UNIVERSITY OF BIRMINGHAM

Hydrogen Carriers Fuel Reforming for On-board Hydrogen Production with Heat Recovery

by

SAK SITTICHOMPOO

A thesis submitted to

The University of Birmingham

for the degree of

DOCTOR OF PHILOSOPHY

School of Engineering

Mechanical Engineering

The University of Birmingham

June 2022

ABSTRACT

The increasing concern of the impact of air pollutants and greenhouse gas emitted by internal combustion engines on global climate change, air quality, and public health have directed the research community to seek various solutions to control and reduce engine-out emissions. Gasoline direct injection (GDI) engines are one of the propulsion systems for road transportation that is heavily regulated by stringent emission legislation bodies. Hydrogen is proposed as an energy vector to help reduce air pollution and decarbonise road transports. However, on-board hydrogen storage is the main obstacle that limits vehicular hydrogen usage. This results in the search for better ways to produce on-board hydrogen for GDI engines to meet both emission legal limits and reduce carbon footprint.

This thesis investigated hydrogen production from ammonia, urea-water solution (AUS32), and AUS32-alcohol fuels (ethanol and methanol) blends through catalytic decomposition. The thesis was carried out using both equilibrium calculations and experiment methods to examine hydrogen yield and product gas compositions from proposed hydrogen carriers. The results indicated that H_2 production could be realised if using waste heat energy from GDI exhaust gas at typical GDI engine conditions. Catalyst inhibition by water combined with limited rate of ammonia decomposition were responsible of unconverted ammonia in the product from hydrogen production process. The presence of gas species in GDI exhaust gas contributed to the formation of by-products (mainly, hydrocarbons) from H_2 production process. The highest hydrogen yield (30.3%-vol) was achieved with AUS32-ethanol blend with significant amount of hydrocarbon by-products. The estimation of tail-pipe CO_2 reduction by using hydrogen produced from ammonia to replace gasoline fuel in GDI engine illustrated the highest impact on tail-pipe CO_2 reduction considering tank-to-wheel scenario. Meanwhile,

using hydrogen produced from AUS32-ethanol blend showed higher estimated CO_2 reduction when analysis performed in well-to-wheel scenario.

The findings in this thesis reveal the feasibility to decarbonise road vehicles equipped with GDI engines. Using proposed carbon neutral hydrogen carriers to improve the air quality to contribute to future zero emission society and address the global climate change.

Dedicated to my dad, my mom, and my wife.

For your endless supports and motivations for me from the start through the end of this journey…

Acknowledgements

Firstly, I would like to thank Prof. Athanasios Tsolakis and Dr. Jose Martin Herreros for their tirelessly great support and their dedicated supervision throughout the research for the past 4 years of my PhD. I am grateful to Dr. Lauren Thomas-Seale for her advice and comments as my independent assessor during my progress reviews.

Many thanks go to Dr. Hadi Nozari and Dr. Julio Augusto Mendes da Silva for their reviews on chemical reactions part in the research – I learned a lot during our academics and non-academics meetings.

I would like to acknowledge the National Science and Technology Development Agency (NSTDA), an agency of the royal Thai government which granted me the full scholarship to pursue my doctoral degree. In addition, I also thank the staff from the Office of the Civil Service Commission (OCSC) and Office of Educational Affairs (OEAUK) for their supervision during my time as a scholarship student. I am very grateful to everyone at King Mongkut's University of Technology North Bangkok (KMUTNB) for their support for me to pursue my PhD. Special Thanks to Assoc.Prof. Kampanart Theinnoi and Asst.Prof. Thawatchai Wongchang for their enormous support from the start.

Thank you to Mr. Jack Garrod, Mr. Kevan Chalesworth, Mr. Lee Gauntlett and Mr. Pete Thornton, the team of technicians who have been of great help to me in the laboratory.

Many thanks must go to my fellow researchers; Dr. Jun Hoe Chan, Mr. Ammar Wahbi, Mr. Jasdeep Singh, Mr. George Blinklow, Dr. Nikolina Kovacev, Ms. Moloud Mardani, Dr. Nahil Serhan and Dr. Kyriakos Xynofon Kallis, for going through the research together, helping each other and uncountable amount of coffee.

Table of contents

ABSTRACT i

Acknowledgements iv

Table of contents v

List of figures x

List of tables xiv

List of abbreviations xv

Nomenclature xviii

Chapter 1 Introduction 1

1.1 Overview 1

1.2 Research focus 4

1.3 Objectives 5

1.4 Thesis outline 5

1.5 Novelty of research 6

Chapter 2 Background and literature reviews 8

2.1 Introduction 8

2.2 Gasoline Direct Injection engine 8

2.2.1 Fundamental and principle of GDI engine 9

2.2.2 Emission regulation 10

2.2.3 Emission controls strategies 11

2.3 Hydrogen addition to improve combustion in SI engine 13

2.4 Hydrogen production 15

2.4.1 Ammonia decomposition 16
2.4.2 Urea decomposition 25
2.4.3 Hydrocarbon fuels reforming 33
2.5 Thermochemical energy recovery 37
2.6 Summary 41
Chapter 3 Experiment facilities and methodologies 43
3.1 Engine test rigs 43
3.1.1 Engines 43
3.1.2 Dynamometer 46
3.1.3 Exhaust gas compositions 47
3.2 Instruments and data acquisitions 48
3.2.1 ATI engine control unit management 49
3.2.2 Fourier Transform Infrared spectroscopy (FTIR) 50
3.2.3 Hydrogen mass spectrometer (HSense) 51
3.2.4 Flue gas analysers 52
3.2.6 Temperature data logging 53
3.2.7 In-cylinder pressure data logging and data post-processing 54
3.2.8 Programmable fuel injection controller unit 55
3.2.9 Fuel reformer gas flow metering 56
3.3 Hydrogen production 57
3.3.1 Hydrogen production setup 57

3.3.2 Methodology of hydrogen production 62

3.4 Thermodynamic analyses 63

3.4.1 Equilibrium calculations 63

3.4.2 Gibbs free energy 64

3.5 Data processing 65

3.5.1 Process efficiency 65

3.5.2 Conversion efficiency 65

3.5.3 Fuel replacement by product gas 66

3.5.4 Heat energy recovery 67

3.5.5 CO_2 reduction by product gas 68

Chapter 4 Energy recovery via catalytic ammonia decomposition for on-board hydrogen production* 73

4.1 Introduction 73

4.2 Experimental conditions 73

4.2.1 Ammonia direct decomposition 73

4.2.2 Ammonia decomposition with GDI exhaust gas 74

4.3 Ammonia direct decomposition 75

4.3.1 Effects of decomposition temperature and ammonia concentration 75

4.3.2 Effects of gas hourly space velocity 77

4.3.3 Energy recovery prediction 78

4.4 Ammonia decomposition with GDI engine exhaust gas 80

4.4.1 Effect of decomposition temperature 80

4.4.2 Effects of O_2/NH_3 ratio 82

4.4.3 Process efficiency and ammonia conversion efficiency 84

4.5 Ammonia and gasoline energy life cycle and carbon footprint 87

4.6 Summary 89

Chapter 5 Aqueous urea decomposition 91

5.1 Introduction 91

5.2 Experiment conditions 92

5.3 AUS32 decomposition in N_2+O_2 93

5.3.1 Effect of AUS32 injection rate and temperature on product gas compositions 93

5.3.2 Process efficiency and urea conversion efficiency 98

5.4 AUS32 decomposition with GDI exhaust gas 99

5.4.1 Effect of AUS32 injection rate and temperature on product gas compositions 99

5.4.2 Process efficiency and urea conversion efficiency 106

5.5 Tailpipe CO_2 emission reduction and waste heat energy recovery 107

5.6 Summary 109

Chapter 6 Hydrogen production from carbon-neutral hydrogen carriers 111

6.1 Introduction 111

6.2 Experimental conditions 112

6.3 Reforming process and fuel conversion efficiencies 112

6.4 Thermodynamics analysis of hydrogen production 114

6.5 Equilibrium prediction of reformate gas compositions 117

6.5.1 Effect of reforming temperature on reformate gas compositions 117

6.5.2 Effect of reactant injection rate on reformate gas compositions 119

6.6 Experimental analysis of reformate gas compositions 120

6.7 Impact on tailpipe CO_2 reduction, energy recovery, and well-to-wheel analysis 123

6.8 Summary 128

Chapter 7 Conclusions and future works 131

7.1 Concluding remarks 131

Energy recovery via catalytic ammonia decomposition for on-board hydrogen production 131

Aqueous urea decomposition 132

Hydrogen production from carbon-neutral hydrogen carriers 132

7.2 General closing remarks 133

7.3 Future works 134

List of references 135

Appendices 158

Appendix A: Arduino coding for the programmable fuel injection controller unit 158

Appendix B: Updated CHEMKIN mechanism 160

Appendix C: Technical specification of the instruments 166

Appendix D: Author Publications 169

List of figures

Figure 2-1: Low pressure loop EGR and high-pressure loop EGR 12

Figure 2-2: Urea solid deposit on the injector nozzle (Left) and on tube wall of laboratory-scale mixing chamber (Right) 32

Figure 2-3: Conceptual diagram of thermochemical energy recovery system 40

Figure 3-1: Engine test rig simplified schematic. 45

Figure 3-2: Engine test rig 47

Figure 3-3: Engine test rig function diagram 49

Figure 3-4: ATI network hub and voltage output modules 50

Figure 3-5: MKS Multigas 2030 FTIR 51

Figure 3-6: Hydrogen mass spectrometer 52

Figure 3-7: Flue gas analyser 52

Figure 3-8: Engine parameter profiles during starting sequences 53

Figure 3-9: Temperature data logger 54

Figure 3-10: Fuel injection controller and its function diagram 55

Figure 3-11: Volumetric fuel injected characteristic of an 8 holes injector with AUS32 56

Figure 3-12: Differential pressure measure-based flow metering apparatus 57

Figure 3-13: Tubular stainless-steel reactor 58

Figure 3-14: Hydrogen production experiment setup 59

Figure 3-15: Hydrogen production from ammonia experiment setup 60

Figure 3-16: Schematic diagram for urea decomposition experiment 61

Figure 3-17: Function diagram of urea supplying system 62

Figure 3-18: Impact of proposed H_2 production system on CO_2 emission 72

Figure 4-1: Process efficiency (A), ammonia conversion (B), change of Gibbs free energy of NH_3 decomposition (C), and hydrogen selectivity (D) 76

Figure 4-2: Estimated energy recovery (A) and gasoline saving and CO_2 reduction (B) via ammonia direct decomposition calculated at GDI engine operation of 148 Nm/2500 rpm. ... 77

Figure 4-3: Effect of GHSV on process efficiency and ammonia decomposition. 78

Figure 4-4: Heat energy requirement for ammonia decomposition (A) and available energy in exhaust heat at various engine conditions (B). 79

Figure 4-5: Predicted CO_2 reduction of passenger vehicle by using hydrogen from ammonia decomposition to replace gasoline fuel 80

Figure 4-6: Equilibrium prediction of product gas compositions from NH_3 decomposition in exhaust gas at $O_2/NH_3 = 0.234$ (A) and change of Gibbs free energy of reactions involved NH_3 decomposition in GDI exhaust gas (B) 81

Figure 4-7: Equilibrium calculations (A) and experimental results (B) of NH_3 decomposition with GDI exhaust gas 83

Figure 4-8: Effect of O_2/NH_3 molar ratio on process efficiency (A) and ammonia conversion efficiency (B) of NH_3 decomposition with GDI exhaust gas 85

Figure 4-9: Estimated energy recovery (A) and gasoline fuel saving and CO_2 reduction (B) by using hydrogen from ammonia decomposition with GDI exhaust gas 86

Figure 4-10: Comparative amounts of CO_2 emissions and energy required for ammonia and gasoline productions. 89

Figure 5-1: Aqueous urea solution decomposition study overview 92

Figure 5-2: Equilibrium calculation of AUS32 decomposition in N_2+O_2 A) effect of temperature, and B) effect of AUS32 injection rate at 650°C 94

Figure 5-3: Change in Gibbs free energy of reactions involved urea decomposition in N_2+O_2 96

Figure 5-4: Product gas compositions from AUS32 decomposition in N_2+O_2 mixture at 550°C (A) and 650°C (B) 97

Figure 5-5: AUS32 decomposition in N_2+O_2 (A) process efficiency and (B) urea conversion efficiency. 99

Figure 5-6: Equilibrium calculation of product gas compositions from AUS32 decomposition in exhaust gas A) effect of decomposition temperature, and B) effect of AUS32 injection rate at 650°C 101

Figure 5-7: Change in Gibbs free energy of reactions involved urea decomposition in GDI exhaust gas 102

Figure 5-8: Product gas compositions from AUS32 decomposition in exhaust gas experiment at 550°C (A) and 650°C (B) 104

Figure 5-9: Process efficiency (A) and urea conversion efficiency (B) of AUS32 decomposition in exhaust gas 107

Figure 5-10: Estimated GDI exhaust gas exergy and % exergy of engine brake output power 108

Figure 5-11: Potential CO_2 reduction and energy recovered if using product gas as REGR 109

Figure 6-1: Reforming process efficiencies of AUS32+EtOH (A) and AUS32+MeOH (B) exhaust gas reforming 113

Figure 6-2: Reactant conversion efficiencies of AUS32+EtOH (A) and AUS32+MeOH (B) exhaust gas reforming 114

Figure 6-3: Change in Gibbs free energy of main reforming reactions as a function of reforming temperature of AUS32+EtOH (A) and AUS32+MeOH (B) exhaust gas reforming 116

Figure 6-4: Reformate gas compositions, equilibrium calculations as a function of reforming temperature for AUS32+EtOH (A) and AUS32+MeOH (B) at a reactant injection rate of 122.5 g/h and 118.5 g/h, respectively. 118

Figure 6-5: Reformate gas compositions, equilibrium calculations as a function of reactant injection rate of AUS32+EtOH and AUS32+MeOH reformings at 550°C and 650°C. 120

Figure 6-6: Experimental results of reformate gas compositions from AUS32+EtOH and AUS32+MeOH exhaust gas reformings as a function of reforming temperature and reactant injection rate 121

Figure 6-7: Hydrocarbon species in the reformate gas of AUS32+EtOH and AUS32+MeOH exhaust gas reforming at a reactant injection rate of 66.6 g/h and 60.8 g/h, respectively..... 123

Figure 6-8: Tail-pipe CO_2 reduction and energy recovery as a function of engine's input energy if e-fuel derived reformate is added via intake manifold to replace gasoline..... 125

Figure 6-9: Impact of hydrogen carrier production routes on CO_2 emissions 126

List of tables

Table 2-1 EURO 6 light-duty vehicle emissions standards on the NEDC 10

Table 2-2 Gas properties comparison between H_2 and NH_3 17

Table 2-3 Summary of Ni-based catalyst characteristics 24

Table 2-4 Summary of Co-based catalyst characteristics 25

Table 2-5 Urea properties 26

Table 2-6 AUS32 properties 26

Table 2-7 Reactions involved hydrocarbon fuels reforming 34

Table 2-8 Carbon neutral hydrogen carrier properties 36

Table 2-9 Category of waste heat recovery technologies for internal combustion engine 39

Table 3-1 The 4 cylinders air-guided GDI engine specifications 44

Table 3-2 The 3 cylinders spray-guided GDI engine specifications 45

Table 3-3 Gasoline fuel properties 46

Table 3-4 Exhaust gas compositions from wall-guided GDI engine 47

Table 3-5 Exhaust gas compositions from spray-guided GDI engine 48

Table 4-1 Experiment conditions for NH_3 direct decomposition experiment 74

Table 4-2 Experiment conditions for ammonia decomposition with GDI exhaust gas 74

Table 4-3 Summary of energy requirement and CO_2 emission of fuel productions. 88

Table 5-1 AUS32 injection rates 92

Table 5-2 Selected engine operating conditions 93

Table 6-1 Reactant injection rates for the H_2 production study 112

Table 6-2 Summary of CO_2 emission of hydrogen carriers from different productions 127

List of abbreviations

AFR	Air fuel ratio
ATR	Autothermal reforming
aTDC	After top dead centre
aTWC	After three-way catalyst
BDC	Bottom dead centre
BMEP	Brake mean effective pressure
BSFC	Brake specific fuel consumption
bTWC	Before three-way catalyst
bTDC	Before bottom dead centre
CA	Crank angle
COV	Coefficient of variation
DEF	Diesel exhaust fluid
DI	Direct injection
DME	Dimethyl ether
DR	Dry reforming
e-fuel	Electrofuel
EGR	Exhaust gas recirculation
EGT	Exhaust gas temperature
FTIR	Fourier-transform infrared spectroscopy
IC	Internal combustion
ICE	Internal combustion engine
IMEP	Indicated mean effective pressure
GDI	Gasoline direct injection

GHG	Greenhouse gas
GHSV	Gas hourly space velocity
HRR	Heat release rate
IMEP	Indicated mean effective pressure
LHV	Low heating value
MBT	Maximum brake torque
NEDC	New European drive cycle
OSR	Oxidative steam reforming
PID	Proportional integral derivative
PM	Particulate matter
POX	Partial Oxidation
ppm	Part per million
REGR	Reformed exhaust gas recirculation
ROHR	Rate of heat release
RWGS	Reverse water gas shift
SCR	Selective Catalytic Reduction
SI	Spark ignition
SMPS	Scanning mobility particle sizer
SMR	Steam methane reforming
SR	Steam reforming
TC	Thermocouple
THCs	Total hydrocarbons
TWC	Three-way catalyst
vol	Volumetric concentration

WGS	Water gas shift
WHR	Waste heat recovery

Nomenclature

AUS32	Aqueous urea solution
CH_4	Methane
C/H	Carbon to hydrogen ratio
CO	Carbon monoxide
CO_2	Carbon dioxide
CO_2/NH_3	Carbon dioxide to ammonia ratio
C_2H_5OH	Ethanol
CH_3OH	Methanol
EtOH	Ethanol
Exp	Experiment
Eqlb	Equilibrium
ΔG	Change in Gibbs free energy
HCs	Hydrocarbons
HNCO	Isocyanic acid
H_2	Hydrogen
H_2O	Water or steam
H_2/CO	Hydrogen to carbon monoxide ratio
H_2O/EtOH	Steam to ethanol ratio
H_2O/fuel	Steam to fuel ratio
H_2O/MeOH	Steam to methanol ratio
H_2O/NH_3	Steam to ammonia ratio
H_2O/urea	Steam to urea ratio
ΔH°_{298K}	Enthalpy of reaction

$\Delta H_{decomposition}$ Enthalpy of decomposition reaction

LHV_{AUS32} Urea solution lower heating value

$LHV_{product}$ Product gas lower heating value

$LHV_{reactant}$ Reactant lower heating value

$LHV_{reformate}$ Reformate gas lower heating value

MeOH Methanol

$\dot{m}_{AUS32}$ Mass flow rate of urea solution

$\dot{m}_{product}$ Mass flow rate of product gas

$\dot{m}_{reactant}$ Mass flow rate of reactant blend

$\dot{m}_{reformate}$ Mass flow rate of reformate

Ni Nickel

N_2 Nitrogen

$(NH_2)_2CO$ Urea

NH_3 Ammonia

NOx Nitrogen oxides or Oxides of nitrogen

NO Nitric oxide

NO_2 Nitrogen dioxide

N_2O Nitrous oxide

O/C Oxygen to carbon ratio

O_2 Oxygen

O_2/fuel Oxygen to fuel ratio

O_2/NH_3 Oxygen to ammonia ratio

Pt Platinum

$\dot{Q}_{recoverable}$ Heat energy recoverable

Rh	Rhodium
Ru	Ruthenium
S/C or SCR	Steam to carbon ratio
SEL	Selectivity
S/F	Steam to fuel ratio
THCs	Total hydrocarbons
Urea/EtOH	Urea to ethanol ratio
ϕ	Equivalence ratio
$\psi_{exhaust}$	Exergy of exhaust gas
η	Decomposition process efficiency
η_{ref}	Reforming process efficiency
γ-Al_2O_3	Gamma-Alumina

Chapter 1 Introduction

1.1 Overview

The effect of climate change as the result of global warming has driven the greenhouse gas (GHG) emission control legislations to become more stringent which affects every aspect of human activities including the transportation sector. The current concentration of ambient carbon dioxide (CO_2) is approximately 400 ppm-vol and with the current rate of CO_2 release, it is expected to raise the global temperature at the rate of 0.07°C per decade [1]. This leads to the pursuit to control CO_2 emission from the transportation sector that includes the phasing out of internal combustion engines (ICE), and the phasing in of electric vehicles (EV).

In the meantime, ICE-powered vehicles, especially gasoline direct injection (GDI) engines, will still play an important role in transportation division for at least another decade during the transition to full electrification [2]–[4]. To achieve a cleaner usage of the GDI engine as a propulsion system, hydrogen (H_2) is nominated as an energy vector to simultaneously reduce regulated emissions and greenhouse gases from the ICEs. Research of H_2 combustion in GDI engines has been carried out and it is proven to be significantly beneficial in terms of improved engine thermal efficiency and reduced regulated emissions through the enhancement of combustion efficiency. However, on-board H_2 storage is the main limitation in terms of feasibility of H_2 usage in transportation. On-board H_2 production from H_2 carriers (hydrogen-containing fuels) using waste heat energy from GDI engine exhaust gas stream demonstrates a potential solution to resolve the hydrogen storage limitation via generating H_2 with accordance to the engine's requirements. This technique is referred to as 'exhaust gas reforming' [5].

Exhaust gas fuel reforming is a thermochemical process that recovers energy from the waste heat of the engine exhaust gas. This is achieved through the promotion of endothermic

chemical reactions (e.g. fuel steam reforming, dry reforming, decomposition of NH_3, etc.) and simultaneously producing H_2. Therefore, reforming process efficiency of higher than 100% is possible because original fuel is converted into product gas containing H_2 which has higher heating value. Relatively high exhaust gas temperature of the GDI engine makes waste heat energy recovery from GDI exhaust more feasible due to higher 'useful' available heat energy [6]. The H_2-containing reformate can be re-introduced into the engine through the intake manifold in a similar method to the exhaust gas recirculation (EGR) system. This technique is also known as reformed exhaust gas recirculation (REGR) which is proven to increase engine intake charge dilution and reduces NO_x while maintaining combustion stability and reduces emissions (e.g. CO, THCs, and CO_2) [6]. The recent research in fuel reforming has been devoted to improve method to predict reformate compositions [7]–[12], develop the fuel reformer [6], [13]–[15], and seeking for new H_2 carriers [16]–[20] for on-board fuel reforming application to enhance engine's thermal efficiency, and reduce engine-out emissions, especially, CO_2.

The selection of H_2 carrier for on-board H_2 production depends on various requirements, for example, available storage, energy density, hydrogen content, enthalpy of reaction when converting into H_2, and GHG emission impacts. Using conventional hydrocarbon fuel for H_2 production can result in considerable carbon footprint as undesired by-product. With the reduction of GHG emission as priority, it is important for H_2 carriers to have low global warming potential (GWP) value [21]. 'Power to X' concept (P2X) (where X can be gas or liquid H_2 carriers or fuel) uses electricity to generate H_2 from electrolysis of H_2O, and react with CO_2 (through hydrogenation reaction) to form energy carrier (e.g. hydrocarbon fuels) and store that energy for later usage [22]–[24]. The technology is based on this concept is also known as 'electrofuel' or 'e-fuel' which mainly uses excess renewable energy (ERE) (e.g. wind, solar, hydro, and nuclear energies) to produce CH_4, ethanol, methanol, DME, gasoline, diesel, and

NH_3 [23]. For the ‘power to chemical’ concept, the same principles as the e-fuel concept are applied but non-fuel chemicals are created as products, for instance; green urea [25]. This concept can be used as a method to reduce atmospheric CO_2 by capturing and using CO_2 as feedstock which makes e-fuel into a ‘carbon neutral fuel’ or ‘non climate-changing fuel’ [24].

Ammonia (NH_3) is one of the most suitable hydrogen carriers that receives attention from both ICEs and fuel cell researchers due mainly to carbon-free properties and advantages over H_2 in various aspects [26]–[28]. For instance, NH_3 has higher hydrogen content than constituent H_2, (both volumetric and gravimetric), higher auto-ignition temperature, lower pressure requirement to store in liquid form, and a distinctive smell that is useful for identifying leakage. H_2 production from NH_3 has been extensively researched mainly on enhancing decomposition catalysts for better low temperature performance [29]–[31].

Urea is the product of synthesis between NH_3 and CO_2 which is colourless, odourless, being non-flammable, non-toxic, and it is miscible in water [32]. Aqueous urea solution (AUS32) or commercially known as ‘AdBlue’ has been used as a reagent for NO_x reduction through SCR (Selective Catalytic Reduction) for commercial vehicles equipped with diesel engines. AUS32 can be used as a hydrogen carrier in the on-board hydrogen production systems [8], [32]–[35]. Additional benefits of using AUS32 include ease of transportation and refilling stations, simplified storage and handling safety [10].

Ethanol and methanol are hydrocarbons electrofuel that have been researched extensively in the context of on-board H_2 production owing to their eligibility as hydrogen carriers [36]–[39]. For instance, there is no sulphur content to damage the reforming catalyst [17] (deactivation via poisoning), low reforming temperature [40], high energy density (both volumetric and gravimetric), high H/C ratio [37] (therefore, high H_2 yield), and ease of storage

and transportation due to their liquid phase [41]. The high miscibility of ethanol and methanol in water enables the blend between AUS32 for steam reforming to enhance the H_2 yield.

The abovementioned H_2 carriers demonstrate their potential as carbon neutral H_2 carriers for on-board H_2 production through exhaust gas reforming while recovering waste heat energy from GDI exhaust gas stream. This thesis presents an efficient method to utilise the proposed H_2 carriers to decarbonise the road transport and decelerate the effect of climate change.

1.2 Research focus

The research's aim is to investigate H_2 production for on-board application through exhaust reforming of various H_2 carriers, for instance, NH_3, AUS32, and the blend of AUS32-ethanol, and AUS32-methanol. Previous works have investigated the performance of H_2 synthesis gas derived from hydrocarbons fuel reforming in an aspect of different reformer scale (laboratory scale [7], [42] and full-scale [6], [13]) and a different of reformate gas compositions [43], [44]. The investigation on hydrogen production from ammonia and urea, was investigated with exhaust from diesel engines [45]. H_2 production from urea has been focused on direct decomposition of urea and autothermal decomposition. The high exhaust gas temperature and low oxygen concentration in the exhaust gas from the GDI engine operated at stoichiometric are the positive prospective for exhaust gas reforming application. The emphasis of this research is mainly on the investigation on the hydrogen production via thermochemical energy recovery through exhaust gas reforming from ammonia, AUS32, AUS32-alcohol fuels blends. The investigation involves using equilibrium calculations to predict the hydrogen yield, product gas compositions, and performing experiments to validate the equilibrium calculations. The impact

of utilising H_2 derived from proposed hydrogen carriers on GDI engine's exhaust waste heat energy recovery and tail-pipe CO_2 reduction are evaluated.

1.3 Objectives

- To investigate the effect of exhaust gas reforming conditions on hydrogen production, reformate gas compositions, reforming process efficiency of the proposed hydrogen carriers (i.e. NH_3, AUS32, AUS32+ethanol, and AUS32+methanol).
- To study the impact of the GDI exhaust gas species on hydrogen production processes.
- To determine the impacts of using H_2 derived from proposed hydrogen carriers on GDI engine's exhaust gas heat energy recovery and tail-pipe CO_2 reduction.

1.4 Thesis outline

Chapter 2 provided some related background of gasoline direct injection engine technology, emissions and current emission controls technology were initially provided. There is a review on hydrogen addition in the engine combustion as a key fuel additive to improve engine performances and emissions. A comprehensive review on hydrogen production through fuel reforming for on-board application was discussed on proposed hydrogen carriers; NH_3, AUS32, ethanol, and methanol, which establishes the research gap in this field. Thermochemical energy recovery technique was examined in this chapter.

Chapter 3 demonstrated details of the experiment apparatus, laboratory facilities, emission analysis instruments, and comprehensive calculations and analyses that were utilised in the research.

In ***chapter 4***, the decomposition of ammonia with or without the presence of exhaust gas from the GDI engine were investigated in presence of rhodium-platinum catalyst at different

O_2/NH_3 ratios and temperatures. Part of this thesis chapter was published in a journal paper "*Exhaust energy recovery via catalytic ammonia decomposition to hydrogen for low carbon clean vehicles*" in "*Fuel*" [46].

In ***chapter 5***, AUS32 was studied as an alternative hydrogen carrier to ammonia for on-board hydrogen production. Equilibrium calculations on AUS32 decomposition are performed to predict the product gas compositions. Experimental study on different AUS32 decomposition conditions was carried out to validate the equilibrium calculations. The effect of H_2 production from AUS32 decomposition on GHG emission and waste heat energy recovery was evaluated.

In ***chapter 6***, AUS32-alcohol blends (ethanol and methanol) exhaust gas reforming were investigated through thermodynamic analyses and experimental study. AUS32 was used as a substitute for water for enhanced H_2 yield of ethanol/methanol steam reforming. The chapter developed an understanding of the effect of various reforming parameters on hydrogen production from the proposed reactant blends for waste heat energy recovery application and the impact on carbon footprint.

Conclusion, and future research works of the thesis were summarised in ***chapter 7***.

1.5 Novelty of research

This thesis has several originalities that contribute to the subject of on-board fuel reforming for the internal combustion engine improvements. The proposed novelties are as follows.

- Study on the on-board H_2 production from non-hydrocarbon hydrogen carriers (NH_3 and AUS32) through the thermochemical energy recovery of GDI engine exhaust gas.
- Presenting synergies between urea solution and e-fuels (ethanol and methanol) reforming with GDI exhaust gas in H_2 production.

- Demonstrated the potential of GDI exhaust waste heat energy recovery and tail-pipe CO_2 reduction using reformate derived from carbon neutral H_2 carriers (NH_3, AUS32, AUS32+ethanol and AUS32+methanol) reforming with GDI exhaust gas.

Chapter 2 Background and literature reviews

2.1 Introduction

This research focused on the production of hydrogen from alternative carbon neutral hydrogen carriers e.g., ammonia, aqueous urea solution, ethanol, and methanol using exhaust gas reforming process. Gasoline engine is considered as a promising candidate for exhaust gas reforming due mainly to its high exhaust gas temperature. Hence, large amounts of waste heat energy can be recovered through the catalytic reforming process. This thermochemical process utilises waste heat and produces hydrogen-rich reformate with H_2 and CO as main gas components. The hydrogen-containing reformate is reintroduced into the intake manifold and expected to improve the overall engine thermal efficiency of gasoline engines utilising energy recovery from waste heat in the exhaust gas. Engine-out emission can improve with the introduction of hydrogen-rich reformate, specifically CO, NO_x, THCs, and CO_2. The detailed review of literature in this chapter will be focused on:

- Fuel reforming with alternative fuels and other hydrogen carriers such as ammonia and Urea.
- The impact of the hydrogen and reformate addition to GDI engine emissions.
- Exhaust gas waste heat energy recovery through H_2 production from thermochemical energy recovery technique.

2.2 Gasoline Direct Injection engine

Gasoline direct injection engine (GDI) is categorised as a spark ignition (SI) engine with direct fuel injection into the combustion chamber which is the current generation of gasoline engine. The new generation of gasoline engine enables better fuel economy and performance

in comparison to the conventional port fuel injection PFI engines. The GDI engine was introduced into mainstream commercial passenger vehicles by Mitsubishi with wall-guided injection configuration [47], which now has become the potential engine option for spark ignition engines to meet CO_2 emissions limits.

2.2.1 Fundamental and principle of GDI engine

The GDI engine has basic engine cycle and hardware structures similar to gasoline engines equipped with PFI and Multi Point Injection (MPI) systems. The distinctive differences are the fuel injector position in the combustion chamber and the higher fuel injection pressure. High fuel injection pressure is needed to overcome the in-cylinder pressure and to ensure sufficient fuel spray formation for good fuel-air mixing.

For a wall-guided GDI engine, the intake charge motion in the cylinder is governed by a piston crown design that creates reverse tumble in comparison to conventional air-fuel charge motion in homogeneous combustion charge engines. In general, wall-guided GDI engines are sensitive to injection timing for operation in stratified charge combustion mode [47].

Meanwhile, for spray-guided GDI engines (SGDI), the intake charge motion plays a less important role in fuel-air mixing in comparison to wall-guided configuration. The fuel spray shape within the cylinder is controlled by the position of injector nozzle holes. Therefore, SGDI engines can be designed without special features on the piston crown to enhance air-fuel mixing as done in wall-guided GDI engines. SGDI utilises higher fuel injection pressure and multi-holes nozzle type fuel injector in comparison to wall-guide systems which can be up to 200 bar to maintain desirable spray penetration in given in-cylinder back-pressure. However, the multi-holes injector is susceptible to solid deposit (e.g. from coking process) from

combustion that causes increased spray penetration length and increased fuel droplet size [48] which can negatively affect unburnt hydrocarbon and particulate matter emissions.

2.2.2 Emission regulation

For ideal stoichiometric combustion ($\lambda = 1$), a conventional gasoline engine emits CO, CO_2, H_2O, NO_x, THCs, and trace amounts of PM as combustion products. The magnitude of emitted CO and THCs have been regulated. Currently, the EURO 6 [49] has limited the amount of CO, THCs, NO_x, and PM emissions as shown in **Table 2-1**.

Table 2-1 EURO 6 light-duty vehicle emissions standards on the NEDC

Pollutant	Emission limits in g/km
	Gasoline
CO	1.000
THCs	0.100
NO_x	0.060
PM	0.005

Although the amount of CO_2 is not regulated by EURO emission standard, the EU set the CO_2 emission target for light-duty vehicles (with average mass of 1390 kg [50]). The CO_2 emission targets with NEDC (New European Driving Cycle) are to achieve 130 gCO_2/km within 2015, 95 gCO_2/km within 2021, 81 gCO_2/km within 2025, and 59 gCO_2/km within 2030. Meanwhile, the CO_2 emission target that is referred to WLTP (Worldwide Harmonised Light Vehicles Test Procedure) set a starting point of 119 gCO_2/km in 2021 and is followed with 15% reduction by 2025, and 37.5% further reduction by 2030 [51].

2.2.3 Emission controls strategies

For conventional port-injected fuel injection gasoline engines operated at stoichiometric mixture, CO, THCs, and NO_x are the main emissions which can be treated using three-way catalyst (TWC) with over 90% conversion efficiency. However, modern turbo-charged GDI engines employ substantial high fuel injection pressure, produce higher output brake power (higher IMEP or BMEP) (e.g. due to down-sizing the engine displacement [52], [53]) and operate in stratified charge combustion. This resulted in considerably higher NO_x and PM emissions. Therefore, such an engine requires similar aftertreatment systems to that of CI engine (e.g., EGR, and particulate matter filter) to suppress engine-out emissions to comply with emission legislations.

EGR is a NO_x emission control technique that involves reintroduction of exhaust gas into the combustion chamber which reduces combustion frame temperature by intentionally causing incomplete combustion. The inert fractions in exhaust gas (e.g. N_2, CO_2 and H_2O) and heat from exhaust gas contribute to the reduction of combustion frame temperature through the simultaneous combination of dilution effect, thermal effect, and chemical effect [54]. The combination of these effects results in deteriorated combustion, therefore thermal NO could be substantially reduced.

EGR structure can be classified into two main types as ‘internal EGR’ and ‘external EGR’ where the former utilises modification of intake and exhaust valves timing to manipulate exhaust reverse flow back into the combustion chamber, and the latter make use of electronically controlled valve to regulate the amount of exhaust gas to be reintroduced through the intake manifold. Another classification of the EGR system in terms of gas flow topology [54] could be classified into two main types based on the location of the EGR loop: low pressure loop (LPL) EGR and high pressure loop (HPL) EGR as illustrated in **Figure 2-1**. LPL EGR has

simple architecture and controls in comparison to HPL EGR due mainly to the pressure difference between exhaust side to intake side is almost always positive which makes LPL operation predictable.

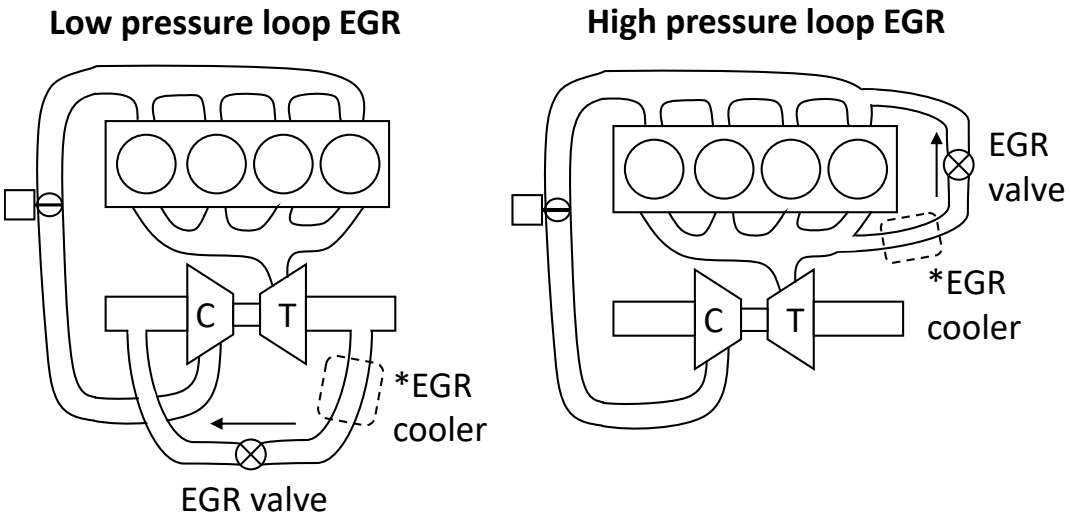

Figure 2-1: Low pressure loop EGR and high-pressure loop EGR

Cooled EGR is the Hot EGR system using a water-cooling heat exchanger positioned upstream the EGR valve which can bring exhaust gas charge temperature down to close to coolant temperature. There are both positive and negative effects on NO_x and THCs emission depending on EGR charge temperature, EGR rate, and engine load (BMEP). The use of hot EGR demonstrated simultaneous improvements in THCs concentration, reduced COV of IMEP, reduced 0-90% mass fraction burned (MFB), improved brake thermal efficiency and CO reduction [54].

In general, utilising EGR in SI engines can reduce throttling loss at part load condition due to the need to open the throttle wider to maintain desired engine torque and speed [6]. The addition of EGR charge into the combustion chamber also reduces heat transfer from burned gas to the cylinder wall. Therefore, brake thermal efficiency (BTE) and fuel economy (BSFC) could be improved [6]. NO_x-PM trade-off is the main consideration of utilising EGR which the

engine designer must compromise between the level of NO_x reduction and the increase in PM concentration. Hergueta et al. [55] reported as high as 5 to 7 times increase of PM (in term of PSD plots) from GDI exhaust gas operated on butanol-gasoline blend at medium load and speed (60 Nm/2100 rpm) when maximum EGR rate (19%) was utilised.

2.3 Hydrogen addition to improve combustion in SI engine

High diffusivity and high flame propagation velocity of hydrogen enhance mixing with air charge which overall results in a fast and stable combustion process. As a fuel for internal combustion engines, hydrogen combustion produces only water due to the absence of carbon atoms. As a result, reduction of CO and CO_2 emissions is proportional to the quantity of H_2 addition in dual-fuel mode. In effect, C/H ratio of air-fuel mixture is decreased with H_2 added in the intake charge [56]. In-cylinder temperature increases as the result of increased pressure by the rapid combustion process of H_2, thus NO_x is increased via thermal NO_x process. In general, THCs concentration will be reduced due to accelerated rate of oxidation by H_2, especially at low engine load due mainly to combined effects of wide flammability limit, significantly shorter flame quenching distance from the cylinder liner [44].

For SI engine, even small amount of H_2 injection in the intake manifold (e.g. 3 to 5% of total fuel input energy [57] or 3 to 9%-vol of intake charge [58]) can reduce noticeable amount of CO and THCs [59] along with improvement in combustion stability and brake thermal efficiency, especially for stratified charge lean operation where misfire occurs at air-fuel lean region [60]. Wide flammability of hydrogen helps to make up with this shortcoming and improves overall combustion quality. As H_2 improves early flame development during CA0-10 [57] (the duration in crank angle from start-of-ignition to 10% of accumulated heat released) which has a high impact on combustion stability [61]. Meanwhile, the main flame propagation

duration, which is defined as CA10-90, indicates a different trend as the result of H_2 addition in comparison to CA0-10. CA10-90 was found to decrease with H_2 presence at low engine load and increase at medium to high engine load which was the result of the effect of H_2 on laminar flame velocity. However, because H_2 addition on CA0-10 was more significant than CA10-90, therefore adding H_2 with intake charge would reduce burn duration in most cases. NO_x emission is reported [59], [62]–[64] to increase with H_2 addition, however; this problem can be mitigated by careful selection of retarded ignition timing within MBT limit while maintaining good engine output performance [60], [65]. Shi, W. et al. [58] demonstrated the benefits gained by retarding the ignition timing of stratified charge operated GDI engine fuelled with hydrogen (up to 10% of intake air volume) and gasoline which proved to enhance overall engine performances in comparison to neat gasoline. CO, THCs, and NO_x emissions were proportional to the degree of ignition retardation, especially NO_x that was significantly affected by this strategy. This was due mainly to reduction of maximum in-cylinder pressure which decreased overall ROHR curve profile, therefore in-cylinder temperature was lowered. A theoretical thermodynamic investigation of on-board H_2 production to reduce fuel consumption and tailpipe GHG emission, was conducted by Zamfirescu and Dincer [35]. Their findings predicted up to 64% GHG emission reduction by using H_2 derived from urea in the internal combustion engine.

Another method to utilise H_2 addition with small NO_x/CO/THCs trade-off is to introduce H_2 along with EGR at high EGR dilution rate to obtain simultaneous reduction of CO, CO_2, THCs and NO_x [57], [64] This approach take advantage of combined effects from hydrogen addition and EGR on the combustion. The method of producing H_2-containing exhaust gas through fuel-exhaust reforming is the foundation of REGR (Reformed Exhaust Gas Recirculation) technique [6], [7], [13]. The reformed exhaust gas is referred to as ‘reformate’

which usually contains H_2, CO, THCs, CO_2, H_2O, and N_2. Initially, the operation limit of utilising EGR in terms of combustion stability based on % of COV of IMEP to not exceed 10% [54] from viewpoint of driveability in real road applications. With H_2 content in the dilution charge, Fennell and his team defined the threshold of deterioration of combustion stability to not exceed 5% of COV of IMEP when using their REGR technique [44]. On the other hand, increasing EGR rate would prolong burn duration and deteriorate the combustion quality which decreased NO_x and increased CO and THCs. The negative effect from EGR could be counter-effect by H_2 addition, especially for low to medium engine loads. H_2 injection allowed the engine to exceed its maximum EGR dilution rate which was governed by flammability limit while maintaining COV of IMEP within practical level [6].

2.4 Hydrogen production

Hydrogen can decarbonise internal combustion engines and can also improve output power, combustion stability and engine-out emissions. However, utilising H_2 as fuel replacement or combustion additive can pose a challenge when it comes to commercial use. Gaseous H_2 has relatively lower volumetric energy density in comparison to other liquid fuels (e.g., gasoline, ethanol, butanol, methanol, etc.) which requires larger volume of storage. Hence, it is sensible to store H_2 in liquid form to achieve comparable volumetric density as conventional liquid hydrocarbon fuels. Although, the requirements to implement H_2 refill infrastructure limits its usage as vehicle fuel on a larger scale. These inherent cost, limitations, and risks of utilising H_2 discourage the feasibility of H_2 as energy for transport vehicles.

Numerous studies had investigated the possibility of producing H_2 on a small scale to supply the internal combustion engine to eliminate the on-board H_2 storage. Several H_2 carriers including hydrocarbon fuels (both liquids [6], [7], [19], [41], [43], [66]–[68] and gaseous fuels

[15], [18], [20]), water, metal-hydroxides, ammonia [28], [29], [45], [69], [70] and urea were studied with various methodologies and processes to generate H_2-containing synthesis gas (or the so-called 'syngas'). Although the on-board H_2 production technology is a mature technology, the amount of the H_2 can be produced on-board is still relatively low. Hence, it is viable to operate an internal combustion engine in dual fuel mode (reformate + conventional fuel) and gain the benefits of improved combustion by H_2.

For industrial scale hydrogen production, steam reforming (SR) and partial oxidation (POX) of natural gas (mainly, methane) is the dominant production method. Coal gasification, biomass gasification and water electrolysis are also used for hydrogen production. However, these methods are out of scope of this thesis and therefore will not be further discussed.

2.4.1 Ammonia decomposition

Ammonia as hydrogen carrier

Ammonia (NH_3) has been considered as one of the best hydrogen carriers for hydrogen production due mainly to its carbon-free (CO_x-free) properties which means there will be no CO_x products from converting NH_3 into H_2 as for hydrocarbon fuels reforming. For onboard hydrogen production application's aspect, NH_3 has several advantages over using storing H_2 onboard in terms of higher energy density per volume, lower weight of container, availability of refill infrastructure [71], and energy cost to produce/transport/store H_2.

Ammonia can be considered a safer alternative to hydrogen for use in combustion owing to higher auto-ignition temperature, higher energy required to ignite, narrow flammability limits, and ammonia's strong smell that can be used to identify leakage in comparison to H_2. **Table 2-2** illustrates gas properties of H_2 and NH_3.

Liquefaction H_2 can be an energy intensive process. Considering H_2 energy volumetric density which is only 1/3 of that of conventional gasoline, it is difficult to justify the use of liquified H_2 in onboard application. For given volume and pressure, NH_3 carries more H_2 atoms than hydrogen in its pure form.

Table 2-2 Gas properties comparison between H_2 and NH_3

Properties	**Hydrogen**	**Ammonia**
Chemical formula	H_2	NH_3
Density at STP (kg/m^3)	0.082*	0.696** (ℓ)
Lower Heating Value (kJ/kg)	120000	18600
Air-fuel ratio (mass basis)	34.4 [72]	6.04 [73]
Laminar flame velocity (m/s)	1.85 [72]-2.9	0.015
Minimum ignition energy (mJ)	0.02	8.0 [74]
Quenching distant (mm)	0.6	
Flammability limit (equivalent ratio)	0.1	
Flammability lower limit (%vol in air)	4 [73]	15.8 [75]
Autoignition temperature (°C)	560*	630**
Flash point (°C)		132**
Molecular weight (kg/kmol)	2.016*	17.031**
Storage pressure (Bar)	10.3 [76]	600
Boiling point (°C)	-253*	-33**
Diffusion coefficient (cm^2/s)	0.61 [77]	

*National Centre for Biotechnology Information. PubChem Database. Hydrogen [78]

**National Centre for Biotechnology Information. PubChem Database. Ammonia [79]

Ammonia decomposition

In theory, ammonia can decompose into hydrogen and nitrogen via thermal decomposition. Direct ammonia decomposition is strongly endothermic, in other word; NH_3 decomposition is thermodynamically limited, and its general reaction as shown in **Equation**

2-1. The decomposition reaction is reversible and is the reverse reaction of the Haber-Bosch reaction that synthesises ammonia.

$$2NH_3 \rightleftarrows 3H_2 + N_2$$
$$\left(\Delta H^{\circ}_{298K} = 46.19 \frac{\text{kJ}}{\text{mol}}, \Delta G = 32.96 \ \frac{kJ}{mol}\right) \qquad \textbf{Equation 2-1}$$

Equilibrium calculation using Chemkin software [80] demonstrates that gas temperature over 400°C is required for complete ammonia dissociation at the pressure of 100 kPa and above. In contrast, Bell and Murciano [81] mentioned that NH_3 decomposition occurs at a temperature range of 520°C to 690°C and the reaction is mainly dependent on NH_3 input concentration. The reason being that the mentioned theoretical temperature by Chemkin is proven under an ideal condition, which means other parameters were not considered such as heat transfer to environment (heat loss), gas hourly space velocity (GHSV), and type of catalyst present.

NH_3 decomposition starts with absorption of NH_3 onto catalyst active sites which have a limited rate. The absorbed NH_3 molecule proceeds through N-H bond cleavage and is followed by a nitrogen atom recombination process [81]–[83]. Recombined nitrogen molecules are desorbed from the catalyst's active site. This step of NH_3 decomposition is considered as a rate-limiting step which determines the overall rate of reaction [84].

In a closed system, a batch reactor which has constant volume, NH_3 dissociation can lead to increased system's pressure as the number of moles of products (mol-H_2 + mol-N_2 = 4 moles) is greater than reactant (2 moles of NH_3) according to **Equation 2-1**. In general, higher NH_3 concentration can generate more H_2 in the end-product, hence; higher partial pressure of H_2. This can cause the reaction to proceed in reverse direction according to Le Chatelier's principle and reduces hydrogen production efficiency (less H_2 yield). Although, in small H_2 generation systems as in this study will emphasise, plug-flow-reactor (PFR) using catalyst in

packed-bed configuration or monolith were the most common type of reactor for NH_3 decomposition. The NH_3 decomposition reactor used in most previous studies [45], [80], [85] employed a continuous flow stream of gas at almost equal or slightly above atmospheric pressure. Therefore, the negative effect from the increased gas partial pressure that reverses $2NH_3 \rightarrow 3H_2 + N_2$ reaction (especially, by H_2 [86]) is negligible, and inlet NH_3 concentration and gas temperature are the dominant parameters that affect hydrogen production efficiency.

Ammonia decomposition in exhaust gas

For onboard application of H_2 production to fuel internal combustion engine, it is sensible to utilise exhaust gas waste heat energy to convert NH_3 into H_2 rather than using other source of heat energy (e.g. primary or secondary fuel, and battery) due mainly to fuel penalty [5], [45]. An approximate 30% of energy from fuel combustion is wasted as heat energy in the exhaust gas which makes heat energy recovery attractive to certain research communities [6], [7]. It is possible to only utilise heat from exhaust gas to decompose NH_3 directly using a combination of catalyst embedded in the heat exchanger, simultaneously has potential to partially recover waste heat energy and produce reformate. However, the concentration of H_2 generated is limited to the available heat in the exhaust gas due to strongly endothermic characteristic of NH_3 dissociation (**Equation 2-1**), which is mainly dependant on the engine IMEP (or BMEP), speed, and AFR (which govern exhaust temperature and mass flow rate). Thus, an exothermic reaction is introduced to generate auxiliary heat to support the decomposition reaction. This can be achieved by introducing a small amount of O_2 to establish oxidation reactions between NH_3 and O_2 as shown in **Equation 2-2**, **Equation 2-3**, and **Equation 2-4** [45], [87].

$$4NH_3 + 3O_2 \rightarrow 6H_2O + 2N_2$$

$$\left(\Delta H^{\circ}_{298K} = -317\frac{\text{kJ}}{\text{mol}}, \Delta G = -1305.4\ \frac{kJ}{mol}\right) \quad \textbf{Equation 2-2}$$

$$2NH_3 + 2O_2 \rightarrow 3H_2O + N_2O$$

$$\left(\Delta H^{\circ}_{298K} = -276\frac{\text{kJ}}{\text{mol}}, \Delta G = -548.6\ \frac{kJ}{mol}\right) \quad \textbf{Equation 2-3}$$

$$4NH_3 + 5O_2 \rightarrow 6H_2O + 4NO$$

$$\left(\Delta H^{\circ}_{298K} = -226\frac{\text{kJ}}{\text{mol}}, \Delta G = -955.1\frac{kJ}{mol}\right) \quad \textbf{Equation 2-4}$$

In an adiabatic system, heat from oxidising 1 mol of NH_3 can decompose 6 mol of NH_3 itself if oxidation reaction occurs (**Equation 2-3**). In this case, O_2 can be derived from the exhaust gas which is in the range between 0.5 to 1.0%-vol (approximately) for typical SI engines operated at stoichiometric [13], [88]. Hence, NH_3 can be reformed with exhaust gas to obtain the merit of additional heat from oxidation reaction. This method of reforming is referred to as ammonia-autothermal reforming (NH_3-ATR) as performed by Wang. et al [45]. and can be written by its overall reaction [45] as shown in **Equation 2-5**.

$$NH_3 + xO_2 \rightarrow (1.5 - 2x)H_2 + 2xH_2O + 0.5N_2 \quad ;\text{for } x < 0.75 \quad \textbf{Equation 2-5}$$

The O_2/NH_3 ratio (by molar basis) (according to **Equation 2-5**, $O_2/NH_3 = x$) is a crucial parameter to control during NH_3-ATR process where partial amount of NH_3 is oxidised which provides additional heat to sustain NH_3 decomposition process. Due to some fuel (NH_3) is consumed by oxidation process, this leads to slight reduction in overall reforming process efficiency (η_{ref}) in exchange of higher H_2 efficiency (η_{H_2}) (increased H_2 yield) at given exhaust gas temperature. According to Wang. et al. [45], H_2 efficiency would increase with O_2/NH_3

ratio up to 0.15 (approx.) and started to decline as O_2/NH_3 ratio increased due to more H_2 fraction being consumed in the exothermic reaction.

Gasoline engine exhaust gas compositions typically contain approximately (by volume) 10-15% of CO_2, 10-14%- of H_2O, 0.5-2.0% of CO, 0.5-1.0% of O_2, 0.01-0.25% of NO_x and up-to 1% THCs (assuming N_2 balanced). Therefore, a competition between reactions occurs, and is subject to selectivity of the catalyst. For instance, Pt has a high tendency to convert NH_3 into N_2O in the presence of O_2, while Ru demonstrates high selectivity toward N_2 formation [89] which is favourable in the presence of NO and O_2.

Using exhaust gas in the reforming process also introduces heat energy with the exhaust stream and this heat can be used to preheat fuel before fuel mixture enters the catalyst. Fennell et al. [13] reported the increased amount of exhaust flow rate in the full-scale fuel reformer could increase fuel-exhaust mixture temperature. The act of preheating fuel can be beneficial to NH_3 decomposition by raising the inlet temperature of NH_3-exhaust gas mixture before entering the catalyst.

Ammonia decomposition catalyst

Ruthenium (Ru) is regarded as the most active catalyst for ammonia decomposition [29], [81] as well as for oxidising NH_3. Ru catalyst is a supported catalyst for ammonia decomposition and can effectively dissociate NH_3 at a relatively low temperature in comparison to other catalysts. Ru catalyst with graphitisation of the carbon nanotube support is reportedly to have onset temperature from 450K and the light-off temperature around 570K for NH_3 decomposition into H_2 [90]. NH_3 decomposition activity depends mainly on catalyst washcoat loading % and type of promoter employed. Carbon nanotubes (CNTs) is a type of promoter currently being researched [91] which could act as good support for Ru nanoparticles by

enhancing dispersion of Ru particles which made Ru more active and stable during NH_3 decomposition process. Ruthenium nanoparticles catalyst with cesium promoter supported on mesoporous crystalline zirconia (Ru-Cs/MPC-ZrO_2) [92] and Ruthenium-ceria supported catalyst (Ru-CeO_2) [93] demonstrated greater turnover frequency (TOF) than Ru-CNTs catalyst which means higher H_2 yield per gram catalyst per minute could be obtained.

Numerous literatures [28], [29], [81], [90], [94] mentioned the scarcity of ruthenium and its high price in comparison to other non-noble metal catalysts. The research for other highly active catalysts for NH_3 decomposition has been studied to develop the alternative to the ruthenium catalyst [27], [28], [95]. However, at this point, the high selectivity of Ru toward N_2 formation is desirable as NH_3 selective oxidation catalyst (NH_3-SCO) [89]. These above-mentioned performance benefits make Ru catalyst the dominant choice for NH_3 decomposition.

For the currently available fuel reforming catalyst, Rh-Pt catalyst with the loading 1.7% and 3.3%, respectively [13], was designed for reforming hydrocarbon fuels. In general, Rh is selective toward NH_3 decomposition into H_2 while Pt and Pd are relatively inactive at NH_3 dissociation and more active toward NH_3 synthesis [96]. For monometallic catalyst system supported on activated alumina, the activeness toward NH_3 decomposition can be rated from high to low, for instance, Ru > Ni > Rh > Co > Ir > Fe >> Pt > Pd > Cu [81] (> means more active, and >> means highly more active). Although, a study [84] reported a different trend (Ru > Ir > Ni) of catalyst activity toward NH_3 dissociation.

Nickel-based catalyst is one of the non-noble precious metal that has been comprehensively studied in the past decades in the attempt to replace the use of Ru-based catalyst for NH_3 decomposition into H_2. [28], [29], [80], [81], [84]–[86], [97], [98] Ni-based catalyst, in general, has lower catalytic activity than that of Ru-based catalyst if the same support/washcoat is used [84]. Combination of Ni/SiO_2-Al_2O_3 catalyst demonstrated higher

TOF and H_2 production rate than Ni-Sepiolite, Ni/Al_2O_3 and Ni/SiO_2 catalysts. **Table 2-3** indicates Ni-based catalysts properties in previous studies.

Table 2-3 Summary of Ni-based catalyst characteristics

Catalyst	Ni %-wt	T (°C)	%NH_3 conversion[%]	T50 (°C)	GHSV	H_2 production rate	Ref.
Ni/Al_2O_3	N/A	800	>99	502-534	600-3000*		[80]
Ni/Al_2O_3	N/A	700	>99	424-576	1160*		[85]
Ni/Al_2O_3-cordierite		614-748	100	545-577	35,000**		[86]
Ni-Pt $/Al_2O_3$	4.7	550-700	>99%	564-600	6520-32600**	480-1910[$]	[98]
Ni/SiO_2-Al_2O_3	0.5g	650	>99	485			[29]

(*unit = h^{-1} , **unit = $cm^3\ g^{-1}_{cat}\ h^{-1}$, [$] mmol g^{-1}cat min^{-1} and [%]using 100%NH_3 input)

Cobalt-base catalyst is comprehensively studied for CO_x-free (carbon-free) hydrogen generation from ammonia as an alternative for precious metal catalyst. In general, it requires substantially higher catalyst loading for cobalt-base ammonia decomposition catalysts than supported catalysts (e.g. Ru, Ni and Rh) to achieve high ammonia conversion [27], [30], [99]. Bimetallic catalyst containing Co and Ni on SiO_2 washcoat exhibited better ammonia decomposition efficiency than monometallic counterpart due to the synergistic effects from both catalysts [30]. Bimetallic catalyst also required lower total catalyst loading in comparison to monometallic catalyst. The catalyst characteristics for example, size of Co nanoparticles, micro porosity, and catalyst nanoparticles dispersion, significantly contributed to M-N bond energy threshold which influenced the rate of hydrogen production [27]. Summary of cobalt-base ammonia decomposition catalyst is illustrated in **Table 2-4**.

Table 2-4 Summary of Co-based catalyst characteristics

Catalyst	%wt Loading	T (°C)	Max% $\%NH_3$ conversion	T50 (°C)	GHSV	Remarks	Ref.
Co_3Mo_3N		600	>99%	481	6000**		[100]
$Cs_{0.018}$ Co_3Mo_3N		550	>99%	451	6000**		[100]
Co+activated carbon or mesoporous carbon support	5-25	400	>99%	Approx. 300	36000**	Microwave heating	[99]
Ni_xCo_y/SiO_2^{Ψ}	10	350-600	76.8-78.1%	Approx. 500-525	6000 to 30000	$^{\Psi}$x:y ratio between 10:0 to 0:10	[30]
Co/Al_2O_3	1.4-7.7	350-580	>99%	Approx. 490-530	6000**	29.41%NH_3 input	[27]

(**unit = $cm^3\ g^{-1}_{cat}\ h^{-1}$)

2.4.2 Urea decomposition

Urea as hydrogen carrier

Urea ($(NH_2)_2CO$) can be considered as a form of NH_3 carrier which is safer than gaseous NH_3 in pure form owing to its non-flammable, non-combustible and non-explosive properties [9]–[11], [34], [35], [101]. Urea is an organic compound also known as carbamide which is formed by combining NH_3 and CO_2. Urea in its solid form is white crystal, odourless, and mildly toxic [102]. Urea is very well soluble in water and stable at room temperature with

$5.45x10^5$ mg/L at 25°C or 54.5%-wt. solubility. Meanwhile, urea is also soluble in ethanol [10] and other higher alcohol or water-soluble fuel [9], [11].

Urea-water solution as ammonia carrier is commercially available to end-users, known as AdBlue or AUS32 (Aqueous Urea Solution) (in Europe) or DEF (Diesel Exhaust Fluid) (in North America). AUS32 has 32.5%-wt. urea and 67.5%-wt. deionised water which has lower hydrogen content than ammonia (in mass basis). High water content in AUS32 significantly reduces fire/explosion safety hazards while still satisfies 6%-wt. hydrogen content 'system-level capacities' hydrogen carrier requirements defined by the US department of energy (DOE) [103]. Physical properties of urea and AUS32 are illustrated in **Table 2-5** and **Table 2-6**

Table 2-5 Urea properties

Properties	**Urea**
Chemical formula	$(NH_2)_2CO$
Density at STP (kg/m^3)	1335
Molecular weight (kg/kmol)	60.056
Melting point (°C)	132-135
Solubility in water (%-wt.)	54.5

Table 2-6 AUS32 properties

Properties	**AUS32**
Chemical formula	**a**$(NH_2)_2CO$ + **b**H_2O
Density at STP (kg/m^3)	1089.5
Molecular weight (kg/kmol)	-
Melting point (°C)	-11
Urea/Water weight ratio	32.5/67.5
Water/Urea molar ratio (**b**/**a** ratio)	6.936

Ease of onboard storage and handling requirement of aqueous urea solution makes its usage appealing to real world application as NH_3 carrier. AUS32 can be stored in a suitable polymer-based container which means less weight penalty and cost for storage. AUS32 has well-established refill infrastructure in countries where the urea-SCR system is compulsory for the De-NO_x system which makes its usage more accessible to end-users.

Water content in AUS32 can be used as reactant for SMR & WGS processes for H_2 production from a mixture of different H_2 carriers [9]–[11]. This benefit from water content in urea solution could potentially reduce the need of additional/separate steam injection system for the reformer setup. However, H_2O/urea ratio of commercial urea solution is constant for given solution and is available in limited range (32.5% to 40.0% by weight for AUS32 and AUS40, respectively) which is the main constraints of using urea solution in on-board H_2 production application.

Urea decomposition

The proposed primary urea decomposition reactions for H_2 production are described in **Equation 2-6**, **Equation 2-7**, and **Equation 2-8**. Urea is injected and evaporates via thermolysis reaction [104]; an endothermic reaction that generates isocyanic acid (HNCO) and ammonia (NH_3) as shown in **Equation 2-6**. The reaction will proceed to hydrolysis of HNCO which is exothermic and produces NH_3 and CO_2 as products as shown in **Equation 2-7** [32]. Ammonia decomposes into hydrogen via an endothermic process as shown in **Equation 2-1**. The global reaction of urea solution decomposition can be expressed as **Equation 2-8** which is overall an endothermic reaction.

$$(NH_2)_2CO\ (g) \rightarrow HNCO + NH_3$$

$$\left(\Delta H^{\circ}_{298K} = 87.66 \frac{\text{kJ}}{\text{mol}}, \Delta G = -125.07 \frac{kJ}{mol}\right) \quad \textbf{Equation 2-6}$$

$$HNCO + H_2O \rightarrow NH_3 + CO_2$$

$$\left(\Delta H^{\circ}_{298K} = -96.19 \frac{\text{kJ}}{\text{mol}}, \Delta G = -89.95 \frac{kJ}{mol}\right) \quad \textbf{Equation 2-7}$$

$$(NH_2)_2CO + H_2O \rightarrow 3H_2 + CO_2 + N_2$$

$$\left(\Delta H^{\circ}_{298K} = 83.85 \frac{\text{kJ}}{\text{mol}}, \Delta G = -13.25 \frac{kJ}{mol}\right) \quad \textbf{Equation 2-8}$$

O/C (oxygen to carbon) and S/C (steam to carbon) ratios are important parameters to control during reforming processes which determine H_2 yield, reforming process efficiency and operating conditions where carbon formation (coke formation) occurs. These ratios are sometimes defined using atomic basis [7] or molar basis [9]–[11]. It is common to refer to O/C and S/C ratio as oxygen to urea ratio (O_2/urea) and steam to urea (H_2O/urea) ratio, respectively. In general, increasing O_2/Fuel ratio would result in lower H_2 yield for the entire range of reforming temperature [9]–[11]. Meanwhile, H_2 yield increases with the H_2O/urea ratio [8]. Increasing H_2O/urea ratio can be beneficial in terms of mitigation from carbon formation which is considered harmful for fuel reforming catalyst [10], [12], [105]. CO from $CO(NH_2)_2 \rightarrow H_2+CO+N_2$ reaction [32] contributes to coke formation through Boudouard reaction [106], [107] at low temperature. Dupont et.al [32] assessed the relationship between the increased S/C ratio and the elevated heat energy requirement for the decomposition process using thermodynamic analysis of urea decomposition in the presence of steam. The effect of urea addition in steam reforming and WGS reactions on carbon formation was examined through a thermodynamic analysis [8], [32]. Carbon contained in urea resulted in increased carbon formation at a low S/C ratio. Introducing ATR technique by including a small amount of O_2 to increase O/C ratio in the reactant mixture could produce a mild oxidation reaction

which effectively inhibited coke formation. Using AUS32 could suppress carbon formation as the result of its high S/C ratio in the urea-water mixture (S/C molar ratio of AUS32 is approximately 6.9 [11], [32]).

Urea decomposition utilises the same decomposition catalyst as NH_3 decomposition. Ruthenium based catalyst has been reported regarding high performance for H_2 production application [10]. Ni/Al_2O_3 was also used for H_2 generation from aqueous urea solution in early work [8] with good resistance to coking formation on catalyst active site.

Challenge of using urea as hydrogen carrier and their solutions

The major consideration of using urea as a hydrogen carrier would be the limited maximum amount of H_2 could be obtained from urea water solution. AUS32 contains H_2 only approximately 2.16% (excluding hydrogen atoms in water) by weight of the solution (or 2.66%-wt. for AUS40). In comparison to alcohol fuel such as ethanol (C_2H_5OH) which has H_2 content approximately 13.04%-wt. or as much as 6 times more than that of AUS32, and AUS40. The low H_2 content problem in AUS32 or AUS40 can be solved by increasing urea in the solution up to 50% by weight which is still within the miscibility limit in water at 25°C [102]. However, this method of enhancing H_2 content will result in higher urea crystalisation temperature (salt-out [108]) which is the main problem of using urea-water solution in cold climate.

Using AUS32 in winter time where ambient temperature is below the AUS32's salt-out temperature (-11°C [108]) which leads to the partially crystallisation within the urea solution and results in tube clogging problems. Another problem with low ambient temperature usage is frozen urea solution. Frozen urea solution can damage the piping line, pump and injector, due mainly to the volumetric expansion of liquid phase solution into solid phase. Frozen urea solution in the reservoir problem can be mitigated by using a heating element with positive

temperature coefficient (PTC) which can self-regulate the heating with minimal control circuit required [109], [110]. To prevent damage from expansion of frozen urea solution, some urea-SCR systems would opt for draining the system before shutting down the engine [111].

High urea conversion efficiency into NH_3 is important which involves several parameters for instance, type of urea solution atomiser, urea solution temperature [112], mixing chamber pressure [113] and temperature, mixing device, mixing chamber geometry, exhaust gas velocity, angle of urea injection into exhaust stream, resident time of urea droplet in the exhaust gas, etc. To achieve high urea conversion efficiency, it is important to minimise urea impingement onto stationary parts along the path. Mainly, the urea spraying process plays an important role in urea decomposition. Finer urea droplets can enhance decomposition by increasing overall surface area, thus heat transfer is improved. This means thermal breakup is enhanced and leads to faster urea solution droplet evaporation [114].

For airless urea injection systems, increasing injection pressure and reducing nozzle diameter can enhance spray atomisation. However, increasing injection pressure can result in greater spray penetration which potentially leads to spray impingement [114]. Impingement causes solid deposit formation that leads to catalyst and gas paths clogged up. However, the possibility of spray impingement to the pipe wall could also be lowered if spray direction was along with the exhaust pipe axial direction [115]. Urea injection pressure of between 4 to 5 bar is used [114], [116] which is within a similar pressure range for the fuel injection system of an PFI system. A higher urea injection pressure up to 8 bar has been experimented which demonstrated enhanced urea solution atomisation [112].

Larsson et al. [112] proposed a novel biomimetic effervescent urea injector which utilised high power heater (200 W per kg/h of AUS32) to heat up urea solution in a fixed-volume chamber and urea solution inlet and outlet were controlled by solenoid valves. The

system was designed to inject the mixture of droplets and hot plume of AUS32 which resulted in better urea to NH_3 conversion, improved NO_x conversion and reduced NH_3 slippage in comparison to conventional urea injector systems. Significant improvement could be observed when the mixing plate was not employed. Similar approach was proposed by Okada et al. [117] utilising glow plugs of 420 W of output power with prototyping urea heating modules which resulted in improved ammonia distribution upstream the SCR catalyst and better NO_x conversion at lower temperature.

Urea solution impingement onto the exhaust tube wall is another problem of utilising liquid phase urea which results in loss fraction of urea solution injected in the form of solid deposit in the SCR system downstream the injector [114] and also found at the injector nozzle and mixing chamber as shown in **Figure 2-2**. Solid deposit negatively affects the system by clogging up the exhaust gas pathway and the SCR catalyst monolith which increases back-pressure in the exhaust manifold. The pump work increases and results in poor engine performances: lower engine output power and higher fuel consumption. The mixing length of the injected urea solution played an important role in reducing wall-wetting [118], [119] as well as the exhaust gas and wall temperatures [118]. Longer mixing length allowed sufficient duration (resident time) for urea solution droplets to absorb heat and complete evaporation, thermolysis and hydrolysis processes. The Decomposition process of urea solution is endothermic intensive [120] and requires a significant amount of heat energy to complete the process hence, high temperature and sufficient exhaust gas flow rate (which defines amount of heat energy available) are crucial parameters for efficient NH_3 formation.

Figure 2-2: Urea solid deposit on the injector nozzle (Left) and on tube wall of laboratory-scale mixing chamber (Right)

By-products of urea decomposition into ammonia such as biuret ($C_2H_5N_3O_2$), triuret ($C_3H_6N_2O_3$), cyanuric acid ($C_3H_3N_3O_3$), isocyanic acid (HNCO), ammelide ($C_3H_4N_4O_2$) and ammeline ($C_3H_5N_5O$) were extensively studied by Tischer et al. [121] on the thermodynamics and reaction mechanisms. Urea decomposition can be categorised into three main steps: urea to biuret mixture, biuret to triuret, and cyanuric acid sublimation where solid deposit is formed by decomposition of triuret into solid phase cyanuric acid and ammelide through separation of ammonia and water, respectively. In urea-SCR systems, it is important to provide sufficiently high exhaust temperature for urea solution to complete evaporation and decompose into NH_3 and H_2O. According to thermogravimetric analysis, complete decomposition temperature of biuret, triuret and cyanuric acid is between 340°C to 400°C [121] which is achievable with gasoline engine exhaust at most operating conditions.

2.4.3 Hydrocarbon fuels reforming

Overview of hydrocarbon fuel reforming

Hydrogen production from hydrocarbon fuels has been broadly studied in the past decades due mainly to the requirement of hydrogen for on-board applications. For instance, electric generation using fuel cells [122]–[125] and as fuel or fuel additive for internal combustion engines [5]–[7], [43], [44], [126] or aftertreatment system [127]–[136] which are the main utilisation of onboard hydrogen. The general reactions involved in hydrogen production from hydrocarbon fuels are summarised in **Table 2-7**. The difference in C/H ratio of each liquid hydrocarbon fuel affects the H_2/CO ratio of the end-product. Additionally, longer chain hydrocarbon fuels will require a higher amount of energy to break the chemical bonds between atoms/molecules. For example, ethanol (ℓ) (C_2H_5OH) has higher enthalpy of formation (Δh_f°) than that of methanol (ℓ) (CH_3OH) (-277.69 kJ/mol vs -238.66 kJ/mol). In addition, more complex chains of hydrocarbons also result in an incomplete conversion, due to the stable form or less reactive hydrocarbons [13].

Steam reforming is the most studied H_2 production to date [38], [41], [66], [67], [137]–[142] due to high H_2 yield and high H_2/CO ratio of reformate. However, it is considered as an energy demanding process and unable to thermodynamically sustain the reaction due to its highly endothermic nature. WGS reaction utilises H_2O to convert CO (which is by-product from SR reaction) into additional H_2 (and CO_2 as by-product). With the requirement of H_2O for SR and WGS reactions, it is preferable to have H_2O/fuel ratio higher than stoichiometry value to ensure complete reforming reaction and to prevent coking formation [9], [10], [19], [142].

Table 2-7 Reactions involved hydrocarbon fuels reforming

Reaction	General chemical formula	Remark
Steam reforming: SR	$C_xH_y + zH_2O \rightarrow (z + \frac{y}{2})\ H_2 + \frac{x}{2}\ CO$	Highest H_2 yield
Dry reforming: DR	$C_xH_y + zCO_2 \rightarrow \frac{y}{2}\ H_2 + (x+z)CO$	
Partial oxidation: POX	$C_xH_y + \frac{x}{2}O_2 \rightarrow \frac{y}{2}\ H_2 + xCO$	
Water gas shift: WGS	$H_2O + CO \leftrightarrow H_2 + CO_2$	
Autothermal reforming 1: ATR 1	$C_xH_y + zH_2O + nO_2 \rightarrow mH_2 + nCO_2$	$m < (z + \frac{y}{2})$, and $n < x$
Autothermal reforming 2: ATR 2	$C_xH_y + zCO_2 + nO_2 \rightarrow mH_2 + nCO_2$	$m < \frac{y}{2}$, and $n < x$
Methanation of CO	$H_2 + CO \rightarrow CH_4 + H_2O$	
Methanation of CO_2	$H_2 + CO_2 \leftrightarrow CH_4 + 2H_2O$	

Dry reforming utilises CO_2 to convert hydrocarbon fuels into H_2 and CO. DR is a strongly endothermic process [143] and has lower H_2 yield than that of SR. DR is a thermodynamically favoured reaction according to Gibbs free energy minimisation analysis [16], [66] and has a natural tendency to proceed than SR at elevated temperature above 700°C.

Autothermal reforming (ATR) is the technique that utilises O_2 [144] and CO_2 or steam to convert methane into H_2-rich syngas [5]. The reformate from ATR reaction using CO_2 and steam have theoretical H_2/CO ratio of 1.0 and 2.5, respectively. For ATR reaction using steam, an author [13] explained the reaction as a combined reaction between SR and POX, which ideally it is desirable that limited or the least possible POX participates in overall reforming process to minimise the fuel penalty (which reduces H_2 yield). The proportion of POX in overall reaction is determined by O_2/C (Oxygen to carbon) ratio (either atomic basis or molar basis) or O_2/Fuel ratio which is usually referred to in molar basis. Meanwhile, ATR reactions using CO_2 are described as the combination of SR and DR reactions.

Methanation is a reaction that produces CH_4 and H_2O through hydrogenation of CO or CO_2. Methanation is a dominating reaction at low reforming temperature [18], [19] that consumes H_2 in the presence of CO or CO_2. Methanation is an undesirable reaction because it reduces H_2 from reformate and can be reversed by increasing reforming temperature. Reversed methanation is also called 'methane steam reforming' (SMR).

As a result of insensitivity and tolerance of internal combustion engine regarding the impurity in the syngas [5] (when compared to fuel cell application), impurity species (CO, THCs, and NH_3) and inert filler (CO_2, H_2O and N_2) in the reformate are acceptable. Due to this research's objective to study the reforming of urea solution and alcohol fuels blends, therefore; ethanol and methanol reforming are examined as H_2 carrier candidates. This is based on high miscibility with water, the absence of sulphur, and carbon-neutrality (no CO_2 contribution to the atmosphere during their life cycles) [40]. Carbon neutral hydrogen carrier properties are as shown in **Table 2-8**. For most hydrocarbon fuels, precious metal-based catalyst (also referred as noble metals) e.g. platinum (Pt), rhodium (Rh), palladium (Pd) and ruthenium (Ru), generally demonstrates good selectivity toward H_2 formation while maintains reasonable low selectivity unwanted by-products. (e.g. NH_3, CO_2, CH_4) Precious metal-based fuel reforming catalyst has been studied extensively in the fuel reforming community [6], [7], [13], [43].

Table 2-8 Carbon neutral hydrogen carrier properties

Properties	Ethanol	Methanol
Chemical formula	C_2H_5OH	CH_3OH
Density at STP (kg/m^3)	789.3	792.0
Molecular weight (kg/kmol)	46.07	32.042
Melting point (°C)	-114.1	-97.6
Solubility in water (mg/mL)	≥100	≥100
Low Heating value (kJ/kg)	26850	20394
Heat of vaporisation (kJ/mol @ 25°C)	42.32	37.34
Source	[145]	[146]

Enhancing hydrogen production through using dual hydrogen carriers

H_2 yield from fuel reforming is limited by various factor e.g. type of reforming fuel (C/H ratio in fuel), S/C ratio, O/C ratio, reforming temperature, heat energy available for the reforming, gas hourly space velocity of the reforming system, reforming reactor design [13], [15], catalyst physical properties, and the selectivity of the catalyst utilised in the reforming process [81]. The stoichiometric reforming reaction defines maximum H_2 yield based on the number of hydrogen atoms in fuel and steam [37], [40]. Hence, fuel with high number of hydrogen atoms in respect to the number of carbon (or having high H/C ratio) can produce high H_2 volumetric concentration. There are works from other authors [9]–[11], [105] involving the thermodynamic analysis of using urea-water solution as steam substitute to enhance H_2 yield of various hydrocarbon fuels. Their results indicated that urea solution could be used in place of steam to achieve higher H_2 yield for either steam reforming and autothermal reforming.

Additional hydrogen atoms from urea contributed to the H_2 in the reformate product. A general chemical reaction of reforming hydrocarbon fuel with urea solution mixture is proposed by [10] shown in **Equation 2-9**.

$$C_xH_yO_z + k(H_2O + m(NH_2)_2CO) + n(O_2 + 3.76N_2) \rightarrow A(aH_2 + bCO + cCO_2 + dCH_4 + fN_2) + gH_2O + hC + jC_xH_yO_z \quad \textbf{Equation 2-9}$$

Where,

k = 0 and n ≠ 0 means the overall reaction is POX.

k ≠ 0, n = 0, and m = 0.315k means the overall reaction is SR.

k ≠ 0 and n ≠ 0 means the overall reaction is ATR.

m = 0 means no urea in the reactant.

m ≠ 0 means there is urea in the reactant.

2.5 Thermochemical energy recovery

Waste heat recovery (WHR) in the internal combustion engine application has been the research topic regarding improving overall thermal efficiency of the engine as a whole system for instance, in a passenger car or transportation vehicle. WHR involves the act of recovering waste heat energy from the engine exhaust gas and using it for useful works. This results in enhancing the engine performances, generating additional mechanical work or electricity or for non-engine purposes (e.g. cabin heating for comfort in winter) [147]. The usefulness of a heat energy source depends on the temperature (high entropy) and amount of heat can be extracted. There are various sources of heat loss from an internal combustion engine. Although, waste heat energy from exhaust gas is the most discussed topic in WHR research due to its high quality and usefulness as a candidate for heat recovery process. Meanwhile, heat loss from coolant is

mainly utilised in low temperature applications such as interior heating and fuel heating where the benefit is less significant in terms of improving the overall system's thermal efficiency. WHR can be categorised as shown in **Table 2-9**.

Thermochemical recuperation (TCP) is the process that utilises heat energy to promote conversion of chemical reactants into different chemical products [148], [149]. Mainly, to convert primary fuel into H_2-rich gas or syngas (synthetic gas) which has higher calorific value. In general, the conversion of biomass (which contains carbon atoms) into fuel (this context will focus on gaseous form of fuel e.g. syngas, town gas/producer gas) through thermal process such as gasification, pyrolysis, water-gas-shift (WGS), and steam reforming are considered as part of thermochemistry [150]. For biomass thermochemistry, the term 'town gas' and 'producer gas' may be used interchangeably which refers to low heating value fuel gas containing mainly H_2, CO, CH_4, CO_2, and traces of other HCs. Heat and electricity productions are the main usage of producer gas as well as the use for synthetic liquid fuel production. Whereas the term synthetic gas or 'syngas' usually refers to gas mixture primarily consisting of H_2 and CO. The remaining CO_2 is removed by means of post-processing.

Table 2-9 Category of waste heat recovery technologies for internal combustion engine

WHR technology	Principle of operation	% Energy recovery efficiency	Reference
Direct heat exchanger	Direct heat transfer between 2 media; using exhaust heating engine & coolant or using coolant heating car interior	N/A	[147]
Turbocharger	Conversion exhaust heat energy into mechanical work using turbine with compressor to increase air density (which decrease pump loss)		[151]
Turbo-compounding	Same as 'turbocharger' but with an additional compounded turbine to further extract useful heat engines downstream (usually used for generating electricity or increasing mechanical output power.		[152]–[155]
Bottoming cycle	Using thermodynamic cycle e.g., Rankine or Brayton cycles which utilise working fluid to drive turbine and generate electrical energy		[156], [157]
Thermoelectric	Utilising solid state device via Seeback effect to convert heat into electrical energy	2.04*	[158]–[163]
Thermochemical	Using heat to convert fuel into reformate with higher enthalpy and use that fuel in the engine in dual-fuel mode	3.4-11.0**	[6], [13], [148], [149]

*Ratio of electrical power to exhaust exergy rate

**in respect to engine output power

In this experimental research, thermochemical energy recovery process involves the use of waste heat energy from engine exhaust gas to convert fuels (which are considered as H_2 carrier) into H_2-containing reformate in the presence of a catalyst that has selectivity toward H_2.

'*Fuel reforming*' is a current research trend of thermochemical energy recovery in the field of fuel cell and internal combustion engines due to the feasibility as an on-board H_2 source. The high calorific value per mass of H_2 results in the increase of heating value of end-product (reformate) [6], [7], [13], [45], [80], [87] after the reforming process. Reforming process efficiency is the ratio between the reformate output energy to the input fuel energy. Reforming process efficiency is used to determine the stage of heat energy recovery (<100% = no heat recovery, and <100% = heat is recovered) [6], [13], [45]. Thermochemical energy recovery technique has been reported to recapture energy up to 18.75% of energy available within the exhaust or approximately up to 11% of engine output power [6]. This technique can be used to further enhance the brake thermal efficiency of the internal combustion engine. The overview of the energy recovery system through thermochemical processes is as shown in **Figure 2-3**.

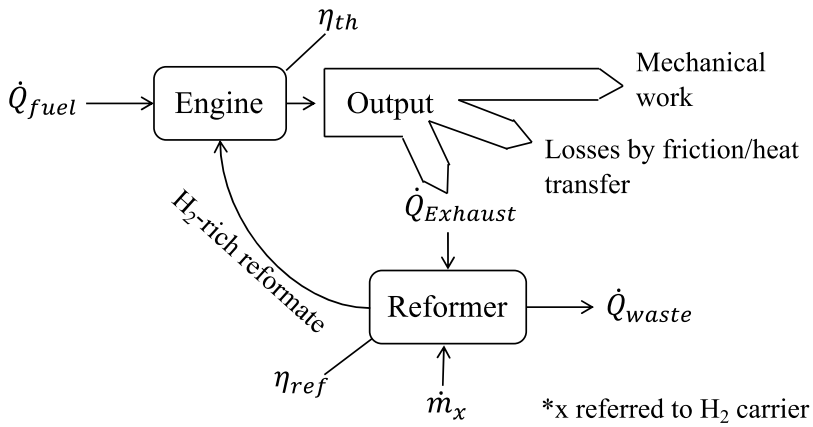

Figure 2-3: Conceptual diagram of thermochemical energy recovery system

Where $\dot{m}_x$ is reforming fuel flow rate, $\dot{Q}_{fuel}$ is engine fuel energy, $\dot{Q}_{Exhaust}$ is exhaust gas energy, $\dot{Q}_{waste}$ is waste heat energy after reformer, η_{th} is brake thermal efficiency (BTE), and η_{ref} is reforming process efficiency.

In a full-scale thermochemical energy recovery system, the heat energy recovery efficiency is determined by the performance of the heat exchanger within the fuel reformer that extracts heat energy from the exhaust gas. Enhancing the endothermic reaction of the reforming

process also plays an important role in the energy extraction process which reflects on reforming process efficiency (>100%). Exhaust gas temperature also dictates TCP's system performance as the result of temperature gradience.

2.6 Summary

This chapter presents an extensive literature review on the thermochemical energy recovery technique to improve the GDI engines combustion and emission characteristics through fuel reforming to produce H_2-containing reformate. Hydrogen combustion as supplementary to other fuels demonstrated benefits in terms of reducing engine-out emissions (CO, THCs, and CO_2) and improving engine's brake thermal efficiency. H_2 improves combustion through the faster flame propagation, better combustion stability, early flame development, increased combustion temperature, and shorter quenching distance from the cylinder's wall. REGR technique showed the combined benefits of H_2 addition and EGR to achieve total emission reduction in GDI engine. This requirement of H_2 usage led to the demand of on-board H_2 production. Hence, H_2 production from various H_2 carriers has been reviewed including NH_3, urea-water solution, and renewable alcohol fuels.

NH_3 is considered as the most attractive H_2 carrier for the on-demand H_2 generation. The higher hydrogen content (volumetric and gravimetric basis), ease of fire safety, and the absence of carbon atoms, make NH_3 a feasible H_2 carrier. The absence of carbon atoms in NH_3 results in further reduction of CO_2 emission when NH_3-derived reformate is utilised in the ICE engine. These promising aspects of NH_3 as H_2 carrier can be reflected in numbers of research on H_2 production from NH_3 decomposition.

Urea is another attractive H_2 carrier candidate for on-board application which has advantages in terms of safety aspect and storage practicality. H_2 production from urea-water

solution has been investigated through both thermodynamic analysis and experimental approaches. However, there are hurdles to overcome with utilising urea solution as hydrogen carrier such as low hydrogen content, crystallisation at low temperature, poor decomposition, solid deposition, and by-products. Solutions to the urea utilisation's problem are comprehensively summarised, for instance; the use of higher urea concentration, employing heating element in urea supplying system, improving urea injector atomisation and positioning, and careful selection of operating temperature to achieve good urea decomposition.

A brief review of hydrocarbon fuel reforming is discussed regarding general reforming reactions involved (steam reforming, partial oxidation, dry reforming, water-gas-shift, autothermal reforming, and methanation reactions). Hydrogen production from exhaust fuel reforming of the proposed electrofuel candidates: ethanol and methanol, is discussed.

Lastly, thermochemical energy recovery technique is reviewed in the aspect of waste heat energy recovery application to enhance the internal combustion engine's thermal efficiency. The high exhaust gas temperature of the GDI engine demonstrated a high degree of usefulness of heat energy source for hydrogen production via fuel-exhaust gas reforming compared to diesel engine exhaust gas.

Chapter 3 Experiment facilities and methodologies

This chapter presents the experiment apparatus and the instruments used in this PhD research. The multiple cylinder GDI engines and the dynamometer setup are briefly discussed. The operational principles, specifications of the instruments, and the laboratory-scale hydrogen production setup utilised in the experiment are reviewed. The detailed data post-processing methodology is presented.

3.1 Engine test rigs

3.1.1 Engines

Two GDI engines were used in this study. The first GDI engine, a wall-guided direct injection system engine, was an inline 4 cylinders with double scroll turbocharger. This engine is used in the experimental study presented in chapter 4. The swept volume was approximately 2 litres. The fuel injectors were located sideways in respect to the cylinder orientation and spark plugs were centrally mounted at the top centre of the cylinder head. It was classified as the first generation of air-guided DI of the GDI category. This engine's detailed specifications are depicted in **Table 3-1**.

The second GDI engine, a spray-guided DI engine, was an inline 3 cylinders with turbocharger and improved cooled exhaust manifold design embedded into the cylinder head. This engine was used in the experimental studies presented in chapter 5 and chapter 6. This engine's suction volume was 1.5 litres, approximately. There were 6 fuel injectors installed, the first injector group was DI injectors configured to form spray-guided fuel within the combustion chamber. Second injector group was port-injected PFI injectors located at the intake manifold

downstream throttle body. The detailed specifications of this engine are shown in **Table 3-2**. The simplified engine test rig is as shown in **Figure 3-1**.

Table 3-1 The 4 cylinders air-guided GDI engine specifications

Detail	Value	Unit
Number of cylinders	4	
Displacement	1999	cm^3
Bore x stroke	87.5 x 83.1	
Compression ratio	10.0:1	
Rated power	149 (@ 6000 rpm)	kW
Rated torque	300 (@ 1750 – 4500 rpm)	Nm
Fuel injection system	Gasoline direct injection	
Maximum injection pressure	200	Bar
Fuel injector	Solenoid actuated, multi-holes	
Fuel	Gasoline E10	
Emissions control	TWC complied to EURO V	
CO_2 emission	169	g/km
Turbocharger	Borg Warner K03	

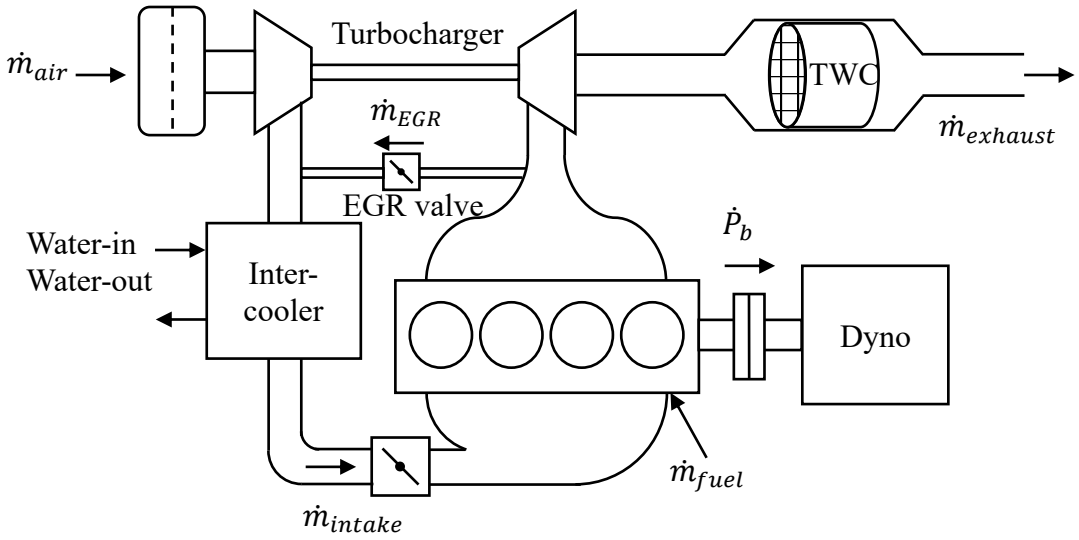

Figure 3-1: Engine test rig simplified schematic.

Table 3-2 The 3 cylinders spray-guided GDI engine specifications

Detail	Value	Unit
Number of cylinders	3	
Displacement	1497	cm^3
Bore x stroke	84.0 x 90.0	
Compression ratio	11.0:1	
Rated power	135.8 (@ 6000 rpm)	kW
Rated torque	270 (@ 1750 – 3500 rpm)	Nm
Fuel injection system	GDI and PFI	
Maximum injection pressure	200	Bar
Fuel injector	Solenoid actuated, multi-holes	
Fuel	Gasoline E0 – E85	
Emissions control	TWC and GPF complied to EURO VI	
CO_2 emission	114	g/km
Turbocharger	Continental radial-axle (RAAX) technology	

The specifications of gasoline fuel used in the GDI engine during the experiment are depicted in **Table 3-3**.

Table 3-3 Gasoline fuel properties

Detail	Gasoline E10
Chemical formula	$C_{6.92}H_{13.40}O_{0.21}$
Research octane number (RON)	95.8
Motor octane number (MON)	85.3
Density at 15°C (kg/m^3)	746.6
Enthalpy of combustion (kJ/kg)	41650
C/H ratio (molar basis)	0.517
Sum oxygen component (%vol)	9.4
C (%-mass)	83.12
H (%-mass)	13.40
O (%-mass)	3.48

3.1.2 Dynamometer

A 75 kW AC dynamometer was mechanically coupled to the engine through the main drive shaft and clutch combination. The dynamometer was controlled by an ABB inverter drive which was capable of both operating in absorption mode (engine drives dynamometer) and regeneration mode (dynamometer motors the engine) through the CADET software supplied by CP Engineering. The dynamometer was able to absorb engine load up to 3500 rpm (equivalent maximum torque of 205 Nm) and was programmed to prevent over-loading failure by means of reducing loading torque, warning alarm and shut-down limits. The engine test rig is as shown in **Figure 3-2**.

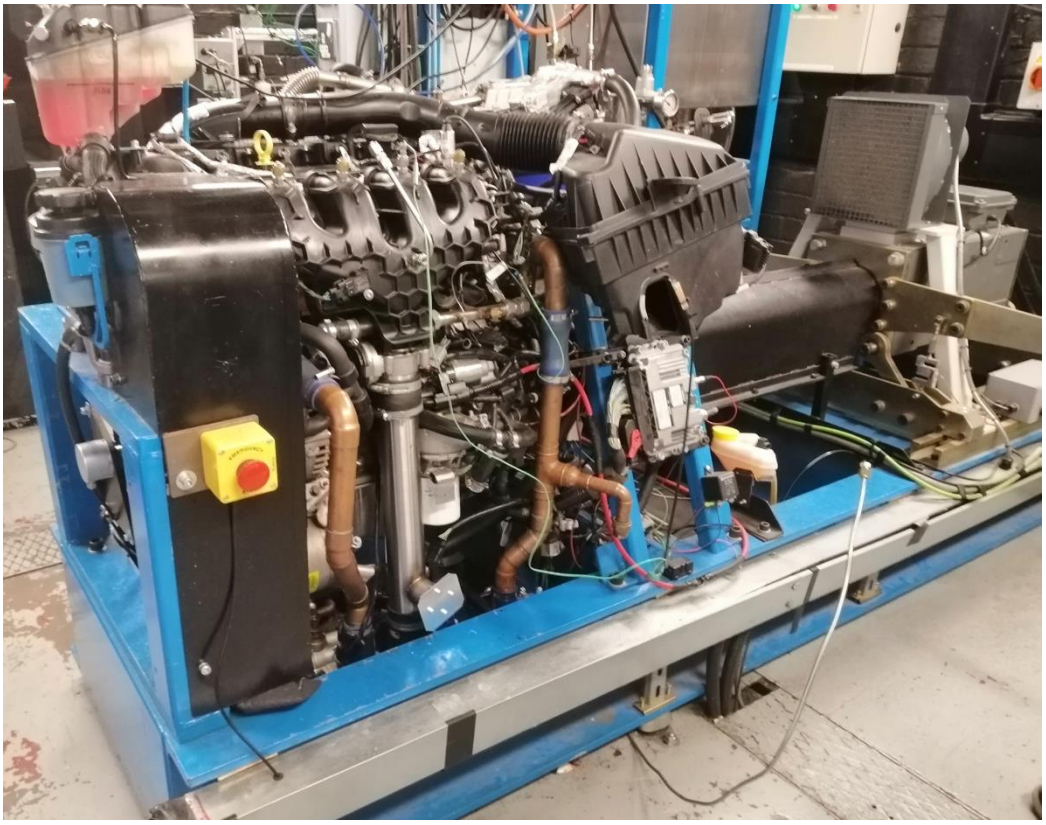

Figure 3-2: Engine test rig

3.1.3 Exhaust gas compositions

The wall-guided GDI engine on an engine dynamometer test rig was employed to supply exhaust gas for NH_3 decomposition in the exhaust gas experiment in chapter 4. The engine condition of 2100 rpm and 35 Nm (IMEP = 3 bar) was chosen based on the New European Drive Cycle (NEDC) for mid-size to large family vehicles with engines of 2-litre displacement. **Table 3-4** tabulates the exhaust gas compositions from the GDI before TWC (bTWC).

Table 3-4 Exhaust gas compositions from wall-guided GDI engine

Exhaust source	CO (ppm)	CO_2 (%)	THC (ppm)	NO (ppm)	NO_2 (ppm)	H_2O (%)	O_2 (%)	H_2 (ppm)
bTWC	6756	11.36	1521	565	1.5	13.15	0.7	2289

The exhaust gas conditions for the thermodynamic analysis and experimental study in chapter 5 and chapter 6 were produced from a turbocharged, 1.5 litre, 3-cylinder, spray-guided GDI engine. The GDI engine was operated at stoichiometric air-fuel ratio (ϕ=1) and steady-state of 2100 rpm and 30 Nm corresponding to an indicated mean effective pressure (IMEP) of 3 bar. The engine-out exhaust gas temperature (EGT) pre-turbocharger was approximately 600°C. GDI engine exhaust gas compositions are as shown in **Table 3-5**.

Table 3-5 Exhaust gas compositions from spray-guided GDI engine

Gas species	**CO (ppm)**	**CO_2 (%)**	**THC (ppm)**	**NO (ppm)**	**NO_2 (ppm)**	**H_2O (%)**	**O_2 (%)**	**H_2 (ppm)**
Volumetric concentration	7044	13.19	1429	1615	2.0	12.61	0.7	2400

3.2 Instruments and data acquisitions

Instruments utilised in this study can be categorised as emission measurements, engine and dynamometer managements, data logging instruments and controllers. Instrument's function diagram is as shown in **Figure 3-3**. Details of instruments will be discussed in the following section.

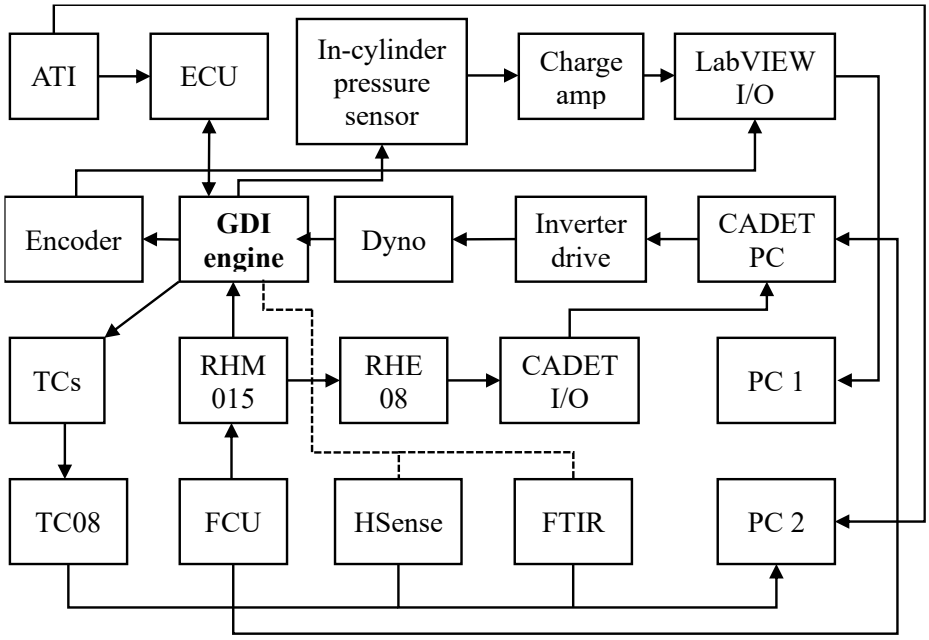

Figure 3-3: Engine test rig function diagram

3.2.1 ATI engine control unit management

VISION software supplied by Accurate Technologies Inc. (ATI) was used for ECU managements in an integrated environment included ECU (Engine control unit) calibration and data acquisition which operated in conjunction with proprietary ATI hardware as shown in **Figure 3-4** (e.g. ECU serial interface, CAN (Control area network) hub, voltage output module) to enable researcher to achieve real-time engine parameter (sensors) monitoring and modifications. The ATI system was used for manually overriding internal EGR (by adjusting intake and exhaust valve timing overlapping), valve timing, lambda value, fuel injection timing, ignition timing, throttle position, boost pressure and fuel pressure.

Figure 3-4: ATI network hub and voltage output modules

3.2.2 Fourier Transform Infrared spectroscopy (FTIR)

MKS Multigas analyser model 2030 FTIR as shown in **Figure 3-5** was employed for measurement of the volumetric concentration of CO, CO_2, NO, NO_2, NH_3, THCs, H_2O and N_2O. Hydrocarbon species can be quantified ranging from C_1 to C_{12}. (Methane to Dodecane). FTIR operates using the concept of the absorption of infrared (IR) spectroscopy. As a gas molecule has its distinctive IR absorption fingerprint, FTIR can determine the type of gas and concentration by comparing the unknown gas spectrum with the known reference gas spectrum. The gas cell with effective path length of 5.11 metre was installed with the spectrometer and was operated at 191°C. Heated line and heated diaphragm pump with temperature controller were used to transport GDI engine exhaust gas and product gas to the FTIR to avoid condensation of gas. The signal to noise ratio (SNR) was maintained approximately 450 during the experiment. An oxygen-free 99.998% nitrogen was employed as purge gas and for flushing the gas cell system for ‘background’ calibration. Further technical information of the MKS 2030 can be found in Appendix C.

Figure 3-5: MKS Multigas 2030 FTIR

3.2.3 Hydrogen mass spectrometer (HSense)

HSense from V&F Analyse- und Messtechnik GmbH, as shown in **Figure 3-6**, was employed to quantify the volumetric concentration of hydrogen based on electron impact ionisation (EIMS) mass spectrometry technique. The HSense sampling rate was 10 S/s (0.1 s sampling interval) with 0.1 ppm display resolution and less than ±2% accuracy. The H_2 detection range was from 0 to 100%-vol. The H_2 mass spectrometer was calibrated using oxygen-free grade N_2 for zero adjustment, and certified 5.04%-vol H_2 for reference concentration. Heated line (same specification as described in '*3.2.2 Fourier Transform Infrared spectroscopy (FTIR)*') temperature was controlled at 191°C by external PID temperature controller.

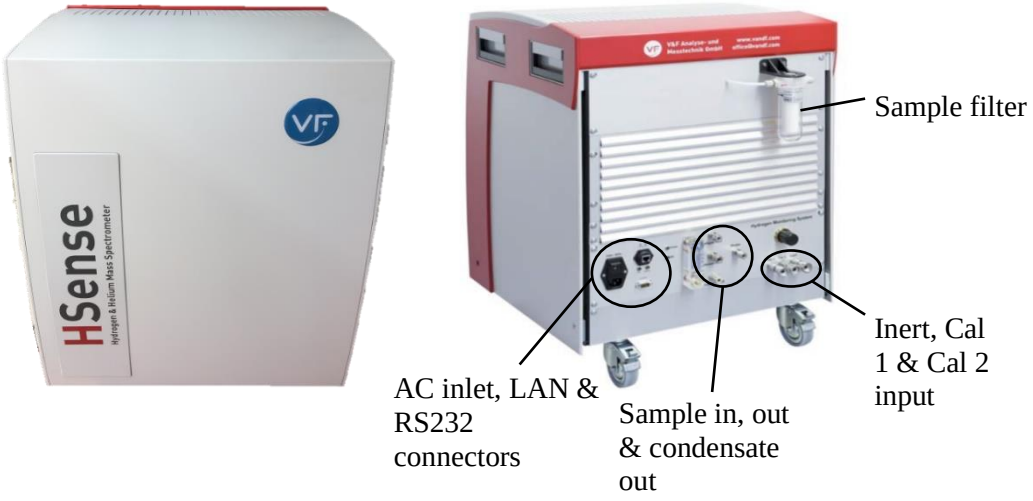

Figure 3-6: Hydrogen mass spectrometer

3.2.4 Flue gas analysers

Testo 340 portable flue gas analyser (as shown in **Figure 3-7**) was used for oxygen volumetric concentration measurement in the range of 0 to 25% with the accuracy of ±0.2% and resolution of 0.01%. The oxygen sensing element reaction time (t_{90}) was less than 20 s. The instrument's internal pump flow rate was 0.6 lpm. To ensure the repeatability of oxygen concentration reading, the reading was taken after a probe connected to the gas source for 2 minutes during the experiment.

Figure 3-7: Flue gas analyser

3.2.5 Engine dynamometer management

CADET software by CP Engineering was mainly responsible for dynamometer management. That included engine load (torque) - rotational speed controls, engine start sequences, coolant temperature control, critical temperature monitoring, auxiliary output controls (e.g., fuel pump, hydrogen solenoid valve, etc.), engine parameters display and data logging. Typical engine parameters (torque, speed and EGT) profiles during engine starting sequences are illustrated in **Figure 3-8**.

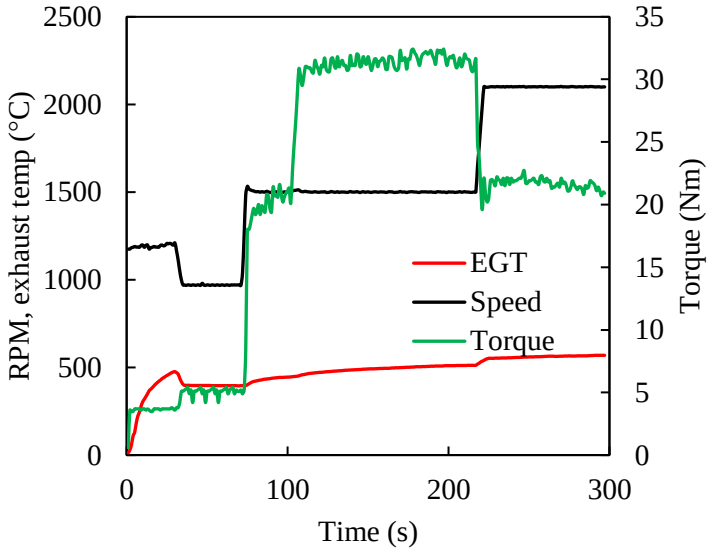

Figure 3-8: Engine parameter profiles during starting sequences

3.2.6 Temperature data logging

A TC08 Pico Technology temperature data logger as shown in **Figure 3-9** and Picolog 6 beta software were used with type-K thermocouples for the temperature recording at various locations e.g., engine-out exhaust before TWC, catalyst inlet, catalyst outlet, reformate output flow sensing element, inlet ammonia mixture and laboratory ambient. Temperature sampling resolution was up to 0.025°C with total temperature reading error of ±0.2% and additional

±0.5°C tolerance. The data logger was factory-calibrated for cold junction compensation. The type-K thermocouples used in this study were supplied by RS components which met IEC60584-1 standard class 1 with tolerance of ±0.5°C and had operating temperature range between -40 to 1100°C. The sampling rate used in this study was 1 Hz.

Figure 3-9: Temperature data logger

3.2.7 In-cylinder pressure data logging and data post-processing

The AVL piezo-electric in-cylinder pressure transducer was installed in the cylinder head at the position of the 4th cylinder combustion chamber. The pressure transducer signal was processed and conditioned by an AVL charge amplifier and data logged by National Instrument (NI) PCI-6251 data logger. The NI card had a maximum sampling rate per channel of 1.25 MS/s (1.25 million samples per second), analogue to digital converter (ADC) resolution of 16 bits, 8 differential or 16 single ended inputs and 4,095 samples of FIFO (First In First Out) memory size. The in-cylinder pressure signal was acquired in synchronisation with crank shaft angular position by a Baumer incremental encoder. The encoder could generate 2 channels of 720 ppr (Pulse per revolution) with 90-degree phasing and 2 channels of complementary 'home' or 'synchronisation' signals. This means the sampling crank shaft angular resolution is 0.5 CA (Crank Angle).

An in-house developed Labview software was used for data acquisition from NI card and displayed online calculations of IMEP, COV of IMEP, and peak in-cylinder pressure.

However, the rate of heat release (ROHR or HRR), and MFB were post-processed off-line using a custom MATLAB script. A consecutive 200 cycles of in-cylinder pressure profiles were acquired for each post-processing into ROHR.

3.2.8 Programmable fuel injection controller unit

The programmable fuel injection controller was used for urea injection together with urea feeding system (in section '*Urea* ') for study in chapter 5 and chapter 6. The controller was a combination of microcontroller-based module and N-channel MOSFET driver module that controlled fuel injector in time resolution down to 10 µs. Arduino Uno was the microcontroller platform chosen in this study. Injector control signal from the controller was fused to comply with the safety requirements and could be manually hardware overridden by a physical external switch. The schematic diagram of the controller is as shown in **Figure 3-10**.

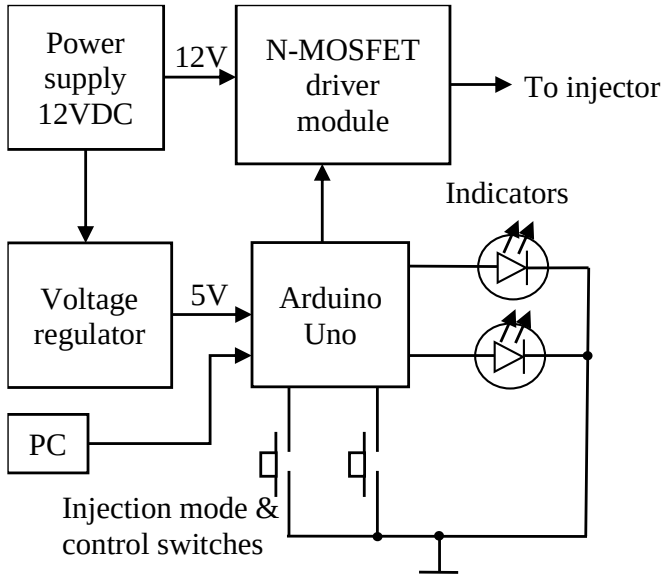

Figure 3-10: Fuel injection controller and its function diagram

The coding for the controller is illustrated in Appendix A. The injection turn-on duration was constant at 2.0 ms and injection turn-off duration was adjusted to obtain designated

frequency. Hence, AUS32 flow rate could be controlled by changing injection frequency. The injection flow rate characteristic curve of AUS32 at 3 bars is as shown in **Figure 3-11**.

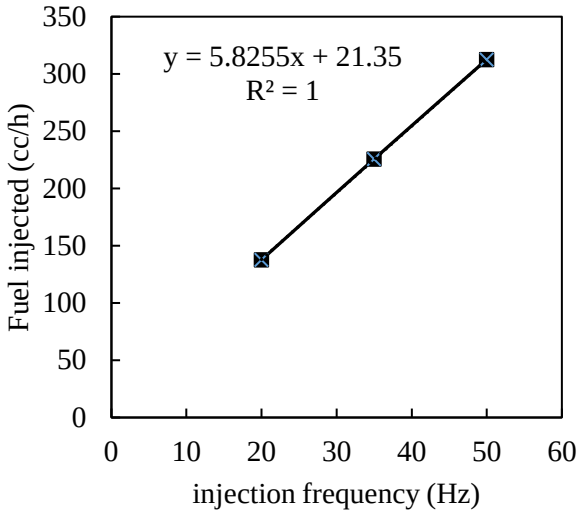

Figure 3-11: Volumetric fuel injected characteristic of an 8 holes injector with AUS32

3.2.9 Fuel reformer gas flow metering

For laboratory scale fuel reformer, volumetric gas flow rate was monitored by an in-house built system as shown in **Figure 3-12**. The device was based on the same principle as gas flow measurement using a restrictor device such as venturi tube or orifice plate, by measuring the pressure drop across the restrictor device. In this case, a ¾" three-way Swagelok fitting and ¾" to ¼" reducing union were modified to create a restrictor and installed downstream the fuel reformer before the suction pump. The pressure drop across the restrictor was measured by Testo 510.

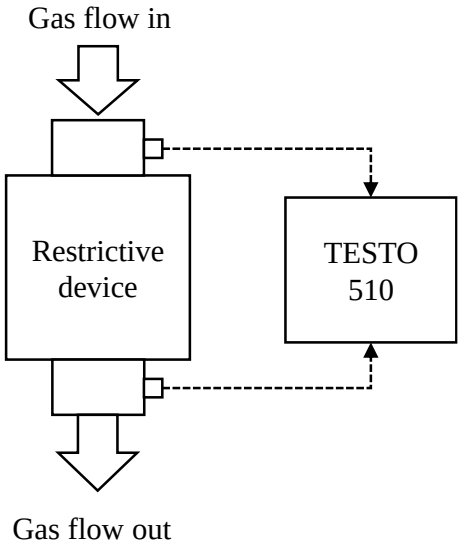

Figure 3-12: Differential pressure measure-based flow metering apparatus

3.3 Hydrogen production

3.3.1 Hydrogen production setup

In chapter 4, a rhodium-platinum (Rh-Pt) fuel reforming catalyst coated on a ceramic monolith with ceria-zirconia-alumina (CZA) support with dimension of 22 mm (diameter) x 77 mm (length), has Rh/Pt ratio of 1.7/3.3 (by weight) and monolith cell density of 400 cell per square inch (cpi) was used in the study. In chapter 5 and chapter 6, a ruthenium catalyst coated on a ceramic monolith (Ru 2%-wt. loading, γ-Al_2O_3, 600 cells per square inch) with dimension of 25 mm (diameter) x 75 mm (length) was employed for the experiment. The catalyst monolith was located inside a stainless-steel tubular reactor as shown in **Figure 3-13**. The reactor was mounted in a Carbolite GVA 12/600 3.9 kW electric furnace, and the reactor was insulated by Superwool 607 as illustrated in **Figure 3-14**. The furnace PID temperature controller was tuned with the reformer setup to attain stable temperature. Volumetric-based gas hourly space velocity (GHSV) was calculated using **Equation 3-1** which could be altered by adjusting total gas flow rate through the catalyst. Due to the low mass flow rate of reformate could be produced from

the laboratory scale reforming setup, therefore; this study did not feed hydrogen-containing product gas back into the GDI engine's intake manifold.

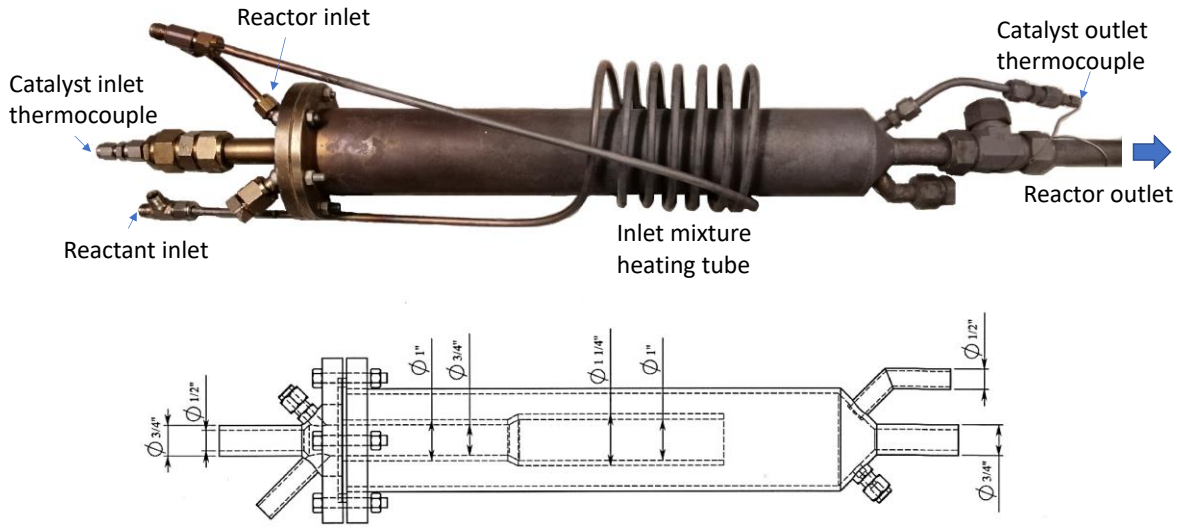

Figure 3-13: Tubular stainless-steel reactor

$$GHSV\ (h^{-1}) = \frac{gas\ flow\ rate\ (lpm) \times 60}{catalyst\ projected\ volume\ (l)} \qquad \textbf{Equation 3-1}$$

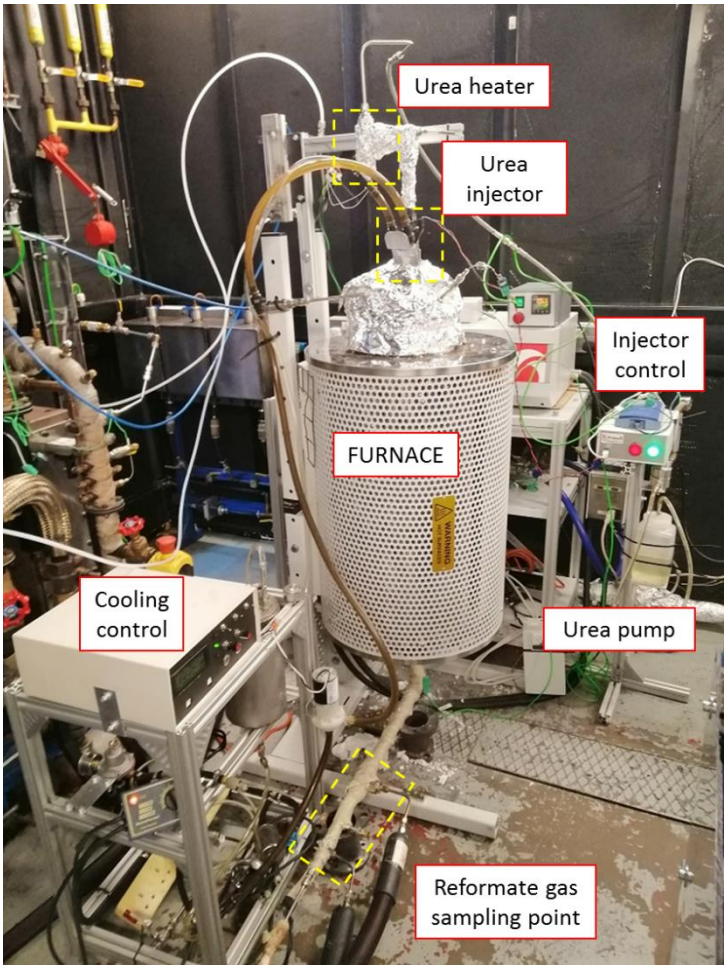

Figure 3-14: Hydrogen production experiment setup

Ammonia decomposition

Ammonia decomposition study utilised diluted ammonia in nitrogen balance (5% NH_3 by volume) provided by BOC UK. Low NH_3 concentration was used to comply with the health and safety regulations. The supply pressure was regulated to 2 bar and volumetrically controlled by CT Platon rotameters (Maximum flow rate: 10 lpm). Bottled nitrogen (99.99% N_2 by volume) (provided by BOC UK) was pressure-regulated to 2 bar and controlled by another CT Platon rotameter (Maximum flow rate: 10 lpm). Check valves were installed downstream the rotameters before mixing both gases and delivering the mixture to the ammonia reforming

reactor. Schematic diagram of H_2 production from NH_3 experiment setup for chapter 4 is as shown in **Figure 3-15**.

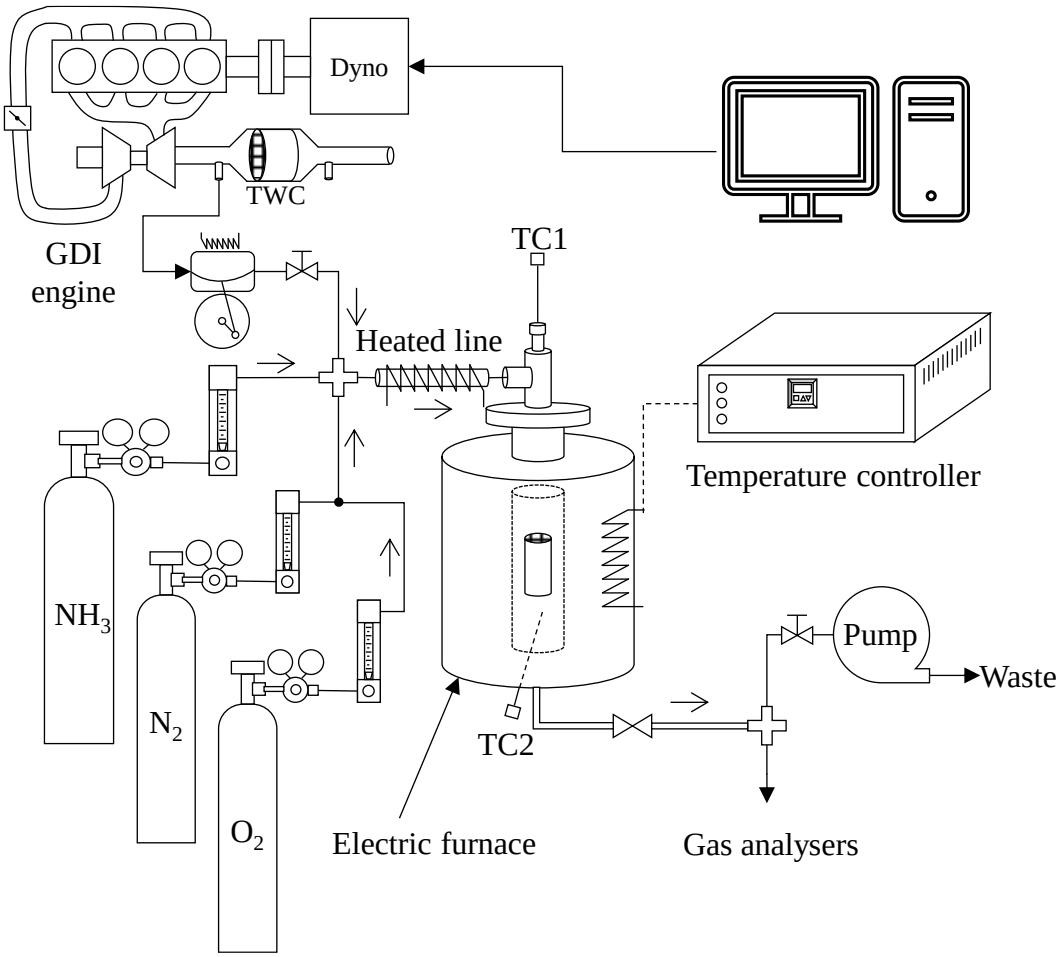

Figure 3-15: Hydrogen production from ammonia experiment setup

Urea and urea-alcohol decomposition

The laboratory experimental setup and the schematic diagram are demonstrated in **Figure 3-16**. The urea-blended fuel supplying system is as illustrated in **Figure 3-17** which is a similar system configuration to the conventional gasoline fuel system. The urea solution feeding system was utilised for injecting urea solution for urea exhaust reforming in the study in chapter 5 and chapter 6. The pump utilised with urea solution was an Ismatec Micro Pump model GA-X21 CFSB magnetic-driven gear-pump in a sealed configuration. The sealed pump

has the separation between electric motor internal components and the wet part of the pump. A temperature-controlled heating system is employed to provide a heated urea solution to the urea injector. This is done to enhance urea decomposition efficiency in the similar method performed by Larsson et.al [112]. In this study, the pressure and temperature of urea solution were at 3 bar and 100°C to avoid urea solution boiling and damage to the urea injector. The fuel injector was a urea-SCR system injector with a water-cooled jacket and installed perpendicular to the exhaust inlet flow direction.

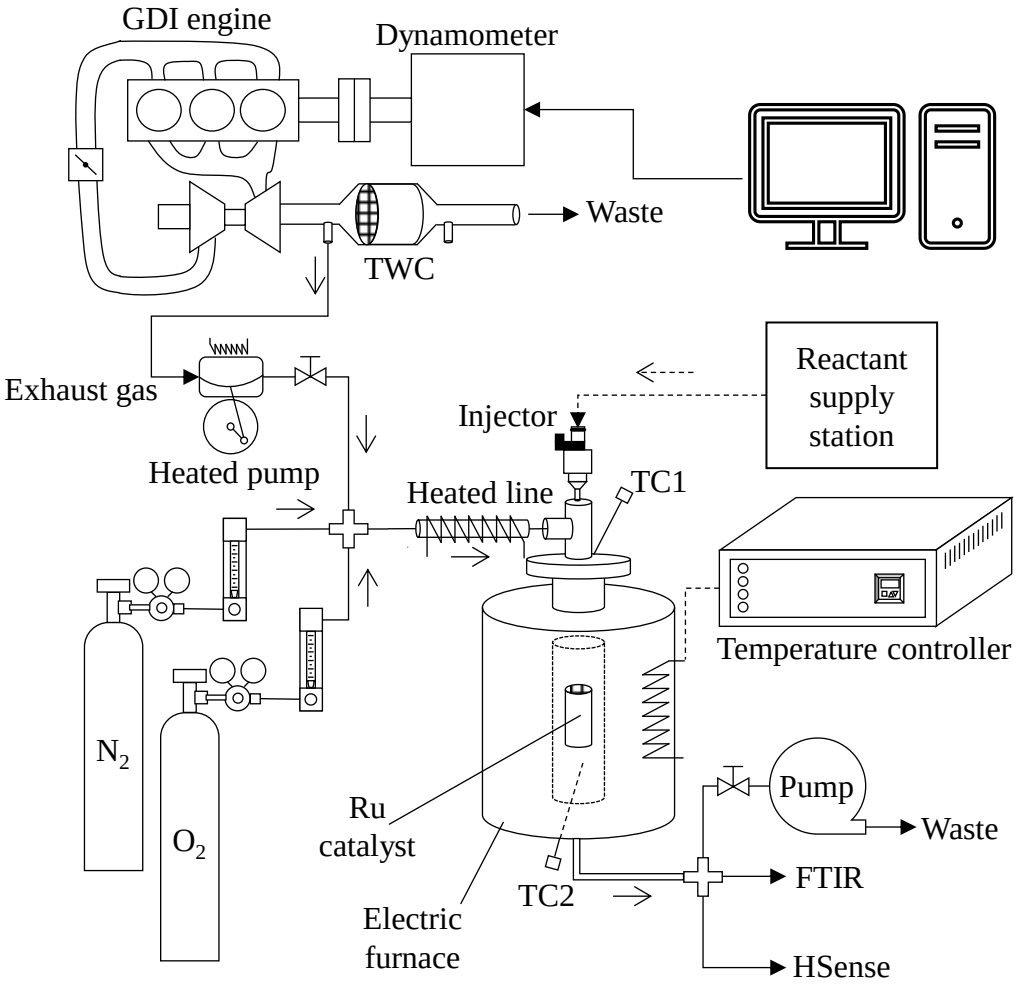

Figure 3-16: Schematic diagram for urea decomposition experiment

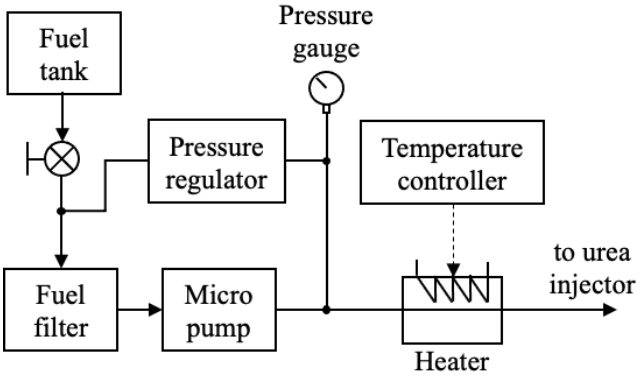

Figure 3-17: Function diagram of urea supplying system

3.3.2 Methodology of hydrogen production

Methodology for Chapter 4

To obtain similarity to real engine exhaust condition, the electric furnace was controlled and monitored to achieve catalyst inlet gas temperature between 450 to 650°C. This resembled an actual GDI engine exhaust gas temperature in medium to high engine loads. For direct NH_3 decomposition experiment, NH_3+N_2 mixture was fed into the reactor to obtain designated GHSV. For NH_3 decomposition in GDI exhaust gas experiments, NH_3, N_2 and GDI exhaust gas were supplied at defined flow rates and O_2 concentration was measured to validate the O_2/NH_3 ratio. The reactor was allowed to reach steady state conditions before gas compositions readings and temperature data were recorded. For reproducibility of the experiment, the reactor was flushed with N_2 until NH_3 reading returned to the background level before conducting the next experiment condition.

Methodology for Chapter 5 and Chapter 6

Bottled gas N_2 and O_2 were utilised in the AUS32 decomposition experiment to investigate the baseline H_2 production of urea decomposition via ATR (Oxidative decomposition) in chapter 5. The N_2+O_2 mixture was formulated to achieve designated O_2

concentration of 0.7%. On the other hand, in the experiment of AUS32 decomposition in GDI exhaust gas, exhaust gas was brought from a GDI engine using the temperature-controlled heated pump and heated line which delivered exhaust gas to the fuel reformer setup. N_2+O_2 gas mixture and GDI exhaust gas volumetric flow rates were established on GHSV of 12000 h^{-1}. Both experiments were carried out with the catalyst inlet temperature of 550°C and 650°C (±5%). For experiment in chapter 6, the same experimental setup was used for exhaust gas reforming experiment and H_2 carrier was changed from AUS32 to AUS32+EtOH or AUS32+MeOH blends.

The experiment is carried out when exhaust gas flow rate is adjusted to reach the designated volumetric flow rate and the temperature at the catalyst inlet attains steady state. Reactants (AUS32, AUS32+EtOH, and AUS32+MeOH) were then injected starting from minimum reactant flow rate (at equivalence O_2/NH_3 of 0.15). The system is flushed with GDI exhaust gas in between each reforming condition to remove remaining reactant on the catalyst surface for reproducibility of the experiment. The system is allowed to reach a steady state of reforming before gas composition readings are taken.

3.4 Thermodynamic analyses

3.4.1 Equilibrium calculations

The equilibrium calculations of ammonia decomposition (Chapter 4), AUS32 decomposition (Chapter 5), and AUS32-alcohol blends reforming (Chapter 6) were performed using Chemkin v.18.2 with reduced mechanism by H. Nozari [164], [165]. The mechanism was developed based on Konnov's mechanisms [166]. Updated hydrogen oxidation mechanisms by Konnov's (2019) [167] were merged with existing mechanisms to enhance accuracy of the calculation. The equilibrium calculation was computed using Gibbs free energy minimisation

method to predict product gas compositions at constant pressure and enthalpy conditions. The GDI engine exhaust gas compositions from engine condition at 2100 rpm and 3 bar IMEP was applied in the equilibrium calculation. Reactant species molar concentrations were applied in %-volume basis which was normalised into total molar of 1 by the software. The equilibrium calculations are computed at constant pressure of 1 bar and at temperature ranges from 400°C to 800°C. Mechanism and thermodynamic file are depicted in Appendix B.

In chapter 5 and chapter 6, the mixture of NH_3(g), HNCO(g) and H_2O(g) is applied as a surrogate for AUS32 assuming the stoichiometry condition that 1 mole of urea converts into 1 mole of HNCO and 1 mole of NH_3 as shown in **Equation 2-6**.

3.4.2 Gibbs free energy

To understand the thermodynamic spontaneity and feasibility of a reaction, the change of Gibbs free energy of reactions involved in H_2 production was calculated using Microsoft Excel spreadsheet over the range of temperature based on **Equation 3-2**. Where ΔG is the change of Gibbs free energy in kJ/mol, ΔH is the change of standard enthalpy in kJ/mol, T is the temperature in K, and ΔS is the change of standard entropy in kJ/mol.K.

$$\Delta G = \Delta H - T\Delta S \qquad \textbf{Equation 3-2}$$

The analysis of ΔG in chapter 5 is carried out with core reactions involved the H_2 production, for instance; NH_3 cracking, Urea+H_2O→H_2+CO_2+N_2, urea thermolysis, hydrolysis of HNCO, WGS, methanation of CO and CO_2. In chapter 6, additional reactions involving ethanol and methanol reforming are included in the analysis, for instance, SR of ethanol, SR of methanol, and DR of ethanol.

3.5 Data processing

3.5.1 Process efficiency

The process efficiency of the decomposition process (η) or reforming process (η_{ref}) can be calculated by **Equation 3-3** which is the ratio between output energy of the output product gas and the input energy of input reactant. Where, $LHV_{product}$ is the product gas lower heating value in kJ/kg, $LHV_{reactant}$ is the reactant lower heating value in kJ/kg, $\dot{m}_{product}$ is the product gas mass flow rate in kg/s, $\dot{m}_{reactant}$ is the reactant mass flow rate in kg/s. The efficiency higher than 100% indicates enthalpy increased by reforming process and reforming efficiency less than 100% indicates fuel lost during reforming process.

$$\eta_{ref} \; or \; \eta = \left(\frac{LHV_{product} \times \dot{m}_{product}}{LHV_{reactant} \times \dot{m}_{reactant}}\right) \times 100\%$$

Equation 3-3

For a full-scale fuel reforming system coupled to the engine exhaust system that exceeds 100% reforming process efficiency, this means energy in engine exhaust gas is recovered and contributes to the overall engine thermal efficiency enhancement. In this context, input heat energy is assumed that it can be harvested from the GDI exhaust gas and therefore input heat energy is considered as 'free energy'

3.5.2 Conversion efficiency

Ammonia conversion efficiency can be analysed by **Equation 3-4** using volumetric concentration of ammonia at catalyst inlet and outlet. This equation calculates the overall conversion efficiency based on the amount of ammonia consumed by the reaction.

$$NH_3\ conversion\ efficiency = \left(\frac{input\ molar_{NH_3} - output\ molar_{NH_3}}{input\ molar_{NH_3}}\right) \times 100\%$$

Equation 3-4

Urea conversion efficiency is the ratio between urea consumed by the decomposition process to the input urea as shown in **Equation 3-5** which assumes the ideal condition that 1 mole urea converts into 2 moles NH_3. Then NH_3 derived from urea is decomposed or reformed in the process.

$$Urea\ conversion\ efficiency = \left(\frac{(input\ molar_{urea} \times 2) - (output\ molar_{NH_3})}{input\ molar_{urea} \times 2}\right) \times 100\%$$

$$Urea\ conversion\ efficiency = \left(1 - \frac{output\ molar_{NH_3}}{input\ molar_{urea} \times 2}\right) \times 100\% \quad \textbf{Equation 3-5}$$

Fuel conversion efficiency for ethanol and methanol is the ratio between fuel consumed by the reforming process to the input fuel as shown in **Equation 3-6**.

$$Fuel\ conversion\ efficiency = \left(\frac{input\ molar_{fuel} - output\ molar_{fuel}}{input\ molar_{fuel}}\right) \times 100\%$$

Equation 3-6

3.5.3 Fuel replacement by product gas

Prediction of gasoline fuel replacement by product gas is based on the assumption that adding H_2-containing product gas from the decomposition/reforming process can partially replace gasoline fuel. It is assumed that engine thermal efficiency remains the same to simplify

the analysis. Fuel replacement by product gas is calculated by assuming the energy from the product gas is equal to energy of gasoline can be replaced. Then mass flow rate of gasoline replaced by adding H_2-containing product gas from the decomposition/reforming process can be obtained as shown in **Equation 3-7**.

$$\dot{Q}_{product} = \dot{Q}_{gasoline,replaced}$$

$$\dot{Q}_{product} = LHV_{gasoline} \times \dot{m}_{gasoline,replaced}$$

$$\dot{m}_{gasoline,replaced} = \frac{\dot{Q}_{product}}{LHV_{gasoline}} \qquad \textbf{Equation 3-7}$$

3.5.4 Heat energy recovery

Producing H_2 on-board through an overall endothermic reaction using waste heat energy from exhaust gas is deemed as a heat energy recovery. This study estimates heat energy recovery from GDI exhaust gas stream calculated based on the maximum amount of H_2-containing product gas that can be produced which is limited by the available heat energy recoverable ($\dot{Q}_{recoverable}$) from GDI exhaust gas as shown in **Equation 3-8**.

$$\dot{Q}_{recoverable} = \eta_{recovery} \times \psi_{exhaust} \qquad \textbf{Equation 3-8}$$

Where $\eta_{recovery}$ is waste heat energy recovery coefficient obtained from previous works [13] and [46], and $\psi_{exhaust}$ is exhaust gas exergy of exhaust gas that contains multiple gas species) which is calculated using **Equation 3-9**.

$$\psi_{exhaust} = \sum \dot{N}_{exhaust} \cdot n_i \left(\left(h_i - h_{i,0} \right) - T_0 \left(s_i - s_{i,0} \right) \right) \qquad \textbf{Equation 3-9}$$

Where $\dot{N}_{exhaust}$ is molar flow rate of the exhaust gas (kmol/s), n_i is molar fraction of gas specie i, h_i and $h_{i,0}$ are enthalpy of gas specie i at temperature 'T' and 298 K, s_i and $s_{i,0}$ are entropy of gas specie i at temperature 'T' and 298 K, and T_0 is ambient temperature (298 K).

Once $\dot{Q}_{recoverable}$ is determined, then the maximum possible reactant mass flow rate can be calculated using **Equation 3-10**. Where $\Delta H_{reforming}$ is enthalpy of reforming reaction of specific reactant.

$$\dot{m}_{reactant} = \frac{\dot{Q}_{recoverable}}{\Delta H_{reforming}} \qquad \textbf{Equation 3-10}$$

3.5.5 CO_2 reduction by product gas

CO_2 reduction can be estimated based on adding H_2-containing product gas from the decomposition/reforming process into the intake manifold that will partially replace gasoline input of the engine. The combustion of carbon-free species in the product gas (e.g. H_2 and NH_3) will result in CO_x-free exhaust gas product. Hence, tail-pipe CO_2 emission reduction can be realised. Assumptions are made such as complete combustion of all combustible species (e.g. H_2, NH_3, CO, and THCs), stoichiometric combustion (ϕ=1), and unchanged brake thermal efficiency (η_{th}).

GDI engine parameters such as mass air flow rate, baseline mass fuel flow rate ($\dot{m}_{gasoline,baseline}$), % EGR dilution rate, exhaust gas temperature and exhaust gas compositions, need to be quantified. Baseline gasoline molar flow rate ($\dot{y}_{gasoline,baseline}$ in mol/h) can be calculated using the following **Equation 3-11**.

$$\dot{y}_{gasoline,baseline} = \dot{m}_{gasoline,baseline}\left(\frac{kg}{min}\right) \times \frac{60}{1}\frac{min}{h} \times \frac{1}{99.9992}\frac{kmol}{kg} \times \frac{1000}{1}\frac{mol}{kmol}$$

Equation 3-11

Utilising the calculated $\dot{y}_{gasoline,baseline}$ to write the stoichiometric combustion equation of gasoline at which gives the baseline number of moles of CO_2 before adding the H_2-containing product gas into the engine. Product gas compositions molar analysis is required to determine molar fraction for writing combustion equations in dual fuel mode (combustion of gasoline + product gas).

Product gas flow rate ($\dot{m}_{product}$) can be determined by estimating the EGR flow rate based on the % dilution in equations **Equation 3-12**.

$$EGR\ or\ REGR\ rate\ (\%) = \left(\frac{CO_{2,intake} + CO_{2,ambient}}{CO_{2,exhaust} + CO_{2,ambient}}\right) \times 100\% \qquad \textbf{Equation 3-12}$$

Alternatively, EGR rate is defined with **Equation 3-13**.

$$EGR\ (\%) = \frac{\dot{m}_{EGR}}{\dot{m}_{intake}} \times 100\% \qquad \textbf{Equation 3-13}$$

As $\dot{m}_{product} = \dot{m}_{EGR}$ because exhaust used for H_2 production is the same exhaust stream of the EGR system. Hence, total energy output in the product gas ($\dot{Q}_{product}$) can be calculated via **Equation 3-14**.

$$\dot{Q}_{product} = \sum_i \dot{x}_i \times \dot{m}_{product} \times LHV_i \qquad \textbf{Equation 3-14}$$

Where, $\dot{x}_i$ is mass fraction of gas species in the product gas, $\dot{m}_{product}$ is mass flow rate of the product gas (kg/s), and LHV_i is lower heating value of gas species in the product gas (kJ/kg).

Gasoline fuel mass flow rate after using the product gas ($\dot{m}_{gasoline,REGR}$) is the difference between mass flow rate at baseline and after part of gasoline is replaced ($\dot{m}_{gasoline,replaced}$) (referred to **Equation 3-7**) with product gas as shown in **Equation 3-15**.

$$\dot{m}_{gasoline,REGR} = \dot{m}_{gasoline,baseline} - \dot{m}_{gasoline,replaced} \qquad \textbf{Equation 3-15}$$

After using product gas for combustion, the number of moles of CO_2 is lower than that of the baseline combustion condition. CO_2 reduction can be calculated using **Equation 3-16**.

$$\%CO_2\ reduction = \frac{\dot{y}_{CO_2,REGR} - \dot{y}_{CO_2,baseline}}{\dot{y}_{CO_2,baseline}} \times 100\% \qquad \textbf{Equation 3-16}$$

Where, $\dot{y}_{CO_2,REGR}$ is molar flow rate of CO_2 after using reformate gas in REGR configuration, and $\dot{y}_{CO_2,baseline}$ is molar flow rate of CO_2 before using reformate (baseline condition).

The comparison between conventional life cycle of CO_2 from the scenario of utilising e-fuel in the internal combustion engine (ICE) and using e-fuel in both ICE and fuel reformer system is illustrated in **Figure 3-18**. The proposed method of using e-fuel in the ICE engine together with the fuel reformer system is expected to further enhance CO_2 reduction because of the improved combustion efficiency and thermal efficiency by H_2 derived from carbon neutral H_2 carriers.

CO_2 reduction by NH_3 decomposition (Chapter 4)

The product gas from NH_3 direct decomposition only consists of H_2, NH_3, and N_2. This will result in the calculated tail-pipe (tank-to-wheel) CO_2 reduction in proportion to the amount of NH_3 input. Meanwhile, the product gas from NH_3 decomposition with GDI engine exhaust gas contains additional gas species originate from the GDI exhaust gas and through reforming reactions. For instance, CO, THCs, CO_2, and H_2O. C-containing species (CO and THCs) will end up as CO_2 for a complete combustion process (at stoichiometric). This CO_2 from the product gas combustion is included in the tail-pipe exhaust stream for the CO_2 reduction calculation. On the other hand, as part of exhaust gas stream is recirculated in the GDI engine, therefore; CO_2 in the EGR stream is excluded from calculation.

CO_2 reduction by urea decomposition (Chapter 5)

Urea decomposition in N_2+O_2 mixture and with GDI exhaust gas produce product gas consists of H_2, NH_3, CO_2, CO, THCs, and N_2. There are two sources of CO_2 in the reactant feed: from EGR stream and from hydrolysis of HNCO. In this research, CO_2 from both sources is excluded from CO_2 reduction calculation. CO_2 in EGR stream is omitted as explained earlier for NH_3 decomposition study. For CO_2 from HNCO hydrolysis reaction is excluded because 'green urea' (carbon-neutral) is chosen. CO_2 reduction here is considered using well-to-wheel point of view.

CO_2 reduction by carbon-neutral hydrogen carriers (Chapter 6)

This chapter utilises urea in combination with e-fuel candidates (ethanol and methanol) which are considered as carbon-neutral hydrogen carriers. Using the same assumption (well-to-wheel analysis) as performed in chapter 5, therefore; CO_2 produced from combustion process of product gas is excluded from CO_2 reduction calculation.

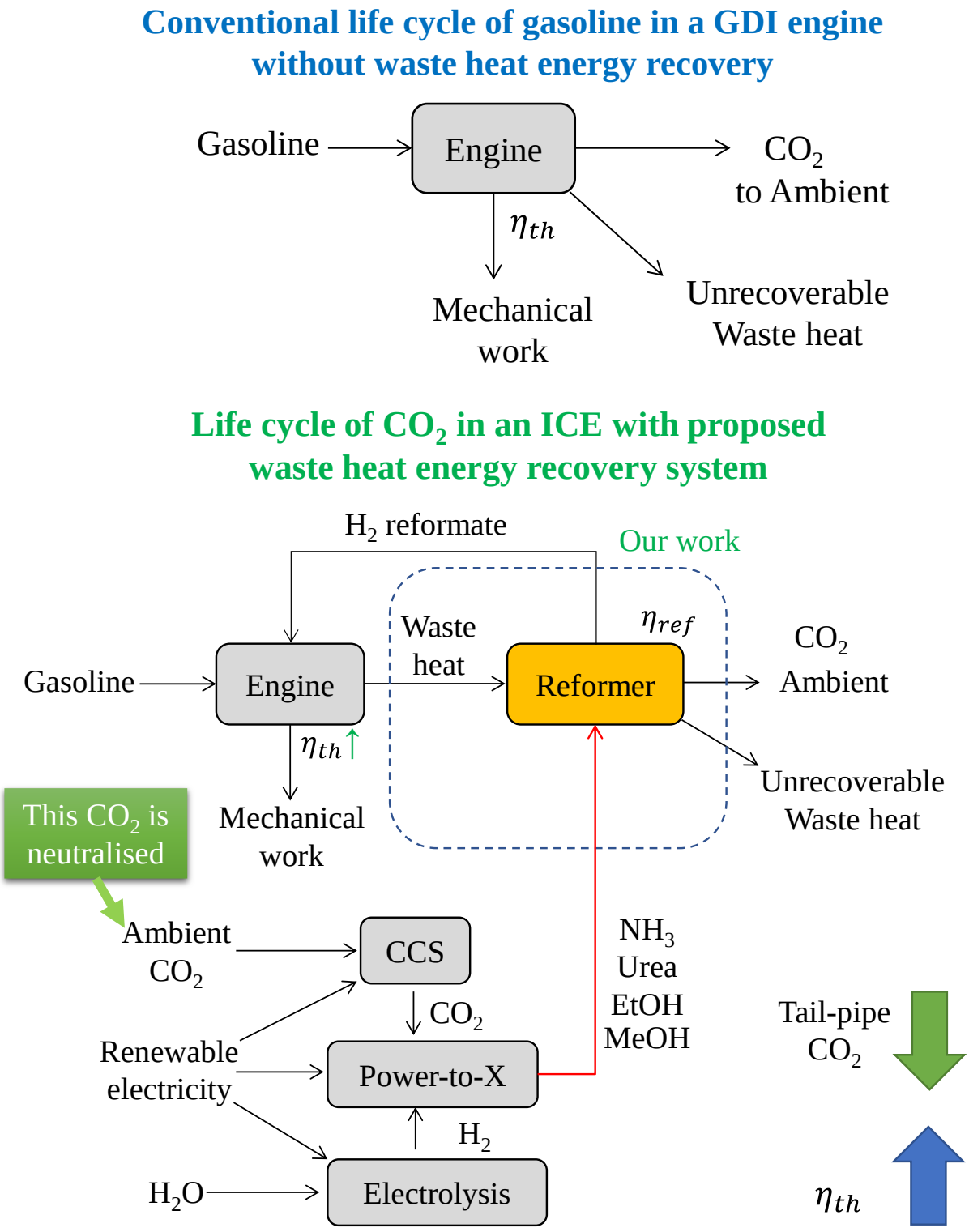

Figure 3-18: Impact of proposed H_2 production system on CO_2 emission

Chapter 4 Energy recovery via catalytic ammonia decomposition for on-board hydrogen production*

4.1 Introduction

In this chapter, experimental hydrogen production from ammonia feedstock using Rh-Pt catalyst in the laboratory scale is discussed in comparison to equilibrium calculations. First, the investigation on the effects of operating conditions of NH_3 direct decomposition via NH_3 cracking (e.g. catalyst inlet temperature, GHSV, inlet NH_3 concentrations) on the product gas compositions, decomposition efficiency, and ammonia conversion efficiency were examined. The later section focuses on the study of NH_3 decomposition with GDI engine exhaust gas to examine potential benefits of H_2 produced from NH_3 for GDI engine performance and emissions improvements.

4.2 Experimental conditions

4.2.1 Ammonia direct decomposition

For the NH_3 direct decomposition experiment was performed to observe the baseline performance such as process efficiency and ammonia conversion efficiency of the Rh-Pt reforming catalyst. There was only NH_3 and N_2 in the reactant, hence, maximum H_2 production efficiency by Rh-Pt catalyst from NH_3 decomposition reaction ($2NH_3 \rightarrow 3H_2+N_2$ reaction) could be determined. Inlet NH_3 concentrations of 1.00%-vol, 2.00%-vol and 4.45%-vol were chosen to study NH_3 decomposition characteristics at different NH_3 concentrations. GHSV between 16000 h^{-1} and 20000 h^{-1} were utilised based on high NH_3 conversion efficiency reported in previous works [45], [88]. NH_3 direct decomposition experiment conditions are tabulated in **Table 4-1**.

*This chapter is published as a journal article.

Table 4-1 Experiment conditions for NH_3 direct decomposition experiment

Condition	GHSV (h^{-1})	NH_3 flow rate (g/h)	NH_3 %-vol	N_2 %-vol
1	16000	3.358	1.00	99.00
2	16000	6.716	2.00	98.00
3	16000	14.943	4.45	95.55
4	20000	18.678	4.45	95.55
5	16000	15.241	5.00	95.00

4.2.2 Ammonia decomposition with GDI exhaust gas

For NH_3 decomposition with GDI engine exhaust gas experiment, inlet NH_3 concentration of 1.00% was selected and designated O_2/NH_3 ratio could be achieved by varying amount of exhaust gas and N_2 was supplied as inert filler to maintain total GHSV of 24,000h^{-1}. Inlet catalyst temperature of 650°C was chosen based on high H_2 concentration, low NH_3 slippage, and high process efficiency. Such temperature was also attainable with GDI engine operated at part load condition. Experiment conditions are as shown in **Table 4-2**.

Table 4-2 Experiment conditions for ammonia decomposition with GDI exhaust gas

Condition	O_2/NH_3	H_2O/NH_3	Reactant feed concentrations		
			NH_3 (%)-vol	Exhaust (%-vol)	N_2 (%-vol)
1	0.078	1.645	1.00	12.5	86.5
2	0.234	3.705	1.00	28.2	70.8
3	0.313	5.015	1.00	38.1	60.9

4.3 Ammonia direct decomposition

4.3.1 Effects of decomposition temperature and ammonia concentration

Equilibrium calculations predict 100% NH_3 conversion efficiency (**Figure 4-1B**) can be achieved from gas temperature of approximately 400°C where negative Gibbs free energy of NH_3 cracking reaction is indicated (**Figure 4-1C**), while the experimental results indicate that almost complete NH_3 decomposition was attained around 550°C, as shown in **Figure 4-1B**. The H_2 selectivity (as shown in **Figure 4-1D**) of NH_3 decomposition reaction is strongly dependent on the inlet gas temperature and initial NH_3 concentration [81]. For low inlet NH_3 concentration condition (3.358 g/h NH_3), almost complete NH_3 conversion with efficiency ranging from 95% to 98% in the range of 550°C to 650°C. The process efficiency of 114.59% (**Figure 4-1A**) is reached. The process efficiency is close to the theoretical efficiency at equilibrium state of 115% indicating that heat is recovered, and the enthalpy of the fuel is increased by approx. 15%. However, at elevated NH_3 concentration (14.943 g/h NH_3), a noticeable reduction for both NH_3 conversion efficiency and process efficiency can be identified, especially at low temperature regions (<550°C). The preliminary findings reveal the possibility to recover energy from exhaust gas through NH_3 decomposition with exhaust gas reforming. For instance, at 14.942 g/h of input NH_3 or 76W (equivalent) is introduced to the laboratory-scale reformer, then product reformate gas produced from this process will have approximately 85W or 11% more enthalpy than the original reactant feed.

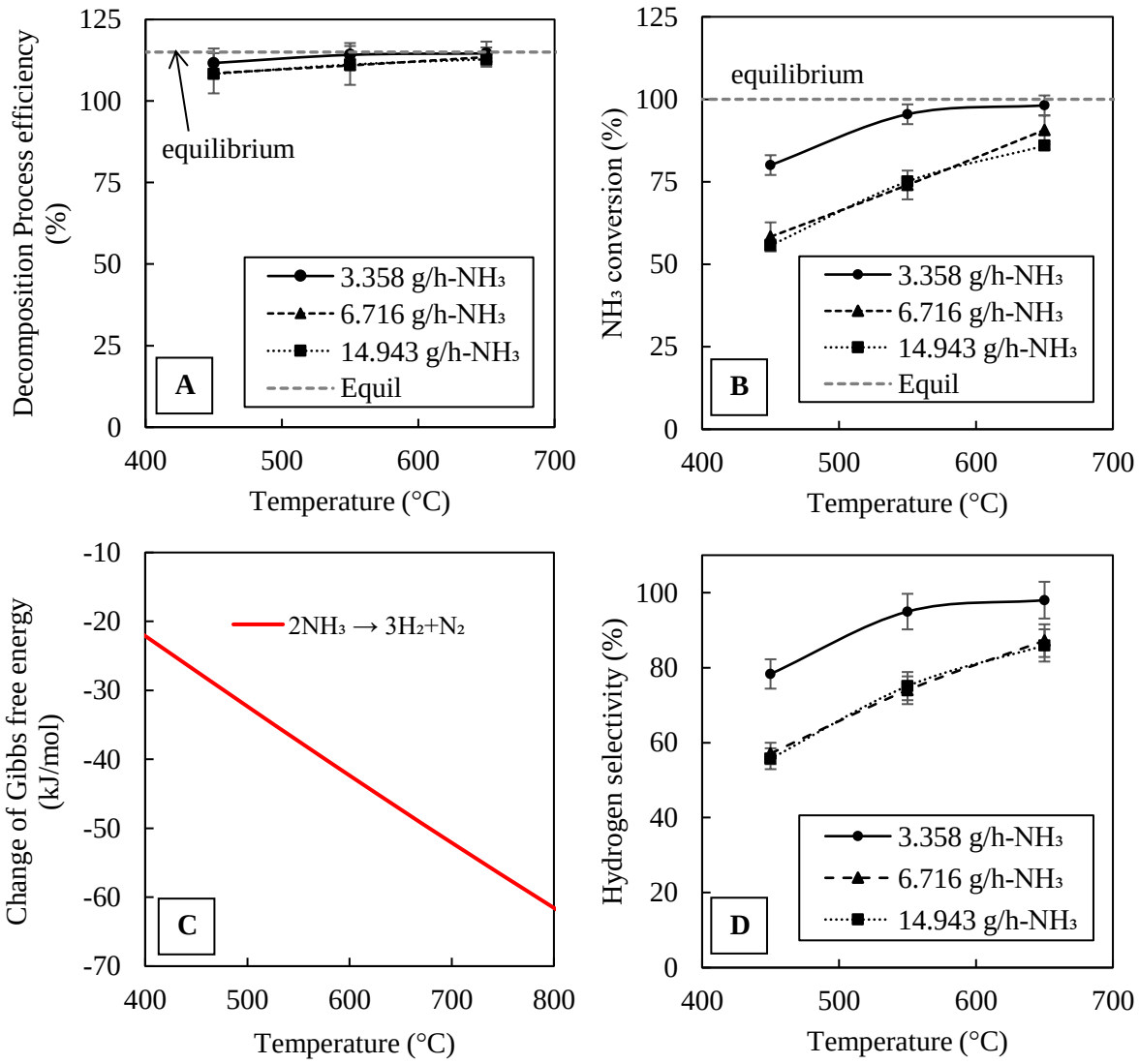

Figure 4-1: Process efficiency (A), ammonia conversion (B), change of Gibbs free energy of NH_3 decomposition (C), and hydrogen selectivity (D)

For a full-scale engine application where up to approximately half a litre (Projected volume) of NH_3 decomposition catalyst is used for energy recovery process. Using information from previous study [6] to estimate available energy within the exhaust gas (as heat energy referred as 'exhaust exergy') is approximately 50% of engine output power. Taking every information into account (also assuming process efficiency from corresponding conditions)

from conditions 3 and 4 in **Table 4-1**. This results in enthalpy increase, as shown in **Figure 4-2**, ranging from 2.77 kW to 3.99 kW if NH_3 equivalent input of 23.76 kW and 29.69 kW are used, respectively. Based on a GDI engine operating condition of 148 Nm and 2500 rpm, which represents typical engine condition for multi-cylinder gasoline engines [7]. The use of H_2 produced from proposed system demonstrates the potential to decrease fuel consumption and tail-pipe CO_2 emission up to 30.43% from baseline.

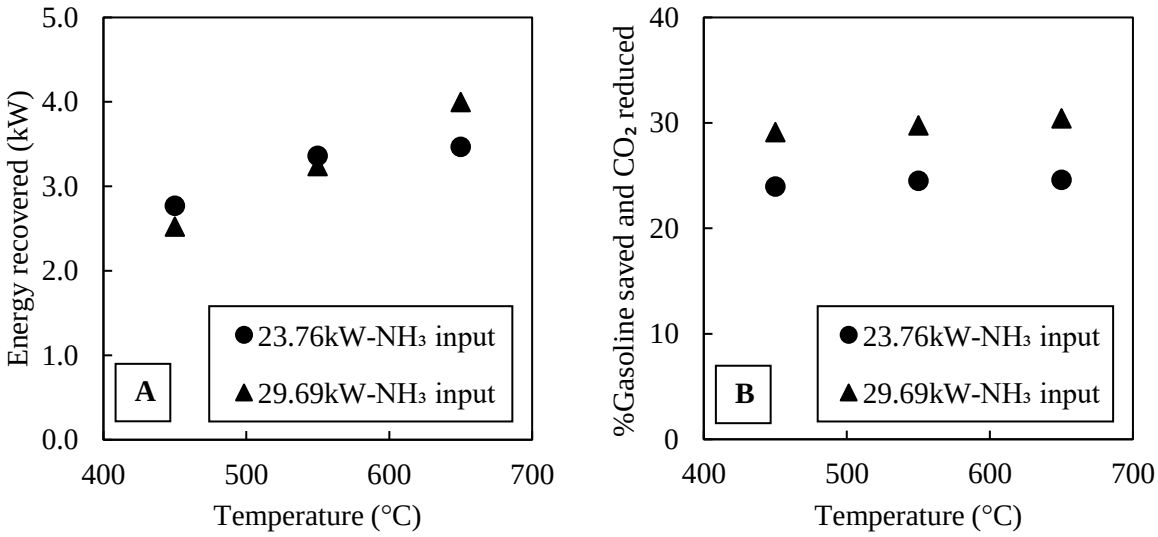

Figure 4-2: Estimated energy recovery (A) and gasoline saving and CO_2 reduction (B) via ammonia direct decomposition calculated at GDI engine operation of 148 Nm/2500 rpm.

4.3.2 Effects of gas hourly space velocity

The effect of GHSV on NH_3 conversion efficiency and process efficiency are investigated by varying total volumetric flow rate of NH_3+N_2 mixtures resulting in GHSV of 16000 h^{-1} and 20000 h^{-1} (experiment condition 3 and 4, respectively). The increase of GHSV results in a noticeable decrease for both NH_3 conversion efficiency and process efficiency as illustrated in **Figure 4-3**. The reduced NH_3 conversion efficiency is the result of the shorter residence time (or less contact time [98]) between reactant (NH_3) and the catalyst active sites.

Moreover, the NH_3 dehydrogenation process is restricted by NH_3 molecules adsorption rate onto the catalyst's active site. It is followed by N-H bond cleavage (splitting), recombination of nitrogen atom, and dinitrogen desorption processes [81], [82] at temperatures below 377°C (650K) [83]. N_2 desorption process is primarily the rate-limiting step of ammonia cracking process [84]. The process efficiency slightly declines at elevated temperature (650°C) and substantially decreases at the lower catalyst inlet temperatures (e.g. at 550°C) as the results of heat transfer constraints. Heat transfer limitation restricts the ammonia cracking process to reach its ideal equilibrium [98].

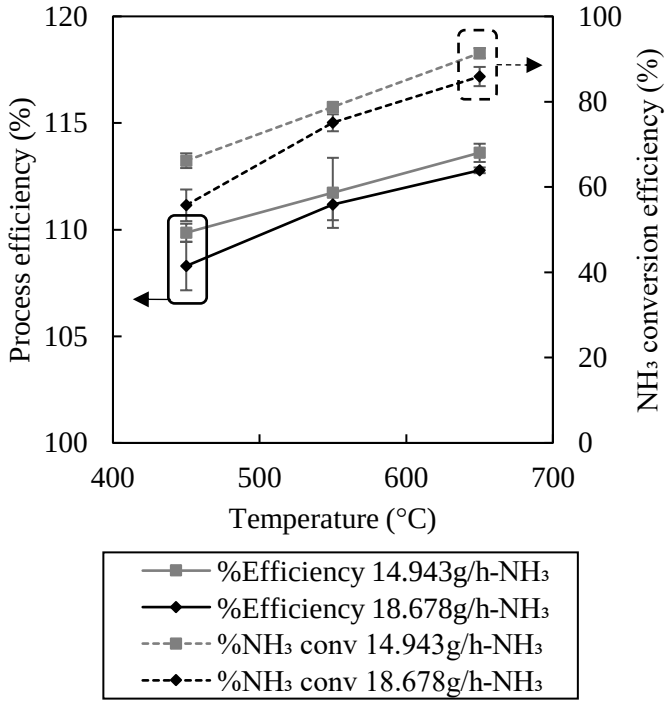

Figure 4-3: Effect of GHSV on process efficiency and ammonia decomposition.

4.3.3 Energy recovery prediction

Heat required to convert ammonia into hydrogen and nitrogen based on ammonia's enthalpy of reaction (ΔH°_{298K}) is illustrated in **Figure 4-4A**. For instance, 4.31 kW of heat energy is required to decompose the equivalent 29.69 kW of NH_3, which is within the heat

energy available in the exhaust gas. **Figure 4-4B** illustrates the calculations of available exhaust heat energy (exergy) of a multi-cylinder gasoline engine at typical engine operating conditions [7] assuming an exhaust gas exergy efficiency of 50% from the GDI engine according to Fennell et al. [6]. The exergy estimations demonstrate that different engine operating conditions affect the amount of maximum NH_3 can be decomposed via $2NH_3 \rightarrow 3H_2 + N_2$ reaction. Hence, the amount of maximum H_2 can be produced is proportional to engine output power.

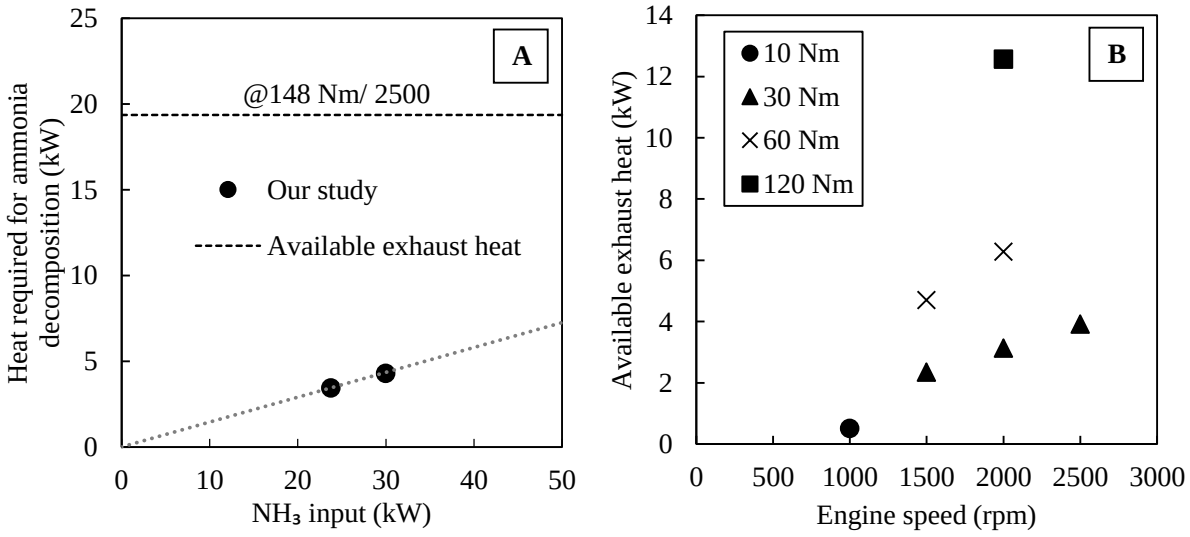

Figure 4-4: Heat energy requirement for ammonia decomposition (A) and available energy in exhaust heat at various engine conditions (B).

According to the ICCT (International Council on Clean Transportation) 2018/19 report [50] , most passenger vehicles in the European countries were able to comply with the 2015 regulation regarding the CO_2 emission limits (as blue line shown in **Figure 4-5**). Although, the abovementioned commercial vehicles would not comply with the 2020/21 CO_2 emission limit target with the current aftertreatment technologies implemented in the vehicles on the market. **Figure 4-5** demonstrates the anticipated value of potential CO_2 reduction via utilising H_2 generated from NH_3 through exhaust gas waste heat energy recovery technique. Based on the process efficiency from previously discussed results, with optimised catalyst, gas hourly space

velocity, and improved reformer heat transfer, the higher H_2 yield can be produced. Hence, it is possible to extend CO_2 emission reduction from GDI engines up to 30.4% from its baseline emission level. The optimised thermochemical energy recovery system can facilitate ICE-powered passenger vehicles to comply with 2020/21 greenhouse emission targets and it is expected to meet the 2030 greenhouse gas emission target.

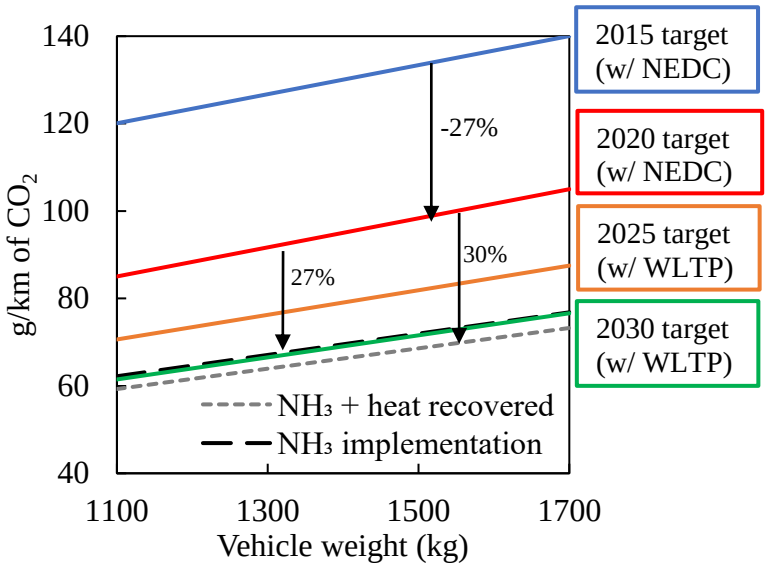

Figure 4-5: Predicted CO_2 reduction of passenger vehicle by using hydrogen from ammonia decomposition to replace gasoline fuel

4.4 Ammonia decomposition with GDI engine exhaust gas

4.4.1 Effect of decomposition temperature

Product gas compositions by an equilibrium calculation of NH_3 decomposition with GDI exhaust gas at O_2/NH_3 of 0.234 are as shown in **Figure 4-6A**. H_2 concentration increases with decomposition temperature from 350°C and reaches the peak H_2 concentration at approximately 500°C because of enhanced NH_3 decomposition, SR of THCs, and WGS reactions as indicated the further decrease of Gibbs free energy illustrated in **Figure 4-6B**. Meanwhile, O_2 in the reactant mixture is mostly consumed mainly by oxidation reactions e.g.

NH_3+O_2, THC + O_2, CO + O_2 and H_2 + O_2 reactions. Among oxidation reactions, H_2 + O_2 reaction is the most reactive and other reactions (oxidation of NH_3, CO, and THCs) would proceed after H_2 (H_2 that came with GDI exhaust gas, 0.23%-vol) is completely consumed [96].

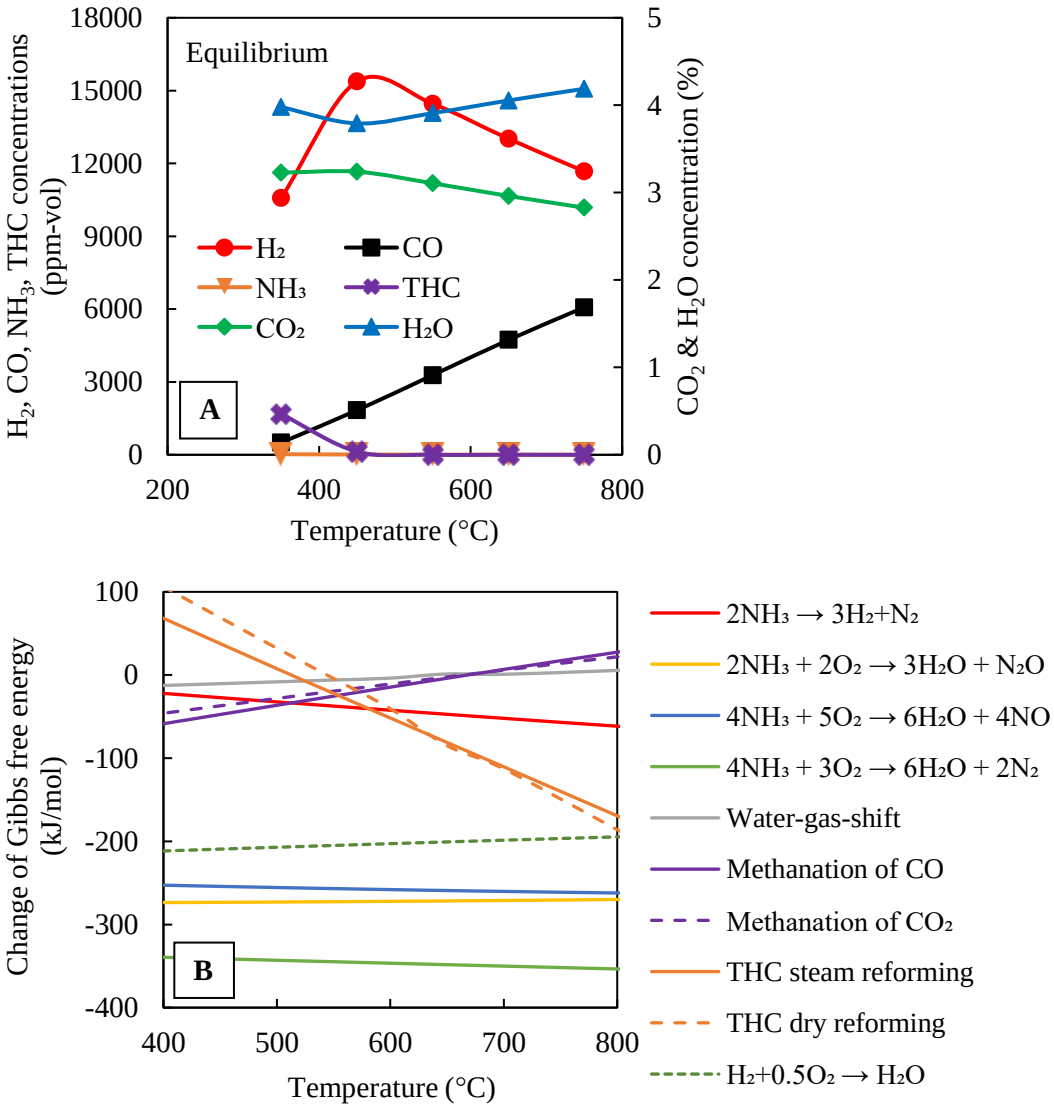

Figure 4-6: Equilibrium prediction of product gas compositions from NH_3 decomposition in exhaust gas at O_2/NH_3 = 0.234 (A) and change of Gibbs free energy of reactions involved NH_3 decomposition in GDI exhaust gas (B)

Trace amounts of NH_3 and THCs (mainly, CH_4) in the product gas is predicted by the equilibrium calculation at low temperature regions (350 to 450°C) as the result of in-situ NH_3 formation and methanation reaction. NH_3 is formed as the result of NO + H_2 and NO + CO + H_2 reactions which competes with the H_2 + O_2 reaction. At low temperature, H_2 presence in reactant feed is reported [96] which demonstrate almost identical affinity to react with NO and O_2. Meanwhile, H_2 is more favoured to react with O_2 at higher temperature. As decomposition temperature increases, methanation reaction is suppressed and WGS reaction is reversed. This is predicted by the increase of the change of Gibbs free energy indicating the tendency of the methanation and WGS reactions to progress in reverse direction as shown in **Figure 4-6B**. This results in the decline of H_2 and CO_2 concentrations, and the increase of CO and H_2O concentrations in the product gas [19].

4.4.2 Effects of O_2/NH_3 ratio

Figure 4-7 illustrates equilibrium calculation and experimental product gas compositions of NH_3 decomposition with GDI exhaust gas at temperature of 650°C and O_2/NH_3 between 0.078 to 0.313. The experiment results reveal the highest H_2 yield at O_2/NH_3 ratio of 0.078 because of lower O_2 fraction in reactants. This leads to the limited consumption of H_2 and NH_3 through $H_2 + 0.5O_2 \rightarrow H_2O$, $NH_3 + O_2 \rightarrow H_2O + N_2$ and $4NO + 4NH_3 + O_2 \rightarrow 6H_2O + 4N_2$ reactions. The increased O_2/NH_3 ratio (more exhaust flow rate, and constant NH_3 inlet flow rate) causes the reduction of H_2 concentration and increase NH_3 slippage. This is due to the higher degree of H_2 + O_2 reaction and catalytic inhibition of NH_3 decomposition by H_2O presence [168]. H_2O concentration in reactant mixture is proportional to the volumetric amount of exhaust gas introduced. In this case, the H_2O/NH_3 ratio is directly proportional to O_2/NH_3 ratio. The presence of H_2O inhibits NH_3 decomposition by its molecular adsorption effect on

catalyst's active sites. As H_2O competes with NH_3 regarding the adsorption onto the reforming catalyst's active sites [169]. However, the inhibition by H_2O adsorption is reversible and became negligible at elevated temperature [168].

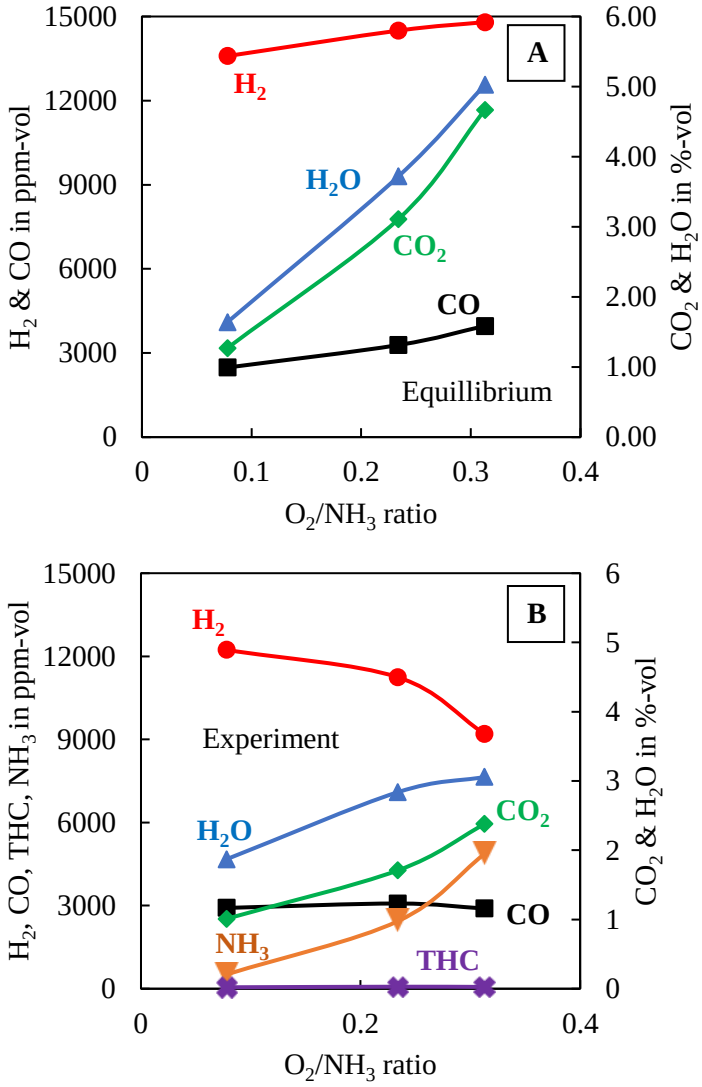

Figure 4-7: Equilibrium calculations (A) and experimental results (B) of NH_3 decomposition with GDI exhaust gas

At O_2/NH_3 = 0.313, the experimental results indicate as high as 48.66% unconverted NH_3 in the reformate gas stream. This indicates that 5134 ppm of NH_3 is decomposes into 7701 ppm of H_2 assuming theoretical conversion efficiency of ammonia. Therefore, it is assumed

that the remaining H_2 is originated from other reaction routes. However, the high amount of NH_3 slippage is thought to be due to the in-situ NH_3 formation though $NO + 2.5H_2 \rightarrow H_2O + NH_3$ and $NO + CO + 1.5H_2 \rightarrow CO_2 + NH_3$ reactions. Ammonia formation is promoted by high selectivity of platinum catalyst in the direction of NH_3 formation as previously described by [96]. The availability of NO and CO in exhaust gas, and the net reducing condition also contributes to ammonia formation.

4.4.3 Process efficiency and ammonia conversion efficiency

Figure 4-8 illustrates the equilibrium calculation and experimental of process efficiencies and ammonia conversion efficiencies for NH_3 decomposition with GDI exhaust gas. In general, process efficiency indicated in the experimental results demonstrates comparable trends to the equilibrium calculations despite lower H_2 yield in the product gas. Similar process efficiencies between equilibrium calculations and experiments are due mainly to significant concentration of NH_3 in the product gas. This results in a substantial contribution of product output energy. Up to 119% of process efficiency is achieved in the experiment at O_2/NH_3 of 0.313. This indicates that heat energy is recoverable through NH_3 decomposition in exhaust gas. Although the experiment results indicate noticeable concentration of NH_3 in product gas as the result of catalyst inhibition by H_2O in exhaust gas as O_2/NH_3 ratio increases. There is a trade-off between the process efficiency of the system and NH_3 slippage in the reformate stream. This requires a careful consideration when operating the proposed system in real world applications.

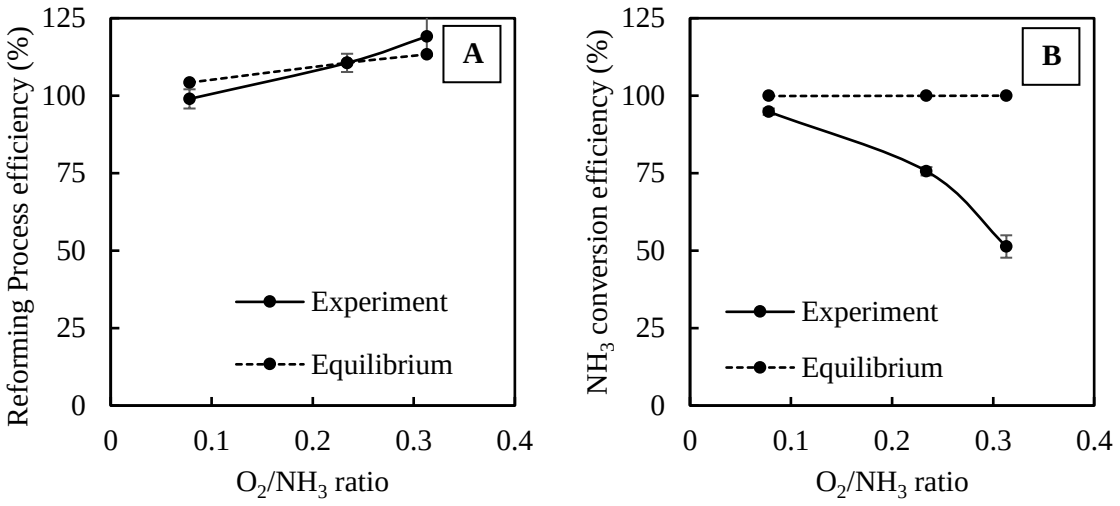

Figure 4-8: Effect of O_2/NH_3 molar ratio on process efficiency (A) and ammonia conversion efficiency (B) of NH_3 decomposition with GDI exhaust gas

The estimation of a full-scale vehicular application is calculated using the same input ammonia energy density (**Table 4-1**) as discussed previously in the ammonia direct decomposition section. The recoverable energy (**Figure 4-9A**) increases with the increase of O_2/NH_3 ratio which also improves with process efficiency illustrated in **Figure 4-8A**. Energy recovery is achievable when the O_2/NH_3 ratio is greater than 0.078. Additional heat from the autothermal-reforming process (ATR) [7], [13], [45] assists sustaining the NH_3 cracking reaction and enhances the process efficiency. Although, at a lower O_2/NH_3 ratio (e.g. at O_2/NH_3 = 0.078), a negative value of fuel energy recovery is observed (**Figure 4-9A**). This indicates that partial loss of ammonia input energy during the decomposition process because of complete oxidation or partial oxidation process.

Figure 4-9B illustrates the estimated value of gasoline fuel saving and tail-pipe CO_2 reduction by feeding H_2 generated from NH_3 back into the intake manifold in REGR configuration [88] of a GDI engine at 148 Nm/ 2500 rpm. According to this estimation, only energy (low heating value) of H_2 and NH_3 are considered. Complete energy conversion by

combustion in the GDI engine when fuelling with H_2 derived from NH_3 decomposition is assumed. Due to CO_x-free characteristics of H_2 and NH_3, the magnitude of gasoline fuel saving, and CO_2 reduction are indistinguishable. In comparison, insignificant enhancement of gasoline fuel saving, and CO_2 reduction can be observed between using H_2 derived from direct NH_3 decomposition and NH_3 decomposition with GDI exhaust gas (30.43% and 31.96%, respectively).

In a real-world operating condition, additional intrinsic gas compositions (e.g. CO and THCs) in the product gas will be introduced along with H_2 reformate via intake manifold. Thus, the potential gasoline fuel saving will be marginally improved. On the assumption that CO and THCs participate in the combustion process. Although, a worsened tail-pipe CO_2 reduction is expected due to the contribution of carbon components available in the product gas which generates CO_2.

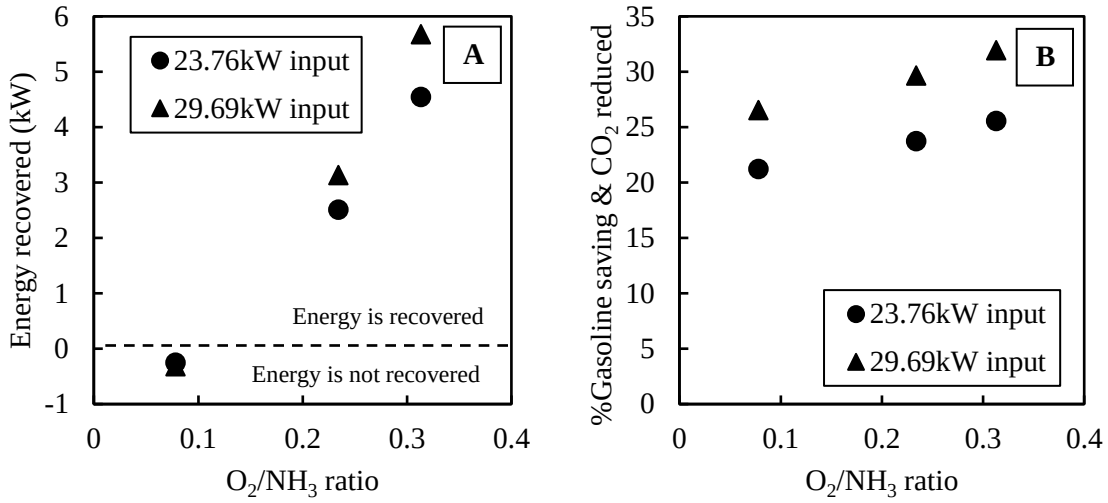

Figure 4-9: Estimated energy recovery (A) and gasoline fuel saving and CO_2 reduction (B) by using hydrogen from ammonia decomposition with GDI exhaust gas

4.5 Ammonia and gasoline energy life cycle and carbon footprint

Energy consumption and CO_2 emission of ammonia production compared to gasoline production through various production methods (refer to **Table 4-3** for the chart's legends) are illustrated in **Figure 4-10**. The most conventional method of ammonia production is gas synthesis via methane steam reforming (points 1A, 4A, 5A and 7A). With this production method, specific CO_2 emissions per unit energy of end-product ranges between 76 to 112 $gCO_2/MJ_{ammonia}$. Meanwhile, energy requirement to produce ammonia is between 1.35 to 2.00 $kJ/kJ_{ammonia}$. The production and utilisation of gasoline fuel releases approximately 80 $gCO_2/MJ_{gasoline}$ and required average energy of 1.17 $kJ/kJ_{gasoline}$ for production process. Therefore, approximately 5% reduction in CO_2 emission can be realised if ammonia from a highly efficient production system is used in comparison with gasoline. Given the on-board fuel reforming efficiency improvement (30%) is considered, the possible reduction in CO_2 emissions of 30% is expected when replacing fuel with H_2 derived from NH_3 decomposition. Moreover, ammonia production will phase out from using fossil fuel feedstocks and progress towards 'green ammonia' production with H_2 from electrolysis driven by renewable energy [170]. Carbon footprint of NH_3 from renewable energy is depicted as points 8A to 11A in **Figure 4-10**. The potential CO_2 emissions reduction of up to 75% is anticipated.

Table 4-3 Summary of energy requirement and CO_2 emission of fuel productions.

Figure 4-10 designation	**Fuel**	**Energy cost (kJ/kJ)**	**CO_2 cost (gCO_2/MJ)**	**Reference**
1A	Ammonia	1.85	94	[171]
2A	Ammonia	2.51	141	[80]
3A	Ammonia	1.40	0	[172]
4A	Ammonia	2.00	112	[173]
5A	Ammonia	1.35	76	[174]
6A	Ammonia	2.18	122	[175]
7A	Ammonia	1.55	87	[175]
8A	Ammonia	2.34	20	[176]
9A	Ammonia	4.20	45	[176]
10A	Ammonia	6.49	46	[176]
11A	Ammonia	8.55	18	[176]
12A	Ammonia	2.15	120	[177]
1G	Gasoline	1.22	81	[178]
2G	Gasoline	1.12	79.85	[179]
3G	Gasoline	1.10	75	[180]
4G	Gasoline	1.02	73	[181]
5G	Gasoline	1.31	87.01	[182]
6G	Gasoline	1.11	81.09	[183]
7G	Gasoline	1.97	123.91	[184]

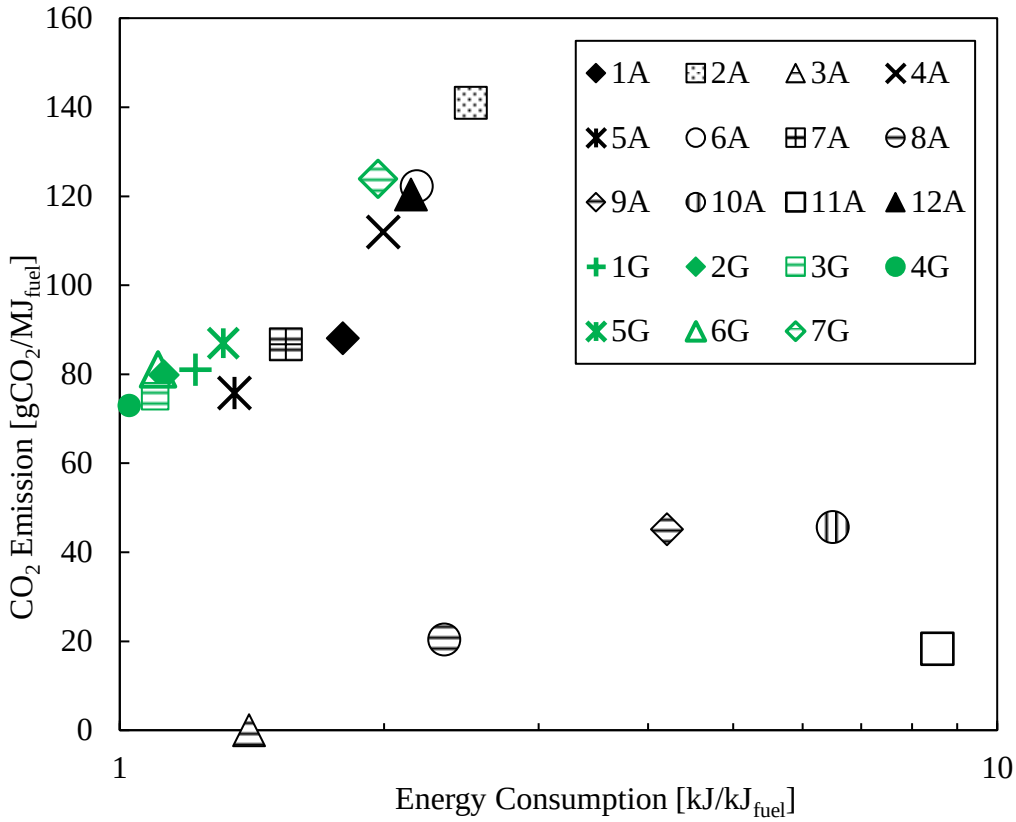

Figure 4-10: Comparative amounts of CO_2 emissions and energy required for ammonia and gasoline productions.

4.6 Summary

This chapter examines the on-board H_2 production from NH_3 decomposition through GDI engine's exhaust energy recovery. The thermochemical energy recovery study is evaluated under two scenarios: using only heat energy from exhaust gas for direct decomposition of NH_3 and using part of exhaust gas and heat energy for NH_3 decomposition. The equilibrium calculations are validated with the experimental results.

The results from direct NH_3 decomposition experiment demonstrates the dependence of decomposition process on the gas temperature which affects the forward rate of NH_3 cracking reaction. The amount of heat energy recovery is a direct function of the decomposition

temperature and input mass flow rate of NH_3. While the tailpipe CO_2 reduction is rather a function of input NH_3 flow rate which directly influences the gasoline fuel replacement.

For NH_3 decomposition with GDI exhaust gas experiment indicates that the H_2 production process is largely dependent on the intensity of oxidation reaction induced by the presence of O_2 in the exhaust gas. The presence of H_2O in exhaust gas also leads to catalytic inhibition of NH_3 cracking which H_2O competes with NH_3 to adsorb onto catalyst active sites and negatively affects NH_3 conversion efficiency. Overall, oxidation reactions can assist energy recovery and GHG reduction.

The COx-free H_2 produced from NH_3 decomposition enables partial replacement of gasoline which demonstrates a prospective in enhancing the fuel economy and reduction of greenhouse gas emissions from the GDI engine. Up to 30% reduction of fuel consumption and CO_2 emissions can be realised using H_2 derived from NH_3 decomposition. CO_2 life cycle analysis verifies the benefit of using NH_3 as H_2 carrier. Especially, if NH_3 produced using renewable energy which indicates potential to achieve further CO_2 reduction compared to gasoline usage.

Chapter 5 Aqueous urea decomposition

5.1 Introduction

In the previous chapter, hydrogen production from NH_3 is investigated which revealed the potential of waste heat energy recovery and CO_2 reduction. While NH_3 is established as one of promising H_2 carrier candidates, urea is considered as a safer and energy-denser form to store NH_3 [121]. Aqueous urea solution (AUS32) can be used as H_2 carrier for on-board hydrogen production due to its advantages, for instance, easy handling, fire safety, ease of fuelling control, and end-user availability. The aim of this chapter is to investigate the hydrogen production from aqueous urea solution in two different scenarios; to imitate using only exhaust gas heat for oxidative decomposition process (performed in N_2+O_2 mixture) and using both heat and gas species in exhaust gas to decompose AUS32. This chapter develops an understanding of the influence of gas species in the GDI exhaust gas (namely, CO_2, H_2O, CO, THCs) on end-product from urea decomposition through the analysis of thermodynamic equilibrium, and experimental methods. The evaluation on exhaust waste heat energy recovery and CO_2 reduction are examined in the scenario that H_2 produced from AUS32 is supplied back to the GDI engine to replace gasoline fuel. This chapter demonstrates the feasibility to produce H_2 on-board and on-demand to enhance the GDI engine thermal efficiency and enable decarbonisation of the transportation sector. The overview of work done in this chapter is illustrated in **Figure 5-1**.

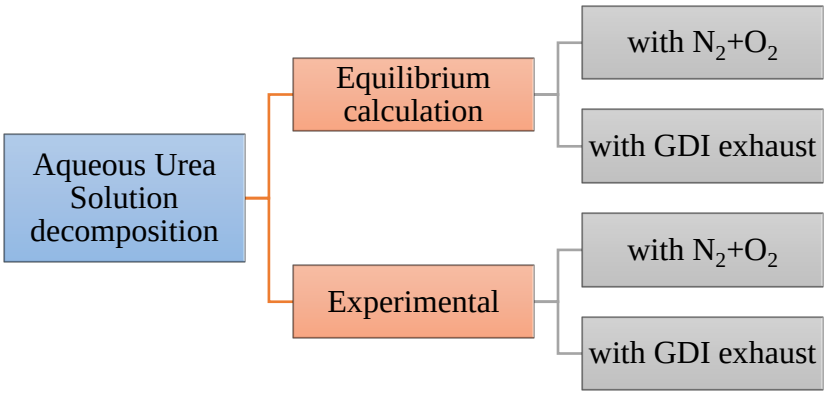

Figure 5-1: Aqueous urea solution decomposition study overview

5.2 Experiment conditions

H_2 production from AUS32 is investigated by both equilibrium calculation and experiments for the two following scenarios: 1) Catalytic decomposition of AUS32 using 0.7% O_2 in N_2 inert gas (Same concentration of O_2 in the GDI engine exhaust gas) and 2) catalytic decomposition of AUS32 with exhaust gas from a GDI engine. AUS32 injection rate is adjusted in the range between 22.99 g/h to 86.24 g/h resulting in the equivalence O_2/NH_3 ratio between 0.04 to 0.15 as shown in **Table 5-1**. These AUS32 injection rates are selected based on previous ammonia exhaust gas decomposition studies [45], [46] which include the decomposition conditions that produced high H_2 yield and decomposition process efficiency.

Table 5-1 AUS32 injection rates

AUS32 injection rate (g/h)	Corresponding theoretical equivalence O_2/NH_3 ratio
22.99	0.15
44.22	0.08
86.24	0.04

This chapter estimates CO_2 reduction based on the available exergy in the exhaust gas from typical engine operating conditions of passenger cars with multi-cylinder gasoline engines [7] as shown in **Table 5-2**.

Table 5-2 Selected engine operating conditions

Condition #	Speed (rpm)	Torque (Nm)	Engine output power (kW)	Brake thermal efficiency (%)	Exhaust gas temperature (°C)
1	2100	30	6.6	24.90	602
2	2100	60	13.2	27.54	685
3	3000	50	15.7	24.55	749
4	2100	105	23.1	32.12	745
5	2500	148	38.7	38.74	802

5.3 AUS32 decomposition in N_2+O_2

5.3.1 Effect of AUS32 injection rate and temperature on product gas compositions

Figure 5-2A illustrates the products at equilibrium of AUS32 decomposition in N_2+O_2 mixture (at $\dot{m}_{AUS32}$=86.24 g/h) as a function of decomposition temperature. The equilibrium calculation predicts the peak H_2 production is between 550°C and 600°C. At lower decomposition temperature, CH_4 is the major carbon species in the gas products because methanation reaction is thermodynamically favourable. Meanwhile, low decomposition temperature leads to the lower forward rate of NH_3 cracking reaction [29] which results in a high concentration of NH_3 in the product gas. Based on the Gibbs free energy (as shown in **Figure 5-3)** which implies the natural tendency of a reaction to spontaneously proceed toward the minimum ΔG value. Overall, an increase in decomposition temperature reduces Gibbs free energy (ΔG) of SR of hydrocarbons, NH_3 cracking, reverse methanation H_2+CO_2↔CH_4+H_2O)

and methane dry reforming (DR) reactions which enhances H_2 production [16], [66]. Meanwhile, ΔG values of WGS and methanation slightly increase with the gas temperature indicating the lower spontaneity of the reaction.

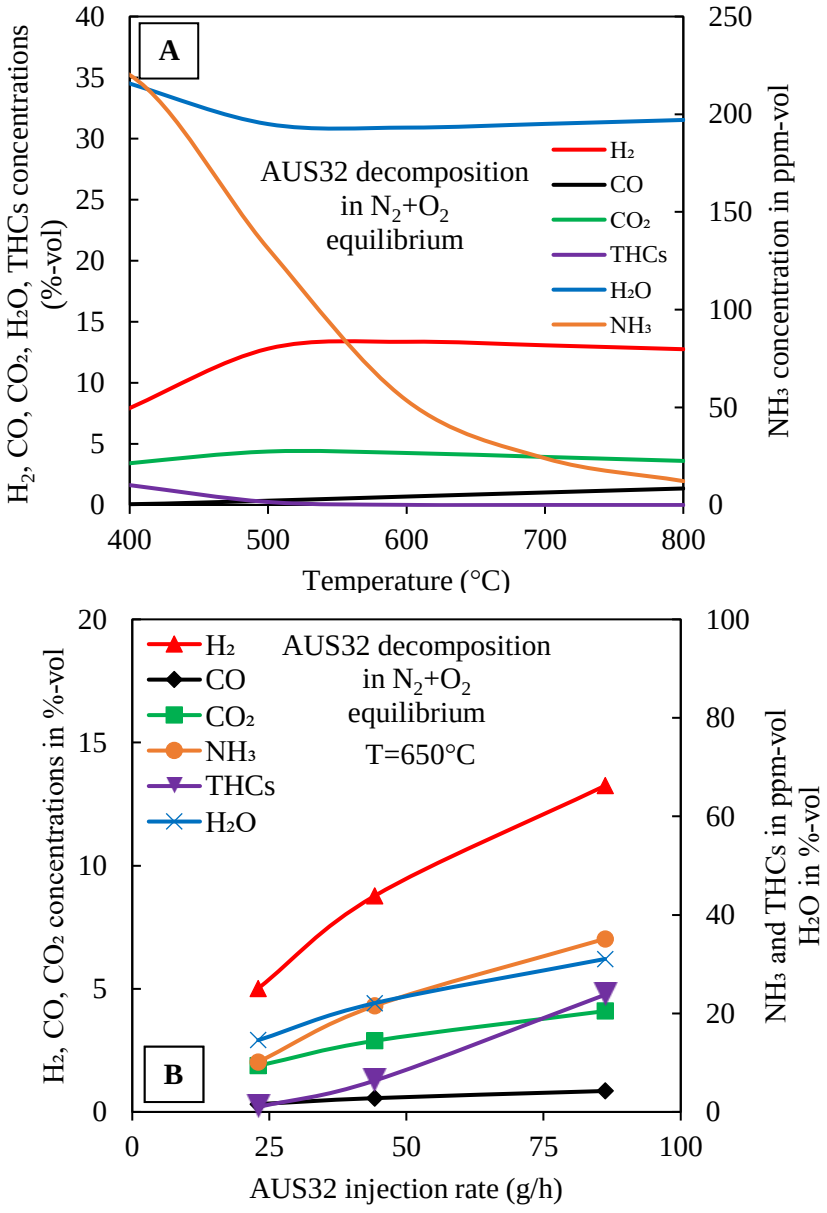

Figure 5-2: Equilibrium calculation of AUS32 decomposition in N_2+O_2 A) effect of temperature, and B) effect of AUS32 injection rate at 650°C

H_2 yield is negatively affected by higher decomposition temperatures due to inhibition of H_2 production which reverse WGS reaction is thermodynamically favoured (as indicated by the increased ΔG of WGS reaction at elevated temperature). CO is produced through WGS reaction. Consequently, CO_2 concentrations in the product gas reduces as decomposition temperature increases. SR and DR reactions of methane and other THCs are viable reaction pathways to generate CO as indicated by gradual reduction of ΔG values. Especially at an elevated temperature where THCs concentration noticeable reduces because of the suppression of methanation reaction.

Figure 5-2B demonstrates the effect of AUS32 injection rate on the product gas compositions at catalyst inlet temperature of 650°C. Generally, the concentrations of H_2, CO, CO_2, NH_3, and THCs in the product gas increase with the AUS32 injection rate as the result of increasing the input H and C atoms in the reactant. The higher AUS32 injection rate implies a greater urea mass flow rate which results in additional H_2 and CO_2 produced via urea cracking reaction (**Equation 2-1**). The higher AUS32 injection rate effectively reduces O_2/C ratio resulting in milder exothermic reactions (e.g. lower degree of NH_3+O_2, H_2+O_2, and THCs+O_2 reactions) and higher degree of endothermic reactions (Urea→H_2+CO_2, SR of THCs, and DR of THCs) that produces H_2.

Figure 5-3 illustrates the change in Gibbs free energy of reactions that are generally involved in the AUS32 decomposition process as a function of decomposition temperature. The substantial negative ΔG values of urea decomposition reactions, including urea thermolysis, hydrolysis of HNCO, NH_3 cracking, and urea+H_2O→H_2+CO_2+N_2 reactions, indicate the high spontaneity of the reactions to proceed in the forward direction as the decomposition temperature increases. Meanwhile, the ΔG values of WGS and methanation reactions increase with the reaction temperature which implies the lower thermodynamic feasibility to proceed,

but rather reverse the direction of the process and favour the reactant. This results in reverse of WGS and methanation of CO_2 reactions which suppress H_2 and CH_4 formations in the product gas.

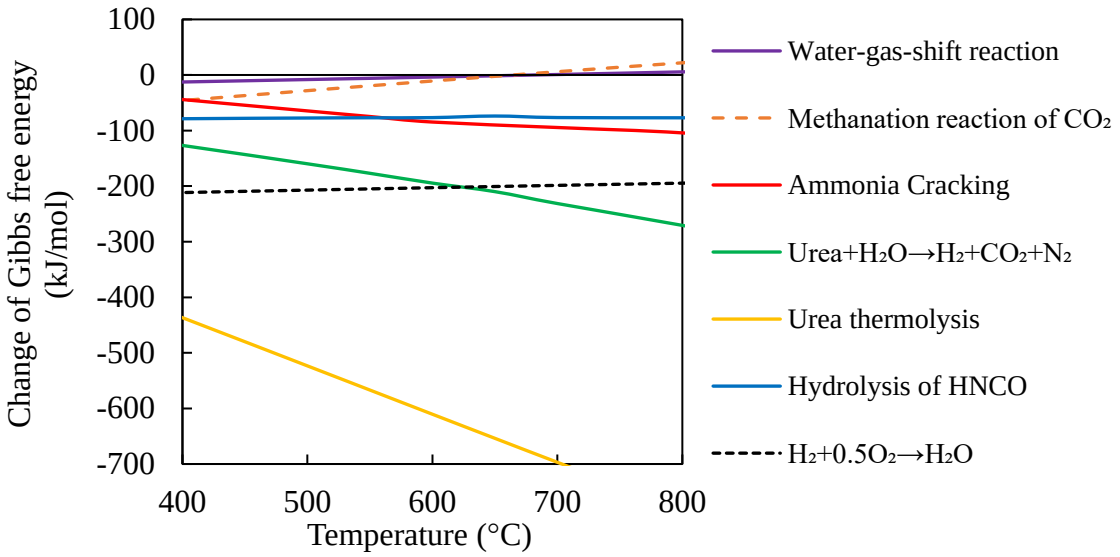

Figure 5-3: Change in Gibbs free energy of reactions involved urea decomposition in N_2+O_2

AUS32 decomposition in N_2+O_2 is experimentally validated as shown in **Figure 5-4**A and **5-4B**) which exhibits a general increasing trend of H_2, CO, CO_2, NH_3, and THCs concentrations in the product gas when AUS32 injection rate increases. At 650°C, H_2 concentration produced from the experiment is noticeably close to the equilibrium calculation predicted. H_2 concentration increases with the decomposition temperature as the result of higher rate of urea decomposition [121] as specified for further reduction ΔG of urea decomposition in **Figure 5-3**. The catalyst inlet temperature increase also enhanced H_2O desorption from the catalyst's active sites resulting in an increased H_2 production [168]. The desorption of H_2O provides more catalyst active sites for $2NH_3 \rightarrow 3H_2+N_2$ reaction by decreasing catalyst inhibition by H_2O [168], [185].

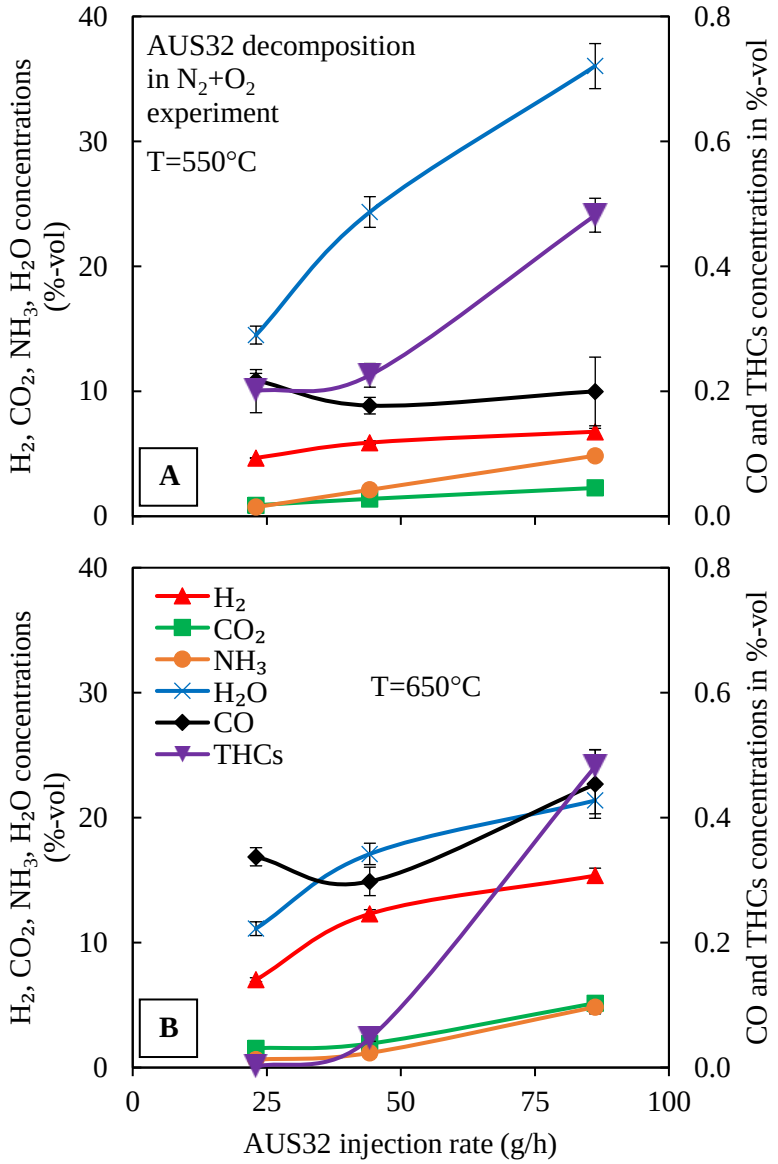

Figure 5-4: Product gas compositions from AUS32 decomposition in N_2+O_2 mixture at 550°C (A) and 650°C (B)

The divergence between equilibrium calculations and experimental results is the greater NH_3 and THCs concentrations in the product in the experiment. In general, NH_3 and THCs concentrations in the product gas increase with the higher rate of AUS32 injection as additional urea is introduced with the reactant mixture which effectively increases urea's weight hourly space velocity (WHSV) in the system. Hence, the shortened residence time [46] for NH_3 and

THCs to transform into H_2 through NH_3 cracking and SR and DR of THCs reactions. As a result, a high concentration of NH_3 and THCs are observed due to the limited capability of the fuel reforming catalyst to convert fuel. NH_3 and THCs concentrations indicate an inverse function to the O_2/urea ratio. Low rate of AUS32 injection (effectively, high O_2/urea ratio) leads to a higher degree of NH_3 and THCs oxidation [10]. The high H_2O concentration from AUS32 mixture also contributes to the low rate of urea decomposition primarily because of two phenomena: 1) adsorption H_2O onto catalyst active sites that decreases existing catalyst active sites for NH_3 cracking [168], [185], and 2) higher latent heat energy requirement for H_2O evaporation into gaseous form [32] results in a reduced amount of energy toward NH_3 decomposition process [121].

5.3.2 Process efficiency and urea conversion efficiency

Process efficiency (η) and urea conversion efficiency of AUS32 decomposition are illustrated in **Figure 5-5**. η between equilibrium calculation (denoted as 'Eqlb') and the experiment is diverged due mainly to greater H_2 concentration than predicted values. Consequently, η increases with AUS32 injection rate at 650°C regardless of declining urea conversion efficiency. However, η reduces with AUS32 injection rate at 550°C (denoted as '550°C Exp') because of decreased CO concentration as WGS is thermodynamically favourable. According to equilibrium calculations, urea conversion efficiency is near 100%, while the experimental results demonstrate up to 93% at inlet catalyst temperature of 650°C.

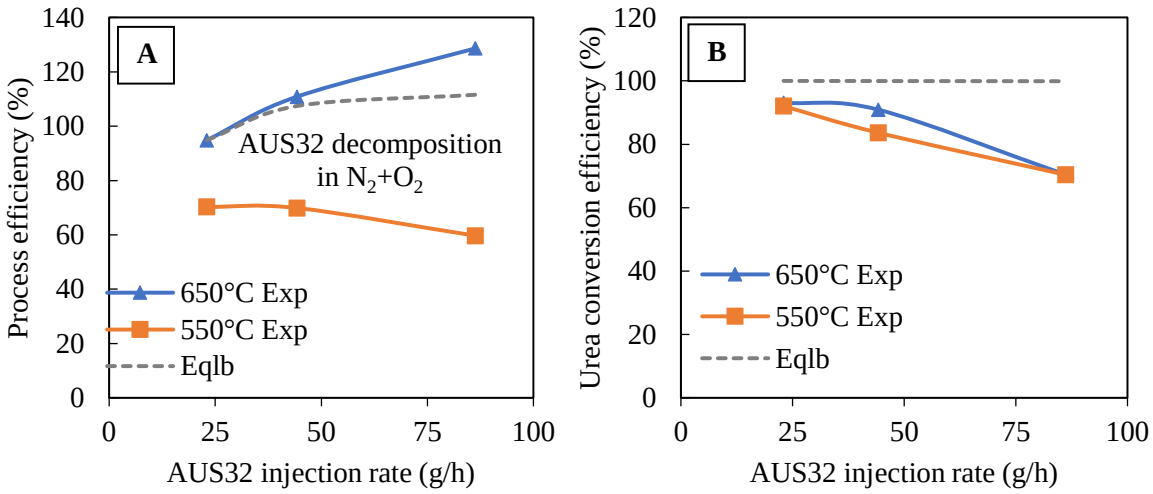

Figure 5-5: AUS32 decomposition in N_2+O_2 (A) process efficiency and (B) urea conversion efficiency.

5.4 AUS32 decomposition with GDI exhaust gas

5.4.1 Effect of AUS32 injection rate and temperature on product gas compositions

The equilibrium calculation as shown in **Figure 5-6**A illustrates product gas compositions from AUS32 decomposition in GDI exhaust gas at $\dot{m}_{AUS32}$ = 86.24 g/h as a function of catalyst inlet temperature. Generally, a comparable trend of products to that of AUS32 decomposition in N_2+O_2 can be observed with marginally higher H_2 concentration and considerably higher concentrations of C-containing products (CO, CO_2, and THCs) in the product gas. Existing CO_2 concentration in exhaust gas is accountable for the formation of CO and multiple THCs species (e.g. ethanol, methanol, methane, propylene, and ethylene) via hydrogenation of CO_2 (CO_2+H_2→C_xH_y+H_2O) at low temperature [186]–[189], and by the reverse WGS reaction at high temperature. Substantial concentrations of CO_2 and H_2O in reactant mixture of AUS32 decomposition in exhaust gas was reported to induce the overall reaction toward higher consumption of CO_2 and H_2O [32]. Hence, the reverse WGS reaction is favoured at elevated temperature (650°C) as the result of CO_2 presence in reactants. This results

in high CO concentration in the product gas compared to that of AUS32 decomposition in N_2+O_2.

Figure 5-6B illustrates a comparable trend of the effect of AUS32 input rate on the product gas compositions as is discussed previously in AUS32 decomposition in N_2+O_2 section (**Figure 5-2**). **Figure 5-6A** indicates the predicted H_2 concentration in the product is slightly higher than that of AUS32 decomposition in N_2+O_2 (**Figure 5-2**) due to available CO and THCs in the exhaust gas results in additional H_2 from WGS and SR of THCs reactions. The higher concentrations of CO and THCs is affected by the presence of CO_2 in the exhaust gas according to the equilibrium calculations. CO_2 concentration declines with the increase of AUS32 injection rate by the dilution effect in which larger fraction of urea and water are introduced in the exhaust gas. The increase rate of reverse WGS is also responsible for increased CO_2 concentration.

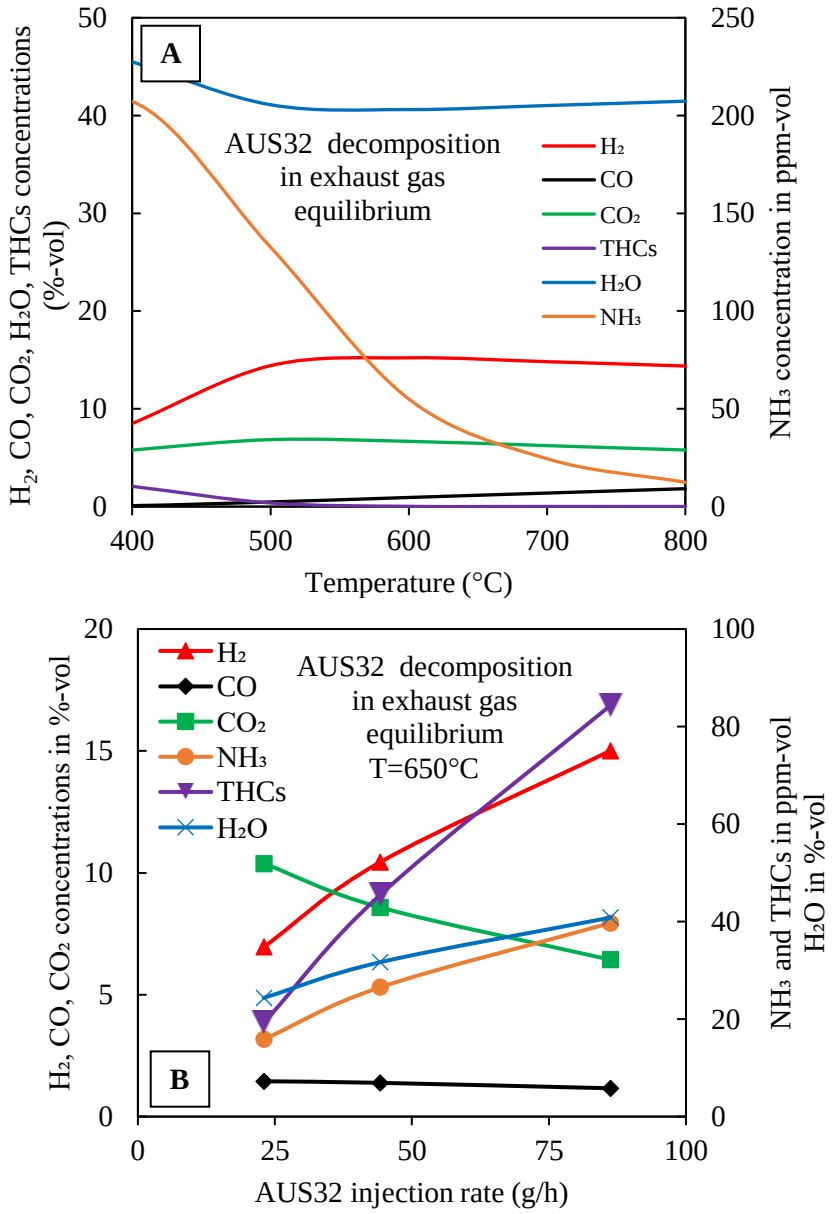

Figure 5-6: Equilibrium calculation of product gas compositions from AUS32 decomposition in exhaust gas A) effect of decomposition temperature, and B) effect of AUS32 injection rate at 650°C

The experimental validation of AUS32 decomposition in exhaust gas is illustrated in **Figure 5-8** which reveals an increasing trend for H_2, NH_3 and THCs concentrations as AUS32 injection rate increases. The experiment showed remarkably greater H_2 concentration and

higher NH_3 and THCs concentrations in the product gas compared to the values predicted by equilibrium calculations. The divergence of the results between equilibrium calculation and the experiments is due to high H_2O concentration in the reactant mixture. In the experiments, the molecular absorption of H_2O affects the catalyst activity through restriction of the absorption of NH_3 onto the catalyst's active sites [169], [190]. Intensified with the slow rate of NH_3 dehydrogenation process ($2NH_3 \rightarrow 3H_2+N_2$ reaction) [81] and limited residence time (gas contact time) with the catalyst active sites, these results in high concentration of unconverted NH_3 in the product gas. Based on the nature of the equilibrium calculations, all gas species have indefinite residence time to attain their equilibrium state, and there is no heat loss in the system. CO concentration from the AUS32 decomposition in the exhaust gas experiment is marginally lower than the equilibrium prediction because of the lower rate of reverse WGS reaction. This is due to the presence of the Ru catalyst that has high selectivity toward the forward direction of WGS [191]. Subsequently, higher CO_2 concentrations can be observed as a smaller number of moles of CO_2 is consumed in the experimental results.

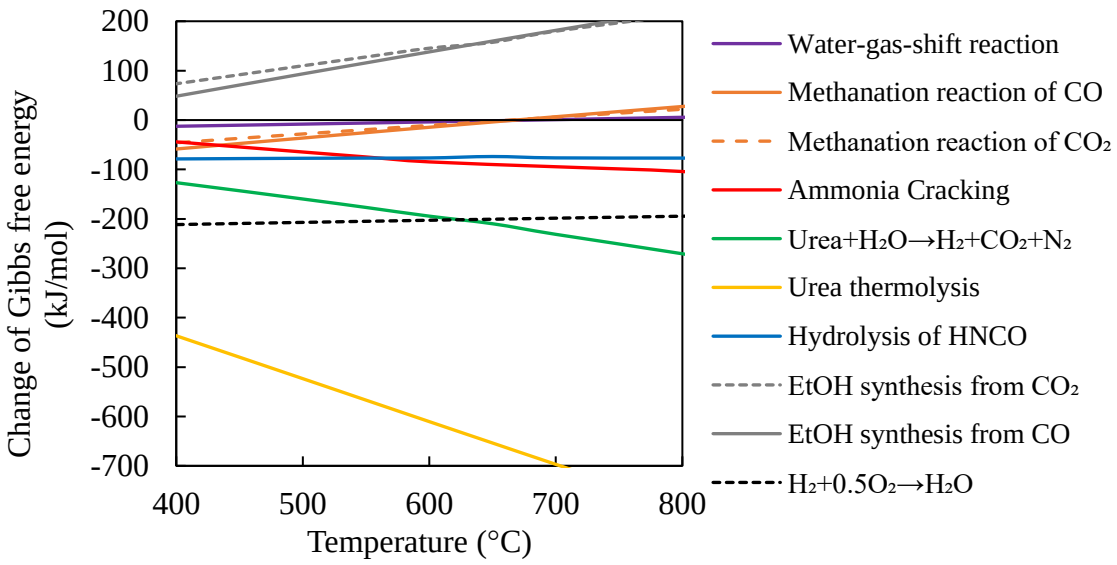

Figure 5-7: Change in Gibbs free energy of reactions involved urea decomposition in GDI exhaust gas

When comparing the results between AUS32 decomposition in N_2+O_2 experiment and the AUS32 decomposition in exhaust gas, the experimental results indicate remarkably lower H_2 concentration in the product output for any given AUS32 injection rate and catalyst inlet temperature. The H_2 concentration difference between AUS32 decomposition in N_2+O_2 and AUS32 decomposition in exhaust gas is affected by the presence of gas species in the GDI exhaust gas (e.g. CO, CO_2, THCs, H_2, NO and O_2). H_2 production is influenced by methanations, partial oxidation (POX), and reverse WGS reactions. According to the ΔG value of reactions involved urea decomposition in **Figure 5-3**, it specifies that H_2 can be utilised by methanation and ethanol synthesis reactions at low temperature. Meanwhile, reverse WGS reaction is responsible for H_2 consumption at the higher temperature. This is supported by the CO concentrations in the product from AUS32 decomposition in N_2+O_2 is considerably lower than that of AUS32 decomposition in the exhaust gas as shown in **Figure 5-4**. The lower CO concentration in AUS32 decomposition in N_2+O_2 is caused by the absence of GDI exhaust gas species (mainly, CO_2) that produced CO.

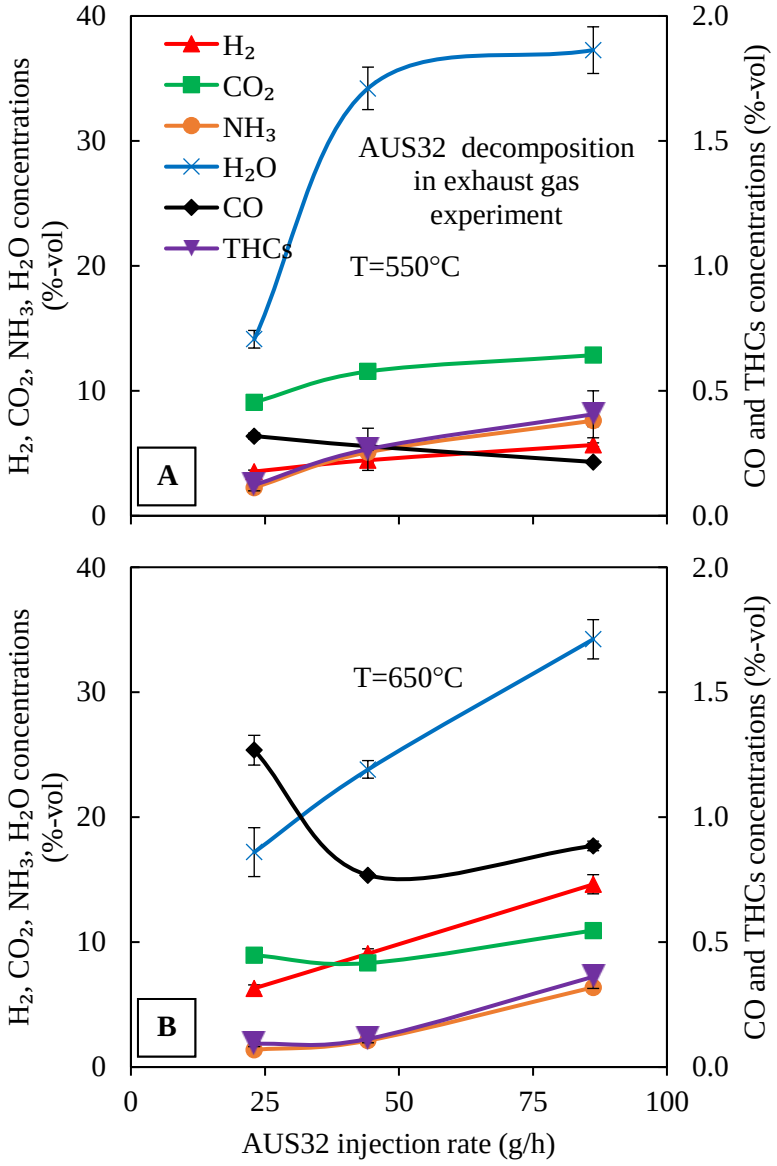

Figure 5-8: Product gas compositions from AUS32 decomposition in exhaust gas experiment at 550°C (A) and 650°C (B)

CO concentration in the product gas in this experimental study (up to 1.3%-vol) is noticeably low in comparison to other previous fuel reforming studies from hydrocarbon fuels (>10%-vol) [7], [10], [42]. This is due to the significantly lower carbon atoms in the reactant when using urea solution as H_2 carrier (only 1 carbon atom per mole of urea). The H_2/CO molar

ratio of product gas in this study is between 4 to 41 while other H_2 production studies [16], [42], [66] reported H_2/CO ratio values of between 0.8 to 6. The product in this study is considered a 'cleaner product' in the viewpoint of carbon footprint because combustion of this product gas will emit lower CO_2 emission to the atmosphere.

A higher concentration of unconverted NH_3 is found in AUS32 decomposition in exhaust gas than that of AUS32 decomposition in N_2+O_2 at any AUS32 injection rate as the result of lower selectivity of NH_3 cracking toward H_2 formation. The additional H_2O concentration in GDI exhaust gas increases H_2O concentration in the reactant mixture compared to that of AUS32 decomposition in N_2+O_2. This contributes to a higher degree of H_2O inhibition that reduces the catalyst activity as the result of H_2O molecular absorption onto catalysts' active sites and competing with NH_3 adsorption [169]. The H_2O inhibition effect combines with the rate-limiting step of dinitrogen desorption of $2NH_3 \rightarrow 3H_2+N_2$ reaction, this results in high NH_3 concentration and decreases urea decomposition efficiency as shown in **Figure 5-9**. It is worth noting that NO in the GDI exhaust gas has tendency to proceed toward $2NO+2CO \rightarrow 2CO_2+N_2$ reactions according to the reaction's ΔG value of less than 0. Moreover, the Ru catalyst has high selectivity toward reducing NO rather than NH_3 formation pathway [81].

5.4.2 Process efficiency and urea conversion efficiency

Figure 5-9A indicates the process efficiency of greater than 100% for the AUS32 exhaust gas decomposition experiment at 650°C which is relatively close to the equilibrium calculation value. Whereas the process efficiency at 550°C is considerably lower than that of the decomposition experiment at 650°C because of lower forward rate of $2NH_3 \rightarrow 3H_2+N_2$ reaction and the lower tendency of the reaction to proceed toward H_2 production as the ΔG value illustrated in **Figure 5-3**. Urea conversion efficiency shown in **Figure 5-9B** increases with the catalyst inlet temperature for any AUS32 injection rates because of enhanced urea thermolysis reaction. When compared to the AUS32 decomposition in the N_2+O_2 experiment, the AUS32 decomposition in the exhaust gas experiment shows lower urea conversion efficiency due to the low rate of NH_3 cracking reaction. Based on the process efficiency and urea conversion efficiency, it is practical to operate AUS32 decomposition in exhaust gas from 650°C onward where high decomposition efficiency and high urea conversion can be realised. Another benefit is to avoid poisoning and carbon formation that negatively impacts catalyst's activity.

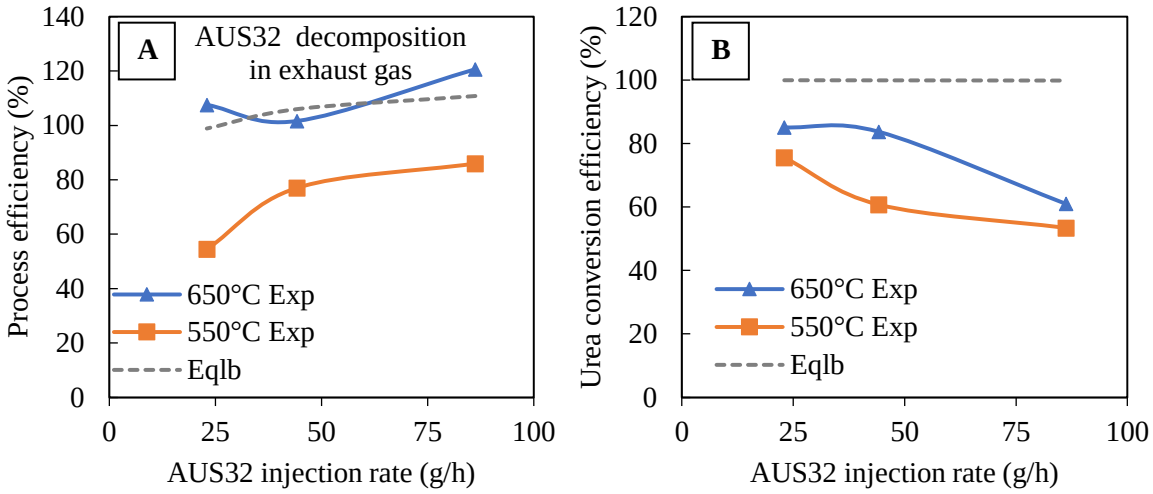

Figure 5-9: Process efficiency (A) and urea conversion efficiency (B) of AUS32 decomposition in exhaust gas

5.5 Tailpipe CO_2 emission reduction and waste heat energy recovery

Tailpipe CO_2 reduction and exhaust gas waste heat energy recovery are calculated based on the exhaust gas exergy of the actual engine conditions described in **Table 5-2**. The exhaust gas exergy of designated engine conditions is in the range between 4.0 kW to 17.9 kW which is between 11.5% to 16.2% of fuel input energy of GDI engine as shown in **Figure 5-10**. Tailpipe CO_2 reduction and heat energy recovery of the chosen engine conditions are determined using product gas compositions from experimental AUS32 decomposition in N_2+O_2 and AUS32 decomposition in exhaust gas at 650°C, and AUS32 injection rate of 86.24 g/h. This condition is chosen based on high process efficiency, high H_2/CO ratio, and because it is achievable with the selected engine conditions (in Table 5-2).

As illustrated in **Figure 5-11**, CO_2 reduction and heat energy recovery depict a proportional relation with the engine output power because more waste heat energy is available to produce H_2 on-board to replace gasoline. In a full-scale application, tailpipe CO_2 reductions are expected up to 17.8% and 16.3% for using H_2 from AUS32 decomposition in N_2+O_2 and AUS32 decomposition in exhaust gas, respectively. Exhaust gas waste heat energy recovery is

up to 4.8 kW and 3.5 kW (4.4% and 3.1% of input energy) for AUS32 decomposition in N_2+O_2 and AUS32 decomposition in exhaust gas, respectively, as shown in **Figure 5-11**. H_2 derived from AUS32 decomposition in N_2+O_2 demonstrates better CO_2 reduction and energy recovery because of the high H_2/CO ratio of the product gas that results in lower CO_2 emitted from the combustion. Exhaust gas energy recovery has a direct correlation with the process efficiency. This study evaluates potential CO_2 reduction by utilising H_2 derived from AUS32 decomposition in the GDI engine, assuming that the engine's thermal efficiency is unchanged. However, in the practical application, using H_2 in the engine will improve thermal efficiency [6], [44]. Therefore, better fuel economy and further CO_2 reduction can be expected.

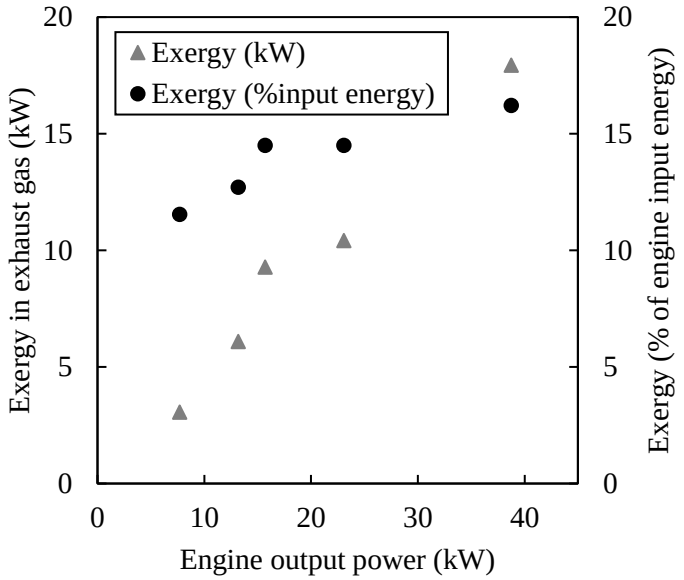

Figure 5-10: Estimated GDI exhaust gas exergy and % exergy of engine brake output power

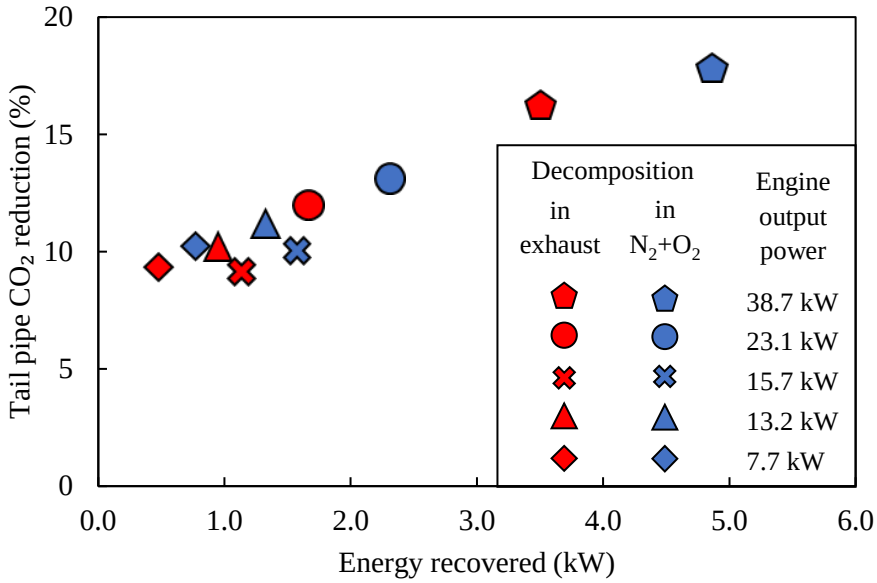

Figure 5-11: Potential CO_2 reduction and energy recovered if using product gas as REGR

5.6 Summary

Aqueous urea solution (AUS32) has a prospect as H_2 carrier for on-board hydrogen production owing to its properties such as ease of handling, end-user availability, and low flammability. This chapter studied the H_2 production from catalytic decomposition AUS32 via thermochemical exhaust gas waste heat energy recovery in two different scenarios; using only exhaust gas heat for oxidative decomposition process (using N_2+O_2 mixture) and using both heat and gas species in exhaust gas to generate H_2 from urea solution. AUS32 decomposition was studied through thermodynamic analysis and experimental approaches.

AUS32 decomposition in the N_2+O_2 mixture experiment demonstrated a comparable trend for H_2 yield in the product gas compared to the equilibrium prediction. Urea conversion efficiency was largely dependent on decomposition temperature and O_2/urea ratio. High water content in urea solution resulted in overall high H_2O concentration in the reactants (up to 40%-vol) (calculated) contributed to lowered rate of NH_3 cracking and resulted in high NH_3 concentrations in the product gas. Maximum H_2 yield of 14.6%-vol is achieved.

AUS32 decomposition in the GDI exhaust gas experiment revealed a similar outcome for H_2 yield in the product gas in comparison to that of AUS32 decomposition in the N_2+O_2 experiment. Substantial THCs concentration could be detected as a by-product of urea decomposition through hydrogenation of CO_2 reaction. Increasing O_2/urea ratio demonstrated the suppression of THCs formation at the cost of lowering process efficiency.

The calculation showed that using H_2 produced from AUS32 decomposition could potentially reduce tailpipe CO_2 emission up to 17.8% and recover waste heat energy approximately 4.4% at typical operating conditions of multiple cylinders gasoline engines in passenger cars.

Chapter 6 Hydrogen production from carbon-neutral hydrogen carriers

6.1 Introduction

The increased share of renewable energy harvested from wind and solar leads to excess renewable energy [21], [192] which can be used to produce synthetic fuel, namely, electrofuel or e-fuel. It can be considered as a better way to store excess electricity than other energy storage forms e.g. chemical battery, pump-hydro-power, and H_2. Electrofuel is also carbon neutral because it is produced from CO_2 which can source from direct air capture [193]. Therefore, the utilisation of electrofuel does not contribute additional CO_2 into the atmosphere. Furthermore, using electrofuel as H_2 carrier for on-board H_2 production can benefit from its carbon neutral properties. This chapter presents the investigation on the H_2 production from the carbon-neutral energy carriers (Urea, Ethanol, and Methanol) through catalytic thermochemical energy recovery of a modern GDI engine exhaust gas. The blends between AUS32-ethanol (denoted as AUS32+EtOH) and AUS32-methanol (denoted as AUS32+MeOH) are used as H_2 carriers. Thermodynamic analysis and experimental investigation are carried out to study the influence of gas species in exhaust gas that affects the H_2 production. The reforming process efficiency and reforming product compositions are studied. Analysis on carbon footprint and exhaust gas waste heat energy recovery when H_2 derived from the reforming process is used as fuel to replace gasoline fuel.

6.2 Experimental conditions

The study of H_2 production from AUS32-ethanol and AUS32-methanol blends reforming with exhaust gas from a GDI engine are carried out by both thermodynamic analysis and experimental approach. The reactant injection rate was varied to achieve an equivalence O_2/NH_3 ratio between 0.04 to 0.15 as shown in **Table 6-1**. Reforming reactant blends have H_2O/ethanol or H_2O/methanol molar ratio of 5. This H_2O/fuel ratio is selected based on 'carbon formation free-zone' reported in literature [9], [10], [105].

Table 6-1 Reactant injection rates for the H_2 production study

Calculated O_2/NH_3 ratio	**O_2/EtOH or O_2/MeOH ratio**	**Reactant flow rate (g/h)**	
		AUS32+EtOH	**AUS32+MeOH**
0.040	0.058	122.5	118.5
0.078	0.112	66.6	60.8
0.150	0.216	38.4	31.6

6.3 Reforming process and fuel conversion efficiencies

Equilibrium calculations expect η_{ref} (as shown in **Figure 6-1**) of AUS32+EtOH and AUS32+MeOH blends exhaust gas reforming to be greater than 100% specifying the enthalpy gain as the result of H_2 production at both reforming temperature (550°C and 650°C). The η_{ref} from equilibrium calculation reveals near complete conversion efficiency for urea, ethanol, and methanol (>99%) as shown in **Figure 6-2**. The experimental results in **Figure 6-1** demonstrate above 100% reforming process efficiency can be reached at 650°C for both AUS32+EtOH and AUS32+MeOH blends which determines that exhaust gas waste heat energy recovery is possible. At 550°C, AUS32+MeOH reforming indicates lower η_{ref} compared to reforming at 650°C for any reactant injection rate as the result of enhanced H_2 production with increased temperature. On the other hand, AUS32+EtOH reforming shows noticeable lower η_{ref} at low

and medium reactant injection rates because of the higher degree of oxidation (effectively higher O_2/EtOH ratio) that adversely influences H_2 yield. Overall, η_{ref} of both AUS32+EtOH and AUS32+MeOH reforming increase with the higher reactant injection rate due to the more hydrogen atom introduced and resulting in higher H_2 concentration in the reformate. Increasing the reactant injection rate effectively decreases O_2/fuel ratio which causes in less portion of fuel utilised by the oxidation process. Reforming temperature and the rate of fuel injection significantly affect the H_2 production of AUS32+EtOH blend which indicates the difference of η_{ref} values. The noticeable greater η_{ref} of AUS32+MeOH reforming at 550°C than that of AUS32+EtOH reforming is a result of the advantage of lower temperature at steam reforming of methanol (≈260°C) [40] compared to ethanol steam reforming (>323°C) [142].

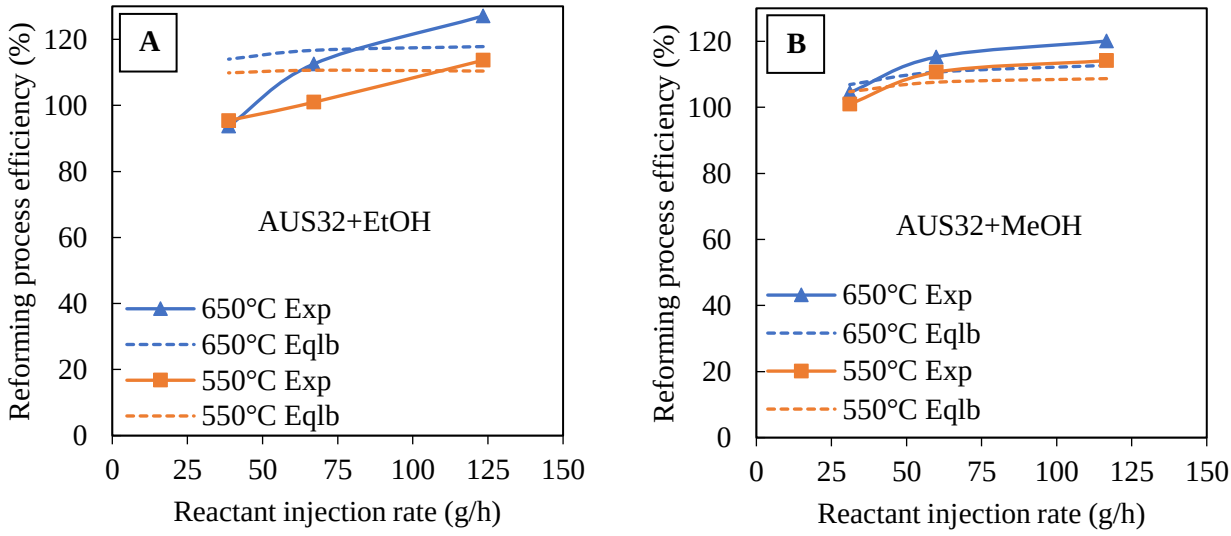

Figure 6-1: Reforming process efficiencies of AUS32+EtOH (A) and AUS32+MeOH (B) exhaust gas reforming

Figure 6-2 illustrates the experimental results of reactant conversion efficiency of AUS32+MeOH blend is noticeably higher than that of AUS32+EtOH blend at 550°C. This is due to the absence of C-C bond in methanol that requires less heat energy for the steam reforming process. Meanwhile, the relatively intensive endothermic nature of ethanol steam

reforming, and ethanol's high latent heat of vaporisation result in a large amount of heat energy required. Especially, at a high reactant injection rate where more mass flow of reactant enters the catalyst. The high S/C ratio in reactant blend was reported to significantly increase heat energy cost for reforming process [10] due to high heat capacity of H_2O in AUS32 [32]. Moreover, the limited residence time of the reactant with the catalyst surface means insufficient time for reaction to fully reach equilibrium state. Hence, a negative impact on conversion efficiency [13], [45]. This results in the lowered ethanol and urea conversion efficiencies at high reactant injection rate and 550°C compared to AUS32+MeOH reforming.

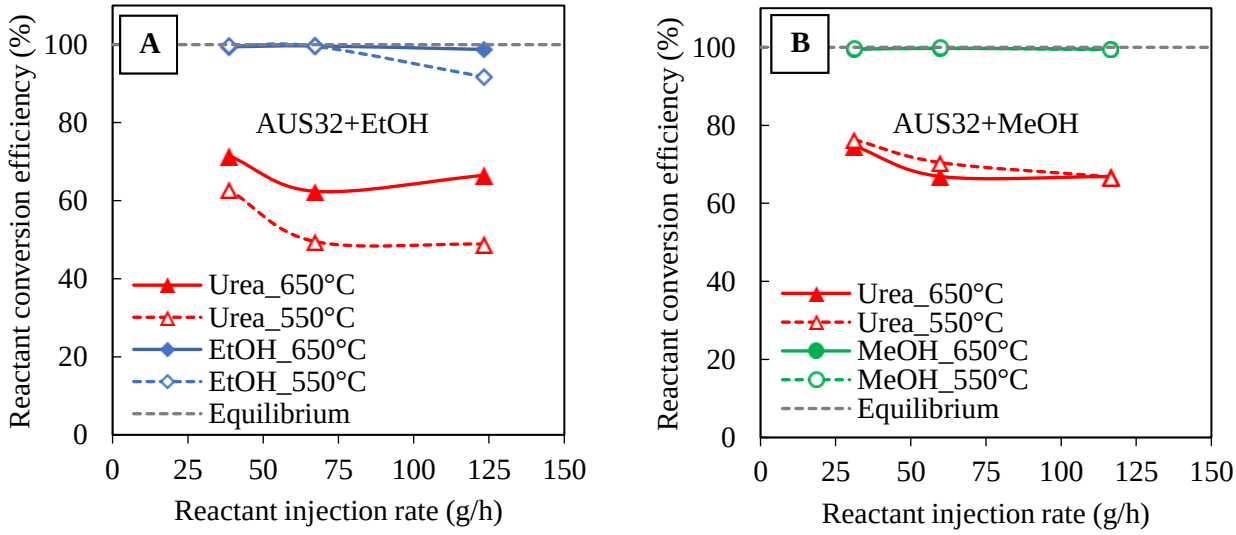

Figure 6-2: Reactant conversion efficiencies of AUS32+EtOH (A) and AUS32+MeOH (B) exhaust gas reforming

6.4 Thermodynamics analysis of hydrogen production

The change in Gibbs free energy of main reactions involved in the reforming of AUS32+EtOH and AUS32+MeOH blends with respect to reforming temperature at atmospheric pressure is illustrated in **Figure 6-3**. At low temperature, ΔG values of urea decomposition reactions (e.g., hydrolysis of HNCO, urea thermolysis, and

urea+$H_2O \rightarrow H_2+CO_2+N_2$ reactions) show the high spontaneity of reaction to proceed in the forward direction in compared to other reactions for both AUS32+EtOH and AUS32+MeOH reformings. SR of methanol, SR of ethanol, DR of ethanol, and WGS reactions contribute to the increasing of H_2 and CO concentrations in the reformate at low reforming temperature regions. At higher reforming temperature, the increasingly negative ΔG values of SR of ethanol and methanol, DR of ethanol, and urea decomposition reactions indicating these reactions are thermodynamically favourable which H_2 and CO productions are enhanced. However, WGS and methanations reactions indicate the decline of ΔG values as the reforming temperature increases. This is because the reactions are less thermodynamically feasible, and the reaction favours the reactant. A slight decline of H_2 production can be observed. CH_4 formation is suppressed, and CO and CO_2 concentrations in the reformate are increased as the result.

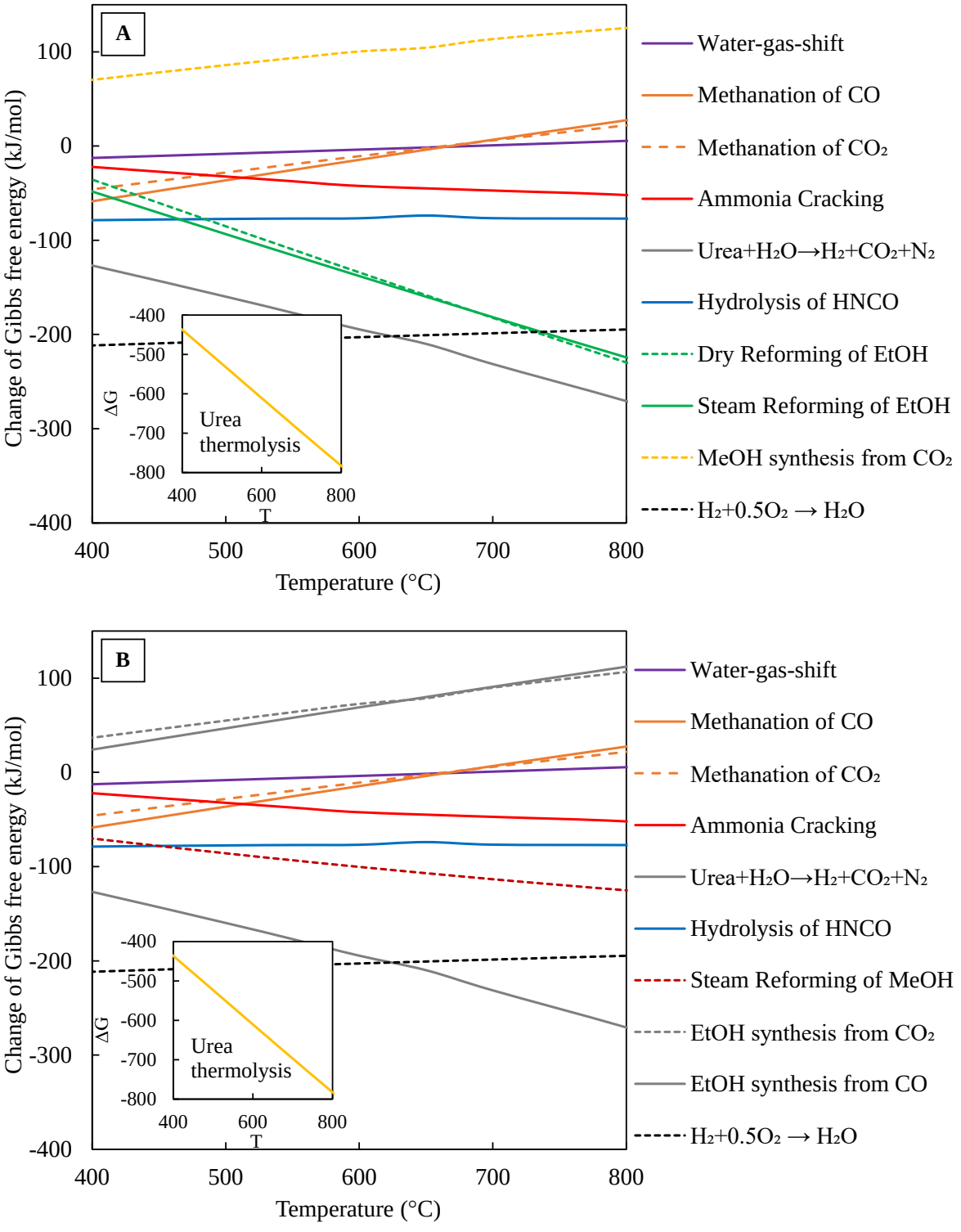

Figure 6-3: Change in Gibbs free energy of main reforming reactions as a function of reforming temperature of AUS32+EtOH (A) and AUS32+MeOH (B) exhaust gas reforming

6.5 Equilibrium prediction of reformate gas compositions

6.5.1 Effect of reforming temperature on reformate gas compositions

The equilibrium calculation of the reformate gas compositions from H_2 production from AUS32+EtOH (**Figure 6-4A**) and AUS32+MeOH (**Figure 6-4B**) at equivalence O_2/ethanol and O_2/methanol of 0.058 are illustrated in **Figure 6-4**. Reformate gas compositions from AUS32+EtOH and AUS32+MeOH exhaust gas reforming have a similar trend as a function of the reforming temperature. Though, equilibrium calculation of AUS32+MeOH reforming specifies a perceptible lower concentration of H_2, CO, and THCs because of the lower number of C-H atoms in methanol compared to that of ethanol.

At low reforming temperatures, CH_4 is the primary carbon-containing product in the reformate gas because the methanation reaction is thermodynamically viable as indicated by the negative ΔG value shown in **Figure 6-3**. The competition between methanation reaction and WGS reaction for CO [194], [195] through hydrogenation [196] consumes and suppresses H_2 concentration in the reformate gas. At a low temperature, WGS reaction is kinetically controlled [194], hence the further reduction of CO concentration through conversion into H_2 and CO_2. A substantial concentration of NH_3 in the reformate is expected because of the lower forward rate of the NH_3 cracking reaction at low temperature [29].

As the reaction temperature increases, the gradual decrease of ΔG values of SR (of both ethanol and methanol) and DR (of ethanol), $Urea+H_2O \rightarrow H_2+CO_2+N_2$, and NH_3 cracking reactions are as shown in **Figure 6-3**. This indicates that these reaction pathways are more thermodynamically favourable. However, the increasing ΔG values of methanation and WGS reactions (and becomes a positive value around 675°C) indicates the tendency of the reaction to proceed in the reverse direction. Consequently, H_2 and CO concentrations increase and CH_4

concentration decrease can be observed, while THCs and NH_3 concentrations decrease with the increase of reforming temperature.

At high reforming temperatures, high reaction rate is favoured including SR of ethanol and methanol, DR, urea decomposition, NH_3 cracking reactions which contribute to the H_2 production. H_2 production reaches the peak at near 650°C and 600°C for AUS32+EtOH and AUS32+MeOH reforming, respectively. The reverse of WGS and methanation reactions become thermodynamically favourable according to the ascending ΔG value as shown in **Figure 6-3**, CO concentration increases while CO_2 concentration decreases with the reforming temperature. H_2/CO molar ratios of reformate from AUS32+MeOH reforming is greater than that of AUS32+EtOH reforming owing to the higher H/C ratio in methanol ($H/C_{MeOH} = 4$) compared to ethanol ($H/C_{EtOH} = 3$) [40].

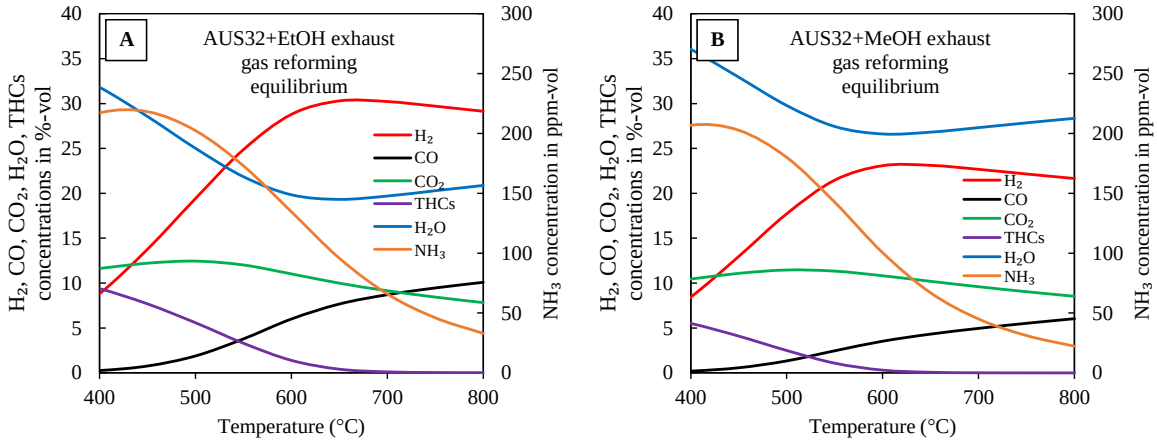

Figure 6-4: Reformate gas compositions, equilibrium calculations as a function of reforming temperature for AUS32+EtOH (A) and AUS32+MeOH (B) at a reactant injection rate of 122.5 g/h and 118.5 g/h, respectively.

6.5.2 Effect of reactant injection rate on reformate gas compositions

The effect of reactant injection rate on the reformate gas compositions at 550°C and 650°C is illustrated in **Figure 6-5**. Generally, the increased concentrations of all gas species in the reformate (e.g. H_2, CO, NH_3, and THCs,) can be observed in proportion to the reactant injection rate. This is the result of increasing the input hydrogen and carbon atoms in the reactant mixture for both AUS32+EtOH and AUS32+MeOH reformings. The elevated reactant injection rate effectively decreases the O_2/fuel ratio resulting in milder exothermic reactions (e.g. NH_3+O_2, H_2+O_2, and THCs+O_2 reactions). Meanwhile, it increases the degree of endothermic reactions (e.g. Urea+$H_2O \rightarrow H_2+CO_2+N_2$, SR of ethanol & methanol, and DR of ethanol) that enhances H_2 production. On the contrary, CO_2 concentration declines with the increase of reactant injection rate because of the dilution effect from adding a significant number of mole reactants in the reactant-exhaust mixture. At the chosen reforming temperatures, the equilibrium calculation reveals that the methanation reaction is substantially suppressed resulting in trace amounts of CH_4 contained in the reformate gas product.

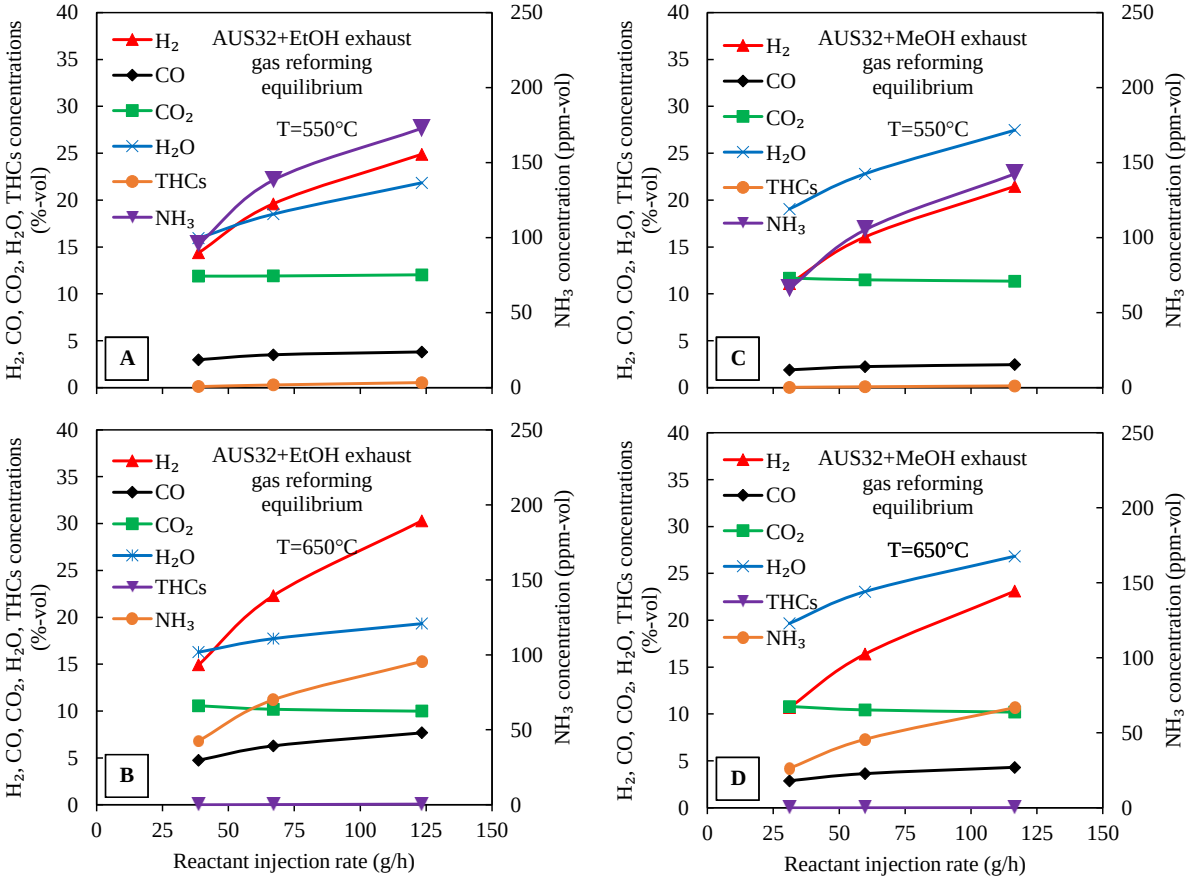

Figure 6-5: Reformate gas compositions, equilibrium calculations as a function of reactant injection rate of AUS32+EtOH and AUS32+MeOH reformings at 550°C and 650°C.

6.6 Experimental analysis of reformate gas compositions

Experimental validation of H_2 production from AUS32+EtOH (**Figure 6-6A** and **6-6B**) and AUS32+MeOH (**Figure 6-6C** and **6-6D**) via exhaust gas reforming demonstrate the effect of reactant injection rate on gas compositions in the reformate gas at the catalyst inlet temperature of 550°C and 650°C. H_2, CO, NH_3, and CH_4 concentrations in the reformate increase with the reactant injection rate as predicted by the equilibrium calculations. CO_2 concentration decreases when reactant injection rate increases because of the dilution effect caused by injecting large amounts of reactant in the exhaust gas. The formation of CH_4 and

other hydrocarbon by-products in the reformate through hydrogenation of CO_2 [196], [197] are accountable for the reduction of the CO_2 in the reformate.

The higher reforming temperature substantially affects H_2 concentration in the reformate of AUS32+EtOH reforming than that of AUS32+MeOH reforming. This phenomenon complies with the equilibrium prediction in **Figure 6-4** as AUS32+EtOH reforming indicates peak H_2 production (~30%-vol) at near 650°C. Meanwhile, AUS32+MeOH reforming has H_2 production plateau (~23%-vol) at a lower temperature because of methanol low reforming temperature properties [40].

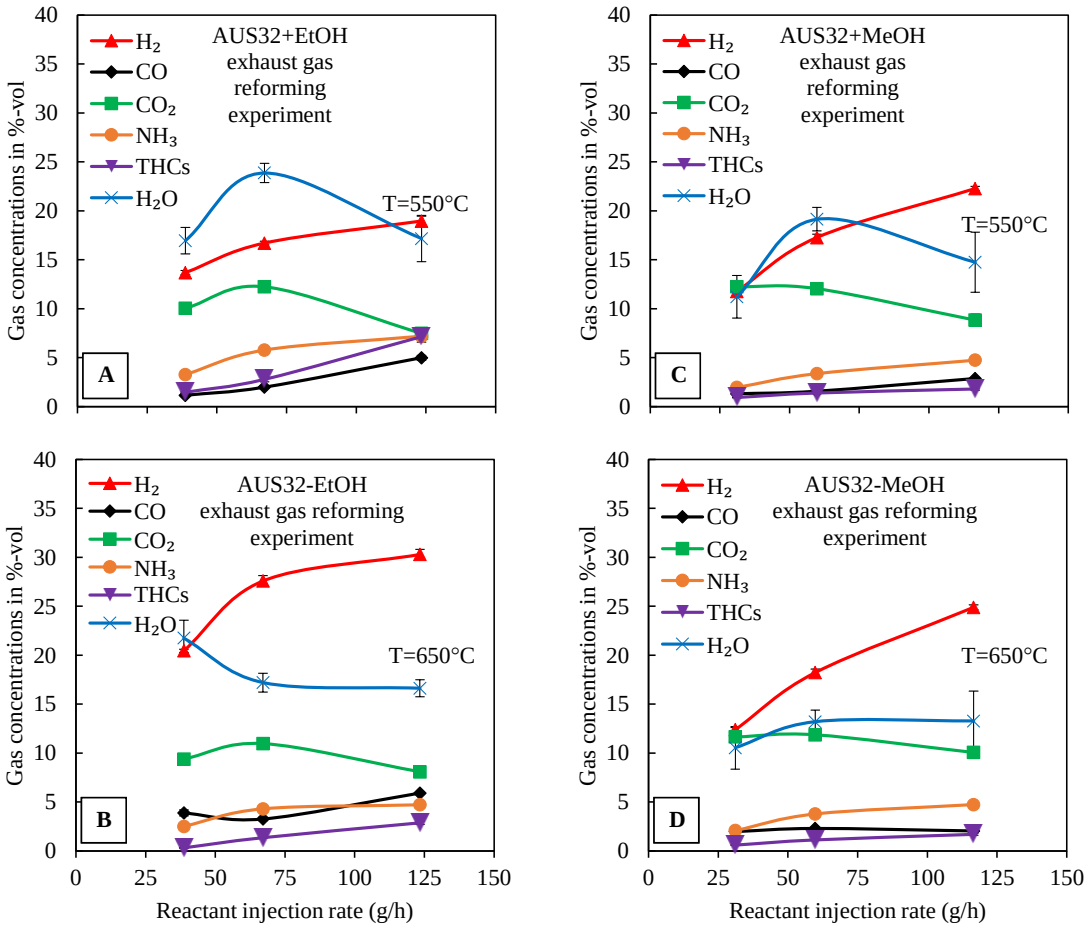

Figure 6-6: Experimental results of reformate gas compositions from AUS32+EtOH and AUS32+MeOH exhaust gas reformings as a function of reforming temperature and reactant injection rate

CO concentration in the reformate from AUS32+EtOH and AUS32+MeOH reforming are remarkably lower than the equilibrium predictions as the result of the lower rate of reverse WGS reaction. The high selectivity of the Ru catalyst toward the forward direction of the WGS reaction is responsible for low CO yield [191]. A significantly lower CO concentration in the reformate from AUS32+MeOH reforming in comparison to that of AUS32+EtOH is because of lower C/H ratio in methanol [40], [198]. Consequently, the reformate from AUS32+MeOH reforming indicates a higher H_2/CO ratio than that of AUS32+EtOH reforming.

A substantial concentration of NH_3 is found in the reformate from both AUS32+EtOH and AUS32+MeOH reforming as the result of the limited contact time of reactant gas species to adsorb onto the catalyst surface. The high H_2O concentration in the reactant mixture plays an important role in the catalyst deactivation. In the experiments, the catalyst activity is impacted by the H_2O molecular absorption that restricts the absorption of NH_3 onto the catalyst's active sites [38], [39]. Low urea conversion efficiency (as shown in **Figure 6-2**) can be observed due to the slow rate of NH_3 dehydrogenation process (NH_3 cracking reaction) [30] at reforming temperature of 550°C. In contrary, equilibrium calculations exclude heat loss in the reforming system residence time of gas species, resulting in the near complete of urea conversion (low NH_3 concentration in the reformate predicted).

The considerable concentration of THCs is detected in the reformate from both reactant blends (AUS32+EtOH and AUS32+MeOH) as the result of CH_4 and other HCs formations through methanation and hydrogenation of CO_2 [187], [199]. Ruthenium catalyst is reported for high selectivity toward CO_2 hydrogenation to CH_4 formation [196] at low temperature. The ruthenium catalyst is also highly active in methanol [200] and ethanol [187] formations through hydrogenation of CO_2 which can be detected in the reformate gas product as shown in **Figure 6-7**. Especially, for H_2 production from AUS32+EtOH where significant THCs concentration

can be observed at 550°C. CH_4 is the main hydrocarbon product identified in the reformate gas and is accounted for over 90% and 85% of total hydrocarbons concentration at the temperature of 550°C and 650°C, respectively. Traces of other hydrocarbons, for instance; propylene, ethylene, and formic acid, are detected as shown in **Figure 6-7** indicating by-products of reforming reactions. Ethylene is a precursor of coke formation [38], [201] and its presence indicates the likeliness of catalyst deactivation for long/sustain operation.

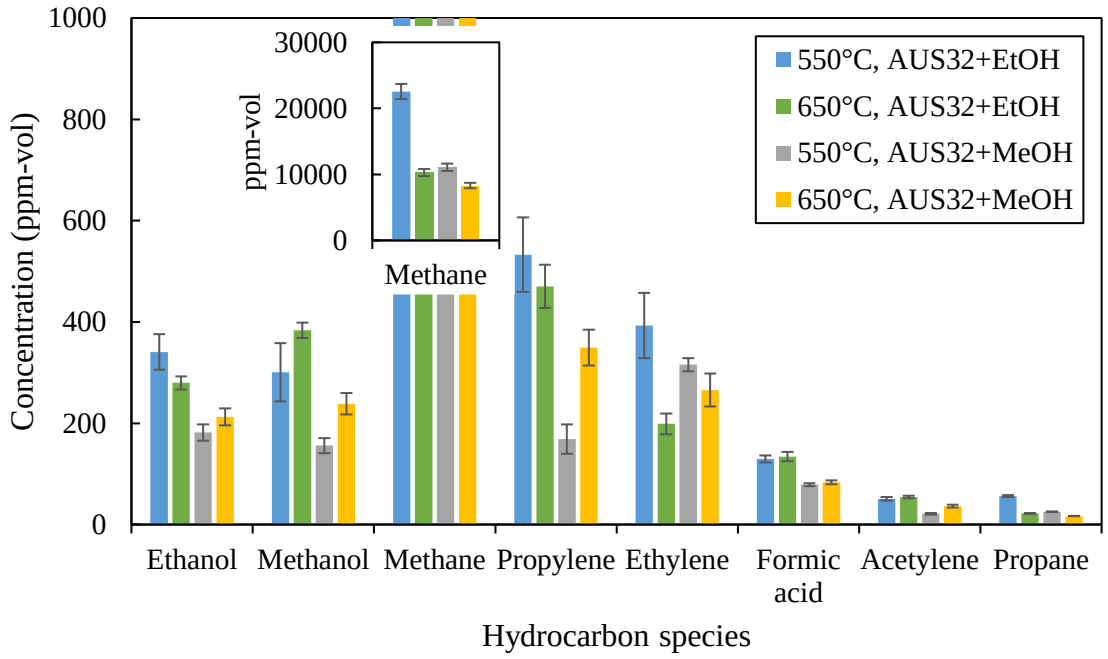

Figure 6-7: Hydrocarbon species in the reformate gas of AUS32+EtOH and AUS32+MeOH exhaust gas reforming at a reactant injection rate of 66.6 g/h and 60.8 g/h, respectively.

6.7 Impact on tailpipe CO_2 reduction, energy recovery, and well-to-wheel analysis

Using e-fuel in the ICE as primary fuel without a thermochemical energy recovery system (fuel reforming system) will result in a carbon neutral situation. As a particular amount of CO_2 is utilised as feedstock for e-fuel production, then the same quantity of CO_2 is emitted from the ICE combustion back to the atmosphere [202]. Conversely, using e-fuel in the ICE alongside with a thermochemical energy recovery system can improve the overall energy

efficiency because the presence of H_2 within the reformate helps improve ICE's brake thermal efficiency (η_{th}) [6]. This means less fuel consumption is possible while producing the same engine output power. Consequently, lower CO_2 emission into the atmosphere can be realised and less contribution to the greenhouse effect.

Figure 6-8 demonstrates the impact of using H_2 derived from AUS32+EtOH and AUS32+MeOH exhaust gas reforming on reduction of tailpipe CO_2 and waste heat energy recovery of a GDI engine at different EGR rates and reforming temperatures. The assumption is made that the exhaust gas of the EGR system is used in the reforming process to produce H_2-containing reformate which is supplied through the GDI engine intake manifold. As reforming reactants (AUS32+EtOH and AUS32+MeOH) are carbon-neutral, hence carbon product (CO_2) from the reforming process is excluded from the calculation. This results in significant tail-pipe CO_2 reduction. Greenhouse gas reduction and energy recovery are calculated using reformate gas compositions obtained at 550°C and 650°C and at reactant injection rate of 122.6 g/h and 118.5 g/h for AUS32+EtOH and AUS32+MeOH reforming, respectively. Overall, CO_2 reduction increases linearly with the EGR rate because a greater number of moles H_2 is introduced to replace gasoline. While energy recovery increases with the EGR rates because the greater quantity of reformate is generated which further extracts more heat energy from the GDI exhaust gas stream [13], [16]. At the reforming temperature of 650°C, GDI engine operates with H_2 derived from AUS32+EtOH reforming indicates superior CO_2 reduction than that of AUS32+MeOH because of higher H_2 yield in the reformate. The larger heat energy recovery is the result of the higher enthalpy of reforming reaction of ethanol compared to methanol. Therefore, a larger magnitude of waste heat energy can be extracted from GDI exhaust gas stream. At the reforming temperature of 550°C, utilising H_2 produced from AUS32+EtOH and AUS32+MeOH reformings demonstrate lower CO_2 reductions. This is because of the lower H_2

concentration and higher CO and THCs concentration in the reformate (effectively lower H_2/CO ratio in the reformate). The full-scale application of the proposed system with improvement in reformer's heat transfer design (which could improve energy recovery coefficient). Including η_{th} enhanced by using H_2 reformate, the better CO_2 reduction and engine-out emission improvement are expected [13].

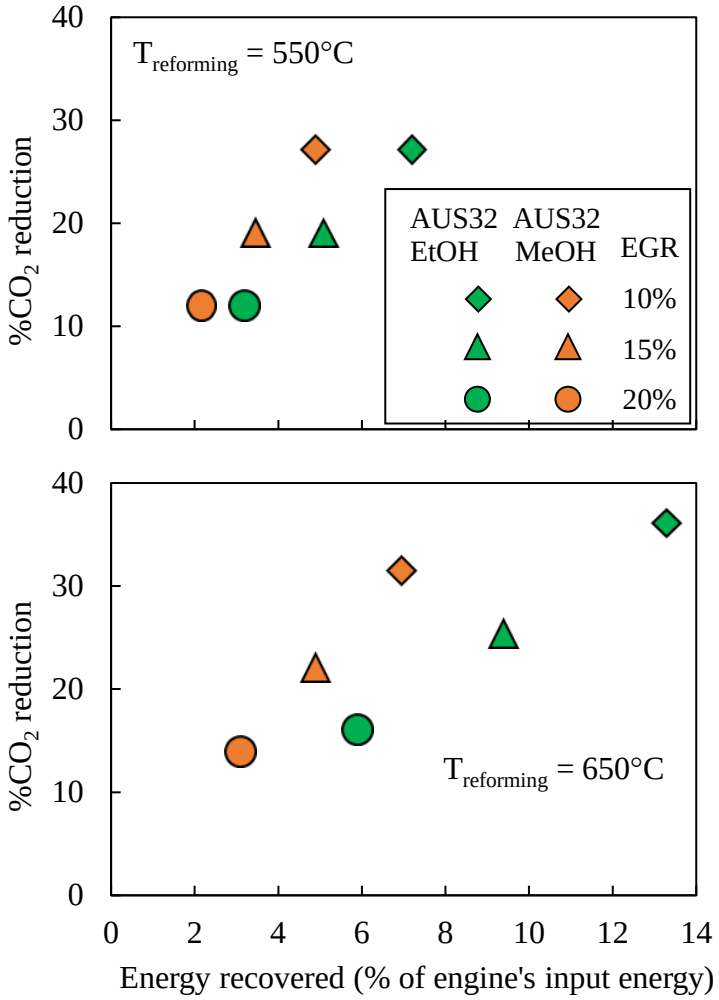

Figure 6-8: Tail-pipe CO_2 reduction and energy recovery as a function of engine's input energy if e-fuel derived reformate is added via intake manifold to replace gasoline

The GHG emission from the well-to-wheel analysis of proposed carbon neutral H_2 carriers are illustrated in **Figure 6-9** in comparison to baseline gasoline production (average

GHG emission = 92.4gCO_2/$MJ_{gasoline}$). Summary of well-to-wheel CO_2 emission of H_2 carriers from various production routes are illustrated in **Table 6-2**. The chart indicates the feasibility of utilising urea, ethanol and methanol produced from renewable energy (RE) for on-board H_2 production. The absence of carbon emission when using renewable energy enables the reduction of GHG emission in production to utilisation aspect for the proposed hydrogen carriers. When considering the improvement of the internal combustion engine's brake thermal efficiency by H_2 derived from the proposed H_2 carriers, further reduction of CO_2 emitted per fuel unit can be realised.

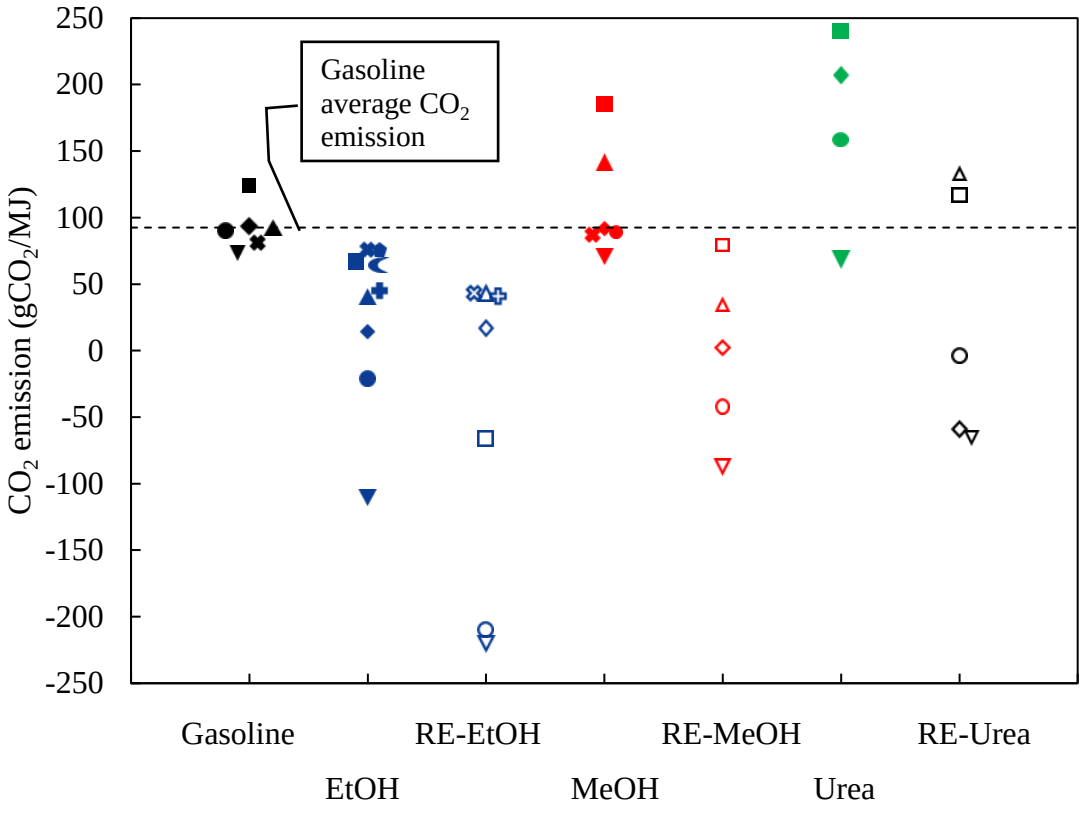

Figure 6-9: Impact of hydrogen carrier production routes on CO_2 emissions

Table 6-2 Summary of CO_2 emission of hydrogen carriers from different productions

Hydrogen carrier	Details (Feedstock/process or energy source)	Designator in Fig.6-9	CO_2 emission (gCO_2/MJ)	Ref.
Gasoline	Fossil based	◆	93.5	[203]
Gasoline	Fossil based	●	90.2	[204]
Gasoline	Fossil based	▲	92.8	[204]
Gasoline	Fossil based	✖	81	[178]
Gasoline	Fossil based	▼	73	[181]
Gasoline	Fossil based	■	123.91	[184]
EtOH	Corn/dry milling	✖	75.8	[203]
EtOH	Molasse	▲	41	[205]
EtOH	Corn/Natural gas	■	67.1	[203]
EtOH	Banagrass/fermentation	◆	14.4	[206]
EtOH	Corn natural gas	⬟	76	[207]
EtOH	Sugarcane	✚	45	[207]
EtOH	Corn	☾	64.3	[208]
EtOH	Sorghum with carbon capture and storage (CCS)	▼	-110.7	[209]
EtOH	Sorghum w/o CCS	●	-21.3	[209]
RE-EtOH	Grain via dry milling using renewable energy (RE)	□	-66	[21]
RE-EtOH	Biomass: wheat grains	○	-210	[21]
RE-EtOH	Biomass: wheat straw	▽	-221	[21]
RE-EtOH	Biomass: wheat straw	◇	17	[21]
RE-EtOH	Corn, nuclear + low temperature electrolysis (LTE) with H_2 recycle	△	44	[204]
RE-EtOH	Corn, wind + solar + LTE with H_2 recycle	⊠	43.1	[204]
RE-EtOH	Corn, wind + solar + LTE without H_2 recycle	✜	40.8	[204]
MeOH	Natural gas	▲	89	[210]

Hydrogen carrier	Details (Feedstock/process or energy source)	Designator in Fig.6-9	CO_2 emission (gCO_2/MJ)	Ref.
MeOH	Natural gas/ Electric from grid	●	141.9	[211]
MeOH	Natural gas	✖	87	[212]
MeOH	Forest residual	▼	70.2	[212]
MeOH	Coal	■	185	[212]
MeOH	Natural gas	◆	91.5	[213]
RE-MeOH	H_2 from H_2O, CO_2 from CCS, Renewable energy	▽	-87.94	[214]
RE-MeOH	H_2 from H_2O, CO from RWGS, Wind energy	◇	2	[210]
RE-MeOH	CO_2 from NH_3 production, excess renewable energy (ERE)	□	79.4	[213]
RE-MeOH	CO_2 from EtOH production, ERE	△	35	[213]
RE-MeOH	CO_2 from CCS, H_2 from H_2O, RE	○	-42.21	[215]
Urea	Syngas from Coal gasification	▼	67.77	[216]
Urea	Coal	◆	206.91	[217]
Urea	SR of CH_4 (SMR)	■	240.13	[218]
Urea	Biomass gasification	●	158.50	[218]
RE-Urea	Electrolysis H_2O, Solar	□	116.74	[218]
RE-Urea	Electrolysis H_2O, Biogas, Solar	△	133.83	[218]
RE-Urea	Renewable urea	○	-3.80	[215]
RE-Urea	Solar & wind energies	◇	-59.11	[219]
RE-Urea	CO_2 from carbon capture and utilisation (CCU)	▽	-66.44	[220]

6.8 Summary

From the knowledge of AUS32 decomposition established in the previous chapter, AUS32 demonstrated its potential as a prospective H_2 carrier for on-board H_2 production application. This chapter demonstrates the H_2 production from the combination of carbon

neutral H_2 carriers (AUS32+ethanol and AUS32+methanol) through exhaust gas reforming. The high miscibility of ethanol and methanol enables AUS32 to be used as the steam source for steam reforming of ethanol and methanol (e-fuel). The thermodynamic analysis is performed alongside the experimental study. In order to investigate the effect of reforming temperature, reactant injection rate (which effectively alter O_2/C ratio), and gas species in GDI exhaust gas (e.g. CO_2, H_2O, CO, THCs) on H_2 production and reformate gas compositions.

Reforming process efficiency above 100% is observed at a reforming temperature of 650°C for both AUS32+ethanol and AUS32+methanol reforming. Low reactant injection rate leads to high degree of oxidation and reduced H_2 yield which results in low reforming process efficiency, especially at reforming temperature of 550°C. High ethanol and methanol conversion efficiencies are observed. Meanwhile, substantially lower conversion efficiency of urea is because of high H_2O concentration combined with insufficient resident time to complete the decomposition process. Catalyst inhibition because of molecular H_2O absorption is the main mechanism that limits dehydrogenation of NH_3. Hence, the high NH_3 concentration is detected in the reformate.

AUS32+ethanol reforming generates higher H_2 yield than that of AUS32+methanol reforming as the result of higher hydrogen content of ethanol compared to methanol. At 650°C, AUS32+ethanol reforming generates up to 30%-vol in comparison to 25%-vol H_2 from AUS32+methanol reforming. However, at lower temperature (550°C), the methanol's superior reforming properties at low temperature demonstrates higher H_2 yield than that of ethanol (22%-vol compared to 19%-vol).

High concentration of hydrocarbons is detected in the reformate gas produced from both AUS32+ethanol and AUS32+methanol reforming as the by-product of hydrogenation of CO_2. Methane is the main carbon product in the reformate as predicted by the equilibrium

calculations. Meanwhile, other heavier hydrocarbons are also be detected. Traces of ethylene is found in the reformate indicating a precursor to coke formation. The results demonstrate the elevated reforming temperature and O_2/C ratio can help to further reduce coke formation precursor.

The estimation of the impact on tailpipe CO_2 reduction and waste heat energy recovery reveal that using H_2 reformate from AUS32+ethanol reforming can reduce CO_2 up to 36% compared to baseline GDI engine operated on conventional gasoline. Reformate from AUS32+methanol reforming indicates noticeably lower CO_2 reduction due mainly to lower H_2 concentration in the reformate. However, at a low reforming temperature (550°C), reformate from AUS32+methanol demonstrates similar performance in reducing CO_2 due to higher H_2/CO ratio of the reformate. Methanol's lower enthalpy of reaction results in relatively lower waste heat energy recovery compared to AUS32+ethanol reforming. Well-to-wheel analysis reveals that proposed H_2 carriers derived from excess renewable energy can neutralise GHG emission and effectively decarbonise the transportation sector.

Chapter 7 Conclusions and future works

This thesis has studied on-board hydrogen production from various feedstocks through both thermodynamics analysis and experimental methods. This thesis focuses on the hydrogen production from carbon neutral hydrogen carriers (e.g. ammonia, aqueous urea solution, ethanol, and methanol) through decomposition/reforming with GDI engine exhaust gas. The conclusion of major findings of this thesis work are as follow:

7.1 Concluding remarks

Energy recovery via catalytic ammonia decomposition for on-board hydrogen production

Ammonia is one of the most promising hydrogen carriers as a solution to the hydrogen storage problem via on-board hydrogen production. The carbon-free nature of ammonia made it one of the best candidates for on-board hydrogen production given no additional carbonaceous emission during its usage. The study demonstrates that hydrogen production from decomposing ammonia was achievable for on-board application at typical operating conditions of a GDI engine. Process efficiency up to 119% was realised. The results revealed significant tail-pipe greenhouse gas reduction of 32% could be attained using hydrogen derived from ammonia decomposition. The proposed process was also able to recover waste heat energy from exhaust gas to use in the decomposition process. Hence, the thermal efficiency of the internal combustion engine could be further enhanced with the proposed technique. The study presented here demonstrated that the use of ammonia in vehicular application could be beneficial as a carbon-free hydrogen carrier and energy carrier (as fuel) for the transportation sector regarding

current state of environmental concerns. The environmental benefits of utilising ammonia can be more significant if renewable energy is used in ammonia production processes.

Aqueous urea decomposition

In this study, aqueous urea solution (AUS32 or AdBlue) was used as hydrogen carrier for hydrogen production through urea decomposition with GDI exhaust gas. The use of aqueous urea solution to generate hydrogen proved to be a feasible method for on-board applications. Especially, when considering using waste heat energy from GDI exhaust gas for decomposition process. Maximum hydrogen yield of 15%-vol was achieved with the process efficiency of 128%. Tail-pipe CO_2 reduction up to 18% (approx.) was estimated in the scenario that hydrogen produced from AUS32 replaced gasoline fuel. The merit of using aqueous urea solution was not only enable the safety of the system, and simplicity of the urea supplying system, but also its practicality to implement the hydrogen product system given the availability of urea solution to end-users. This study broadened the application of aqueous urea solution from a NO_x emission control reducing agent to a prospective hydrogen carrier for vehicular applications. The use of cleaner and environmentally friendly 'green urea' produced from sustainable energy will further improve the decarbonisation potential of the system. The outcome of this research can help automakers to implement and adopt on-board hydrogen production technology to maximise the energy efficiency and minimise emissions of internal combustion engine vehicles.

Hydrogen production from carbon-neutral hydrogen carriers

Ethanol and methanol are the two most promising electrofuel candidates for on-board hydrogen production applications given their advantages in aspect of fuel for internal combustion engines, excellent properties regarding fuel reforming, and benefit of being carbon-

neutral fuels (as a result of electrofuel production concept). This study demonstrated the use of aqueous urea solution as steam replacement to formulate urea-ethanol and urea-methanol blends for hydrogen production application. The use of proposed hydrogen carriers demonstrated an enhanced hydrogen production and substantial exhaust gas waste heat energy recovery. Hydrogen production from proposed hydrogen carrier blends could reach hydrogen yield of 30%-vol which indicated process efficiency of 127%. The calculation revealed up to 36% CO_2 reduction was attainable considering well-to-wheel analysis. The findings of this study can help enable the utilisation of proposed electrofuel in the transportation sector to become more viable with a lower impact on greenhouse gas emission to achieve carbon emission neutrality.

7.2 General closing remarks

The high exhaust gas temperature of the GDI engine in comparison to that of diesel engine makes catalytic thermochemical energy recovery a thermodynamically feasible technique. Harvesting waste heat energy from GDI exhaust gas to produce hydrogen on-demand from carbon neutral hydrogen carriers can push the limit of the internal combustion engines in terms of thermal efficiency and emissions. The proposed technology is also an important steppingstone during the transition of the transportation sector into full-on electrification in the near future. The findings of this research can help the transportation sector to adopt the fuel reforming technology for on-board hydrogen production from proposed hydrogen carriers which helps reduce carbon footprint of road vehicles and advance the transportation sector toward the zero-carbon society. The research can also help bridge the gap between the carbon neutral energy carrier supply and the demand from the transportation sector

through using proposed fuel reforming technology. The use of cleaner energy vectors to control greenhouse gas emission will be the key to address the global climate change problem.

7.3 Future works

- Regarding thermodynamic study, the future work should focus on an extensive thermodynamic study of proposed H_2 carriers with exhaust gas from GDI engines operated at lean air-fuel ratio. For instance, an investigation on H_2 production and waste heat energy recovery of GDI engines operating in stratified charge mode. The higher oxygen content in the exhaust gas and lower EGT will be a challenge for H_2 production.
- A development of a full-scale reformer for thermochemical energy recovery experiment with GDI engine in steady-state and transient state modes should be conducted specifically with the proposed H_2 carriers. This investigation will enable validation of the thermodynamic study results regarding waste heat energy recovery, fuel economy improvement, brake thermal efficiency improvement, and emissions reduction.
- As H_2-containing product gas from AUS32 decomposition contains significant H_2O fraction, a study of the effect of high-water content reformate on the engine combustion characteristic should be investigated. With the current trend of downsizing the engine to continue, this will result in the engine operating at higher IMEP which prevents knocking (self-ignition) will be the main challenge. Water can affect the combustion phasing which can be beneficial for preventing knocking at high engine load. A robust and active engine management will be needed to maintain high engine efficiency and good emission characteristics.

List of references

[1] R. Lindsey and L. Dahlman, “Climate Change: Global Temperature,” 2020. https://www.climate.gov/news-features/understanding-climate/climate-change-global-temperature (accessed Jun. 03, 2020).

[2] Z. Yang, B. Wang, and K. Jiao, “Life cycle assessment of fuel cell, electric and internal combustion engine vehicles under different fuel scenarios and driving mileages in China,” *Energy*, vol. 198, p. 117365, 2020, doi: https://doi.org/10.1016/j.energy.2020.117365.

[3] A. Wanitschke and S. Hoffmann, “Are battery electric vehicles the future? An uncertainty comparison with hydrogen and combustion engines,” *Environ. Innov. Soc. Transitions*, vol. 35, pp. 509–523, 2020, doi: https://doi.org/10.1016/j.eist.2019.03.003.

[4] R. D. Reitz *et al.*, “IJER editorial: The future of the internal combustion engine,” *Int. J. Engine Res.*, vol. 21, no. 1, pp. 3–10, Sep. 2019, doi: 10.1177/1468087419877990.

[5] S. Golunski, “What is the point of on-board fuel reforming?,” *Energy Environ. Sci.*, vol. 3, no. 12, pp. 1918–1923, 2010, doi: 10.1039/C0EE00252F.

[6] D. Fennell *et al.*, “On-board thermochemical energy recovery technology for low carbon clean gasoline direct injection engine powered vehicles,” *Proc. Inst. Mech. Eng. Part D J. Automob. Eng.*, pp. 1–13, 2017, doi: 10.1177/0954407017726701.

[7] B. P. Leung, J. M. Herreros, M. L. Wyszynski, and S. E. Golunski, “Using Catalytic Heat Recovery to Improve Efficiency of Gasoline Spark Ignition Engines,” *Johnson Matthey Technol. Rev.*, vol. 62, no. 4, pp. 407–416, 2018, [Online]. Available: https://doi.org/10.1595/205651318X15318154729616.

[8] A. N. Rollinson, G. L. Rickett, A. Lea-Langton, V. Dupont, and M. V. Twigg, “Hydrogen from urea-water and ammonia-water solutions,” *Appl. Catal. B Environ.*, vol. 106, no. 3–4, pp. 304–315, 2011, doi: 10.1016/j.apcatb.2011.05.031.

[9] K. W. Lin and H. W. Wu, “Hydrogen-rich syngas production of urea blended with biobutanol by a thermodynamic analysis,” *Int. J. Hydrogen Energy*, vol. 43, no. 37, pp. 17562–17573, 2018, doi: 10.1016/j.ijhydene.2018.07.184.

[10] H. Wu and K. Lin, “Hydrogen-rich syngas production by reforming of ethanol blended with aqueous urea using a thermodynamic analysis,” *Energy*, vol. 166, pp. 541–551, 2019, [Online]. Available: https://doi.org/10.1016/j.energy.2018.10.122.

[11] H. W. Wu and K. W. Lin, “Thermodynamic analysis of hydrogen-rich syngas

production with a mixture of aqueous urea and biodiesel," *Int. J. Hydrogen Energy*, vol. 43, no. 14, pp. 6804–6814, 2018, doi: 10.1016/j.ijhydene.2018.02.126.

[12] P. Ebrahimi, A. Kumar, and M. Khraisheh, "Thermodynamic assessment of effect of ammonia, hydrazine and urea on water gas shift reaction," *Int. J. Hydrogen Energy*, 2020, doi: https://doi.org/10.1016/j.ijhydene.2020.11.056.

[13] D. Fennell, J. Herreros, A. Tsolakis, K. Cockle, J. Pignon, and P. Millington, "Thermochemical recovery technology for improved modern engine fuel economy – part 1: analysis of a prototype exhaust gas fuel reformer," *RSC Adv.*, vol. 5, no. 44, pp. 35252–35261, 2015, doi: 10.1039/C5RA03111G.

[14] T. Jiwanuruk, S. Putivisutisak, P. Vas-Umnuay, P. Bumroongsakulsawat, C. K. Cheng, and S. Assabumrungrat, "Modeling of thermally-coupled monolithic membrane reformer for vehicular hydrogen production," *Int. J. Hydrogen Energy*, vol. 42, no. 42, pp. 26308–26319, 2017, doi: 10.1016/j.ijhydene.2017.08.210.

[15] S. Jung, B. Choi, S. Park, D. W. Lee, and Y. B. Kim, "Hydrogen production by compact combined dimethyl ether reformer/combustor for automotive applications," *Int. J. Hydrogen Energy*, vol. 42, no. 19, pp. 13463–13476, 2017, doi: 10.1016/j.ijhydene.2016.11.199.

[16] J. Singh, H. Nozari, J. M. Herreros, and A. Tsolakis, "Synergies between aliphatic bio-alcohols and thermo-chemical waste heat recovery for reduced CO2 emissions in vehicles," *Fuel*, vol. 304, p. 121439, 2021, doi: https://doi.org/10.1016/j.fuel.2021.121439.

[17] S. Ogo and Y. Sekine, "Recent progress in ethanol steam reforming using non-noble transition metal catalysts: A review," *Fuel Process. Technol.*, vol. 199, p. 106238, 2020, doi: https://doi.org/10.1016/j.fuproc.2019.106238.

[18] F. Rau, A. Herrmann, H. Krause, D. Fino, and D. Trimis, "Production of hydrogen by autothermal reforming of biogas Production of hydrogen by autothermal reforming of biogas Assessing the feasibility of using the heat temperature function for a long-term di," *Energy Procedia*, vol. 120, pp. 294–301, 2017, doi: 10.1016/j.egypro.2017.07.218.

[19] B. Kumar, S. Kumar, and S. Kumar, "Thermodynamic and energy analysis of renewable butanol – ethanol fuel reforming for the production of hydrogen," *J. Environ. Chem. Eng.*, vol. 5, no. 6, pp. 5876–5890, 2017, doi: 10.1016/j.jece.2017.10.049.

[20] D. Kim, G. Park, B. Choi, and Y. Kim, “Reaction characteristics of dimethyl ether (DME) steam reforming catalysts for hydrogen production,” *Int. J. Hydrogen Energy*, vol. 42, no. 49, pp. 29210–29221, 2017, doi: 10.1016/j.ijhydene.2017.10.020.

[21] B. Buchspies, M. Kaltschmitt, and U. Neuling, “Potential changes in GHG emissions arising from the introduction of biorefineries combining biofuel and electrofuel production within the European Union – A location specific assessment,” *Renew. Sustain. Energy Rev.*, vol. 134, p. 110395, 2020, doi: https://doi.org/10.1016/j.rser.2020.110395.

[22] B. R. de Vasconcelos and J. M. Lavoie, “Recent advances in power-to-X technology for the production of fuels and chemicals,” *Front. Chem.*, vol. 7, no. JUN, pp. 1–24, 2019, doi: 10.3389/fchem.2019.00392.

[23] M. Sterner and M. Specht, “Power-to-gas and power-to-x—the history and results of developing a new storage concept,” *Energies*, vol. 14, no. 20, pp. 1–18, 2021, doi: 10.3390/en14206594.

[24] D. Candelaresi and G. Spazzafumo, *Introduction: the power-to-fuel concept*. INC, 2021.

[25] C. Fernando and W. W. Purwanto, “Techno-economic analysis of a small-scale power-to-green urea plant,” *IOP Conf. Ser. Earth Environ. Sci.*, vol. 716, no. 1, 2021, doi: 10.1088/1755-1315/716/1/012010.

[26] M. E. E. Abashar, “Ultra-clean hydrogen production by ammonia decomposition,” *J. King Saud Univ. - Eng. Sci.*, vol. 30, no. 1, pp. 2–11, 2018, doi: 10.1016/j.jksues.2016.01.002.

[27] T. E. Bell, H. Ménard, J.-M. González Carballo, R. Tooze, and L. Torrente-Murciano, “Hydrogen production from ammonia decomposition using Co/γ-Al2O3 catalysts – Insights into the effect of synthetic method,” *Int. J. Hydrogen Energy*, vol. 45, no. 51, pp. 27210–27220, 2020, doi: https://doi.org/10.1016/j.ijhydene.2020.07.090.

[28] S. F. Kurtoğlu *et al.*, “COx-free hydrogen production from ammonia decomposition over sepiolite-supported nickel catalysts,” *Int. J. Hydrogen Energy*, vol. 3, 2018, doi: 10.1016/j.ijhydene.2018.04.057.

[29] S. Mukherjee, S. V. Devaguptapu, A. Sviripa, C. R. F. Lund, and G. Wu, “Low-temperature ammonia decomposition catalysts for hydrogen generation,” *Appl. Catal. B Environ.*, vol. 226, no. December 2017, pp. 162–181, 2018, doi:

10.1016/j.apcatb.2017.12.039.

[30] Z.-W. Wu, X. Li, Y.-H. Qin, L. Deng, C.-W. Wang, and X. Jiang, “Ammonia decomposition over SiO2-supported Ni–Co bimetallic catalyst for COx-free hydrogen generation,” *Int. J. Hydrogen Energy*, vol. 45, no. 30, pp. 15263–15269, 2020, doi: https://doi.org/10.1016/j.ijhydene.2020.04.007.

[31] X. Lu and A. Roldan, “Are Carbon-Based Materials Good Supports for the Catalytic Reforming of Ammonia?,” *J. Phys. Chem. C*, vol. 125, no. 29, pp. 15950–15958, Jul. 2021, doi: 10.1021/acs.jpcc.1c03996.

[32] V. Dupont, M. V. Twigg, A. N. Rollinson, and J. M. Jones, “Thermodynamics of hydrogen production from urea by steam reforming with and without in situ carbon dioxide sorption,” *Int. J. Hydrogen Energy*, vol. 38, no. 25, pp. 10260–10269, 2013, doi: 10.1016/j.ijhydene.2013.06.062.

[33] A. N. Rollinson, V. Dupont, G. L. Rickett, and M. V Twigg, “Hydrogen production by catalytic steam reforming of urea,” 2010.

[34] A. N. Rollinson, J. Jones, V. Dupont, and M. V Twigg, “Urea as a hydrogen carrier: a perspective on its potential for safe, sustainable and long-term energy supply,” *Energy Environ. Sci.*, vol. 4, no. 4, pp. 1216–1224, 2011, doi: 10.1039/C0EE00705F.

[35] C. Zamfirescu and I. Dincer, “Utilization of hydrogen produced from urea on board to improve performance of vehicles,” *Int. J. Hydrogen Energy*, vol. 36, no. 17, pp. 11425–11432, 2011, doi: 10.1016/j.ijhydene.2011.04.185.

[36] Y. Shen *et al.*, “Low-Temperature Methanol-Water Reforming over Alcohol Dehydrogenase and Immobilized Ruthenium Complex,” *ChemSusChem*, vol. n/a, no. n/a, Jul. 2021, doi: https://doi.org/10.1002/cssc.202101240.

[37] A. M. Ranjekar and G. D. Yadav, “Steam Reforming of Methanol for Hydrogen Production: A Critical Analysis of Catalysis, Processes, and Scope,” *Ind. Eng. Chem. Res.*, vol. 60, no. 1, pp. 89–113, Jan. 2021, doi: 10.1021/acs.iecr.0c05041.

[38] B. Sawatmongkhon, K. Theinnoi, T. Wongchang, C. Haoharn, C. Wongkhorsub, and A. Tsolakis, “Hydrogen Production via the Catalytic Partial Oxidation of Ethanol on a Platinum–Rhodium Catalyst: Effect of the Oxygen-to-Ethanol Molar Ratio and the Addition of Steam,” *Energy & Fuels*, vol. 33, no. 7, pp. 6742–6753, Jul. 2019, doi: 10.1021/acs.energyfuels.9b01398.

[39] J. T. Hwang, S. P. Kane, and W. F. Northrop, “Hydrous Ethanol Steam Reforming and

Thermochemical Recuperation to Improve Dual-Fuel Diesel Engine Emissions and Efficiency," *J. Energy Resour. Technol.*, vol. 141, no. 11, May 2019, doi: 10.1115/1.4043711.

[40] A. Kundu, Y. G. Shul, and D. H. Kim, "Chapter Seven - Methanol Reforming Processes," in *Advances in Fuel Cell*, vol. 1, T. S. Zhao, K.-D. Kreuer, and T. B. T.-A. in F. C. Van Nguyen, Eds. Elsevier Science, 2007, pp. 419–472.

[41] B. Sawatmongkhon, K. Theinnoi, T. Wongchang, C. Haoharn, C. Wongkhorsub, and E. Sukjit, "Modeling of Hydrogen Production from Catalytic Partial Oxidation of Ethanol over a Platinum–Rhodium-Supported Catalyst," *Energy & Fuels*, Feb. 2021, doi: 10.1021/acs.energyfuels.0c04125.

[42] K. Theinnoi, W. Temwutthikun, T. Wongchang, and B. Sawatmongkhon, "Application of Exhaust Gas Fuel Reforming in Diesel Engines Towards the Improvement Urban Air Qualities," *Energy Procedia*, vol. 152, pp. 875–882, 2018, doi: https://doi.org/10.1016/j.egypro.2018.09.257.

[43] S. Choi, J. Bae, J. Lee, and J. Cha, "Exhaust gas fuel reforming for hydrogen production with CGO-based precious metal catalysts," *Chem. Eng. Sci.*, vol. 163, pp. 206–214, 2017, doi: https://doi.org/10.1016/j.ces.2017.01.010.

[44] D. Fennell, J. Herreros, and A. Tsolakis, "Improving gasoline direct injection (GDI) engine efficiency and emissions with hydrogen from exhaust gas fuel reforming," *Int. J. Hydrogen Energy*, vol. 39, no. 10, pp. 5153–5162, 2014, doi: 10.1016/j.ijhydene.2014.01.065.

[45] W. Wang, J. M. Herreros, A. Tsolakis, and A. P. E. York, "Ammonia as hydrogen carrier for transportation; Investigation of the ammonia exhaust gas fuel reforming," *Int. J. Hydrogen Energy*, vol. 38, no. 23, pp. 9907–9917, 2013, doi: 10.1016/j.ijhydene.2013.05.144.

[46] S. Sittichompoo *et al.*, "Exhaust energy recovery via catalytic ammonia decomposition to hydrogen for low carbon clean vehicles," *Fuel*, vol. 285, p. 119111, 2021, doi: https://doi.org/10.1016/j.fuel.2020.119111.

[47] R. Stone, *Introduction to Internal Combustion Engines*, 4th ed. Palgrave Macmillan, 2012.

[48] C. Jiang *et al.*, "Effect of fuel injector deposit on spray characteristics, gaseous emissions and particulate matter in a gasoline direct injection engine," *Appl. Energy*,

vol. 203, pp. 390–402, 2017, doi: 10.1016/j.apenergy.2017.06.020.

[49] J. Cooper and P. Phillips, “NOx Emissions Control for Euro 6,” *Platin. Met. Rev.*, vol. 57, no. 2, pp. 157–159, 2013, doi: 10.1595/147106713x663924.

[50] P. Mock, “ICCT EUROPEAN VEHICLE MARKET STATISTICS 2018/19,” 2018. [Online]. Available: www.theicct.org.

[51] and S. D. Uwe Tietge, Jan Dornoff, Peter Mock, “CO2 EMISSIONS FROM NEW PASSENGER CARS IN EUROPE: CAR MANUFACTURERS’ PERFORMANCE IN 2021,” 2022. [Online]. Available: https://theicct.org/publication/co2-new-passenger-cars-europe-aug22/.

[52] J. W. G. Turner *et al.*, “SuperGen on Ultraboost,” *SAE Int. J. Engines*, vol. 8, no. 4, pp. 1602–1615, Oct. 2015, [Online]. Available: http://www.jstor.org/stable/26278057.

[53] Y. S. Jo, L. Bromberg, and J. Heywood, “Optimal Use of Ethanol in Dual Fuel Applications,” *SAE Int. J. Engines*, vol. 9, no. 2, pp. 1087–1101, Oct. 2016, [Online]. Available: http://www.jstor.org/stable/26284880.

[54] W. H., Z. T., S. G., T. L., and W. Y., “Gasoline engine exhaust gas recirculation - A review,” *Appl. Energy*, vol. 99, no. X, pp. 534–544, 2012, doi: 10.1016/j.apenergy.2012.05.011.

[55] C. Hergueta, M. Bogarra, A. Tsolakis, K. Essa, and J. M. Herreros, “Butanol-gasoline blend and exhaust gas recirculation, impact on GDI engine emissions,” *Fuel*, vol. 208, pp. 662–672, 2017, doi: 10.1016/j.fuel.2017.07.022.

[56] C. Ji, T. Su, S. Wang, B. Zhang, M. Yu, and X. Cong, “Effect of hydrogen addition on combustion and emissions performance of a gasoline rotary engine at part load and stoichiometric conditions,” *Energy Convers. Manag.*, vol. 121, pp. 272–280, 2016, doi: 10.1016/j.enconman.2016.05.040.

[57] J. Kim, K. Min Chun, S. Song, H.-K. Baek, and S. Woo Lee, “The effects of hydrogen on the combustion, performance and emissions of a turbo gasoline direct-injection engine with exhaust gas recirculation,” *Int. J. Hydrogen Energy*, vol. 42, no. 39, pp. 25074–25087, 2017, doi: 10.1016/j.ijhydene.2017.08.097.

[58] W. Shi, X. Yu, H. Zhang, and H. Li, “Effect of spark timing on combustion and emissions of a hydrogen direct injection stratified gasoline engine,” *Int. J. Hydrogen Energy*, vol. 42, no. 8, pp. 5619–5626, 2017, doi: 10.1016/j.ijhydene.2016.02.060.

[59] Y. Karagöz, N. Yuca, T. Sandalcı, and A. S. Dalkılıç, “Effect of hydrogen and oxygen

addition as a mixture on emissions and performance characteristics of a gasoline engine," *Int. J. Hydrogen Energy*, vol. 40, no. 28, pp. 8750–8760, 2015, doi: 10.1016/j.ijhydene.2015.05.039.

[60] K. Ravi, J. Pradeep Bhasker, and E. Porpatham, "Effect of compression ratio and hydrogen addition on part throttle performance of a LPG fuelled lean burn spark ignition engine," *Fuel*, vol. 205, pp. 71–79, 2017, doi: 10.1016/j.fuel.2017.05.062.

[61] J. B. Heywood, *Internal Combustion Engine Fundamentals*, Internatio. McGraw-Hill, 1988.

[62] S. O. Akansu, S. Tangöz, N. Kahraman, M. İ. İlhak, and S. Açıkgöz, "Experimental study of gasoline-ethanol-hydrogen blends combustion in an SI engine," *Int. J. Hydrogen Energy*, vol. 42, no. 40, pp. 25781–25790, 2017, doi: 10.1016/j.ijhydene.2017.07.014.

[63] S. Raviteja and G. N. Kumar, "Effect of hydrogen addition on the performance and emission parameters of an SI engine fueled with butanol blends at stoichiometric conditions," *Int. J. Hydrogen Energy*, vol. 40, no. 30, pp. 9563–9569, 2015, doi: 10.1016/j.ijhydene.2015.05.171.

[64] Y. Du, X. Yu, L. Liu, R. Li, X. Zuo, and Y. Sun, "Effect of addition of hydrogen and exhaust gas recirculation on characteristics of hydrogen gasoline engine," *Int. J. Hydrogen Energy*, vol. 42, no. 12, pp. 8288–8298, 2017, doi: 10.1016/j.ijhydene.2017.02.197.

[65] S. Tangöz, N. Kahraman, and S. O. Akansu, "The effect of hydrogen on the performance and emissions of an SI engine having a high compression ratio fuelled by compressed natural gas," *Int. J. Hydrogen Energy*, vol. 42, no. 40, pp. 25766–25780, 2017, doi: 10.1016/j.ijhydene.2017.04.076.

[66] M. Mardani, A. Tsolakis, H. Nozari, J. Martin Herreros, A. Wahbi, and S. Sittichompoo, "Synergies in renewable fuels and exhaust heat thermochemical recovery in low carbon vehicles," *Appl. Energy*, vol. 302, no. August, p. 117491, 2021, doi: 10.1016/j.apenergy.2021.117491.

[67] V. Palma, C. Ruocco, E. Meloni, F. Gallucci, and A. Ricca, "Enhancing Pt-Ni/CeO2 performances for ethanol reforming by catalyst supporting on high surface silica," *Catal. Today*, vol. 307, pp. 175–188, 2018, doi: https://doi.org/10.1016/j.cattod.2017.05.034.

[68] W. Thavorncharoenpon and K. Theinnoi, “Feasibility Study of Hydrogen Production from Compression Ignition Engine Fueled with Biodiesel-Diesel Fuel Blends via Reforming Process,” in *2018 Third International Conference on Engineering Science and Innovative Technology (ESIT)*, 2018, pp. 1–4, doi: 10.1109/ESIT.2018.8665136.

[69] L. Wang, Y. Yi, Y. Zhao, R. Zhang, J. Zhang, and H. Guo, “NH3 Decomposition for H2 Generation: Effects of Cheap Metals and Supports on Plasma-Catalyst Synergy,” *ACS Catal.*, vol. 5, no. 7, pp. 4167–4174, 2015, doi: 10.1021/acscatal.5b00728.

[70] S. Chiuta and D. G. Bessarabov, “Design and operation of an ammonia-fueled microchannel reactor for autothermal hydrogen production,” *Catal. Today*, vol. 310, pp. 187–194, 2018, doi: https://doi.org/10.1016/j.cattod.2017.05.018.

[71] C. H. Christensen, T. Johannessen, R. Z. Sørensen, and J. K. Nørskov, “Towards an ammonia-mediated hydrogen economy?,” *Catal. Today*, vol. 111, no. 1–2, pp. 140–144, 2006, doi: 10.1016/j.cattod.2005.10.011.

[72] C. Bae and J. Kim, “Alternative fuels for internal combustion engines,” *Proc. Combust. Inst.*, vol. 36, no. 3, pp. 3389–3413, 2017, doi: 10.1016/j.proci.2016.09.009.

[73] S. Frigo and R. Gentili, “Analysis of the behaviour of a 4-stroke SI engine fuelled with ammonia and hydrogen,” *Int. J. Hydrogen Energy*, vol. 38, no. 3, pp. 1607–1615, 2013, doi: 10.1016/j.ijhydene.2012.10.114.

[74] C. S. Mørch, A. Bjerre, M. P. Gøttrup, S. C. Sorenson, and J. Schramm, “Ammonia/hydrogen mixtures in an SI-engine: Engine performance and analysis of a proposed fuel system,” *Fuel*, vol. 90, no. 2, pp. 854–864, 2011, doi: 10.1016/j.fuel.2010.09.042.

[75] K. Ryu, G. E. Zacharakis-Jutz, and S. C. Kong, “Effects of gaseous ammonia direct injection on performance characteristics of a spark-ignition engine,” *Appl. Energy*, vol. 116, pp. 206–215, 2014, doi: 10.1016/j.apenergy.2013.11.067.

[76] K. Ryu, G. E. Zacharakis-Jutz, and S. C. Kong, “Performance characteristics of compression-ignition engine using high concentration of ammonia mixed with dimethyl ether,” *Appl. Energy*, vol. 113, pp. 488–499, 2014, doi: 10.1016/j.apenergy.2013.07.065.

[77] F. Yan, L. Xu, and Y. Wang, “Application of hydrogen enriched natural gas in spark ignition IC engines: From fundamental fuel properties to engine performances and emissions,” *Renew. Sustain. Energy Rev.*, vol. 82, no. May 2017, pp. 1457–1488, 2017,

doi: 10.1016/j.rser.2017.05.227.

[78] National Center for Biotechnology Information, “PubChem Compound Summary for CID 783, Hydrogen,” *PubChem*. https://pubchem.ncbi.nlm.nih.gov/compound/Hydrogen (accessed Apr. 20, 2020).

[79] National Center for Biotechnology Information, “PubChem Compound Summary for CID 222, Ammonia,” *PubChem*. https://pubchem.ncbi.nlm.nih.gov/compound/Ammonia (accessed Apr. 20, 2020).

[80] S. Ishimatsu, T. Saika, and T. Nohara, “Ammonia Fueled Fuel Cell Vehicle :,” *SAE Tech. Pap.*, no. 2004-01–1925, pp. 1–7, 2004, doi: 10.4271/2004-01-1925.

[81] T. E. Bell and L. Torrente-Murciano, “H2 Production via Ammonia Decomposition Using Non-Noble Metal Catalysts: A Review,” *Top. Catal.*, vol. 59, no. 15–16, pp. 1438–1457, 2016, doi: 10.1007/s11244-016-0653-4.

[82] M. C. J. Bradford, P. E. Fanning, and M. A. Vannice, “Kinetics of NH3 Decomposition over Well Dispersed Ru,” *J. Catal.*, vol. 172, no. 2, pp. 479–484, 1997, doi: https://doi.org/10.1006/jcat.1997.1877.

[83] W. Tsai, J. J. Vajo, and W. H. Weinberg, “Inhibition by hydrogen of the heterogeneous decomposition of ammonia on platinum,” *J. Phys. Chem.*, vol. 89, no. 23, pp. 4926–4932, 1985, doi: 10.1021/j100269a009.

[84] T. V. Choudhary, C. Sivadinarayana, and D. W. Goodman, “Catalytic ammonia decomposition: COx-free hydrogen production for fuel cell applications,” *Catal. Letters*, vol. 72, no. 3–4, pp. 197–201, 2001, doi: 10.1023/A:1009023825549.

[85] Y. Saito, H. Mitsui, T. Nohara, Y. Aoki, and T. Saika, “Hydrogen Generation System with Ammonia Cracking for a Fuel-Cell Electric Vehicle,” *Transportation (Amst).*, vol. 4970, no. 2009-01–1901, 2009, doi: 10.4271/2009-01-1901.

[86] C. Plana, S. Armenise, A. Monzón, and E. García-Bordejé, “Ni on alumina-coated cordierite monoliths for in situ generation of CO-free H2 from ammonia,” *J. Catal.*, vol. 275, no. 2, pp. 228–235, 2010, doi: 10.1016/j.jcat.2010.07.026.

[87] N. Engelbrecht, S. Chiuta, and D. G. Bessarabov, “A highly efficient autothermal microchannel reactor for ammonia decomposition: Analysis of hydrogen production in transient and steady-state regimes,” *J. Power Sources*, vol. 386, no. March, pp. 47–55, 2018, doi: 10.1016/j.jpowsour.2018.03.043.

[88] D. Fennell, J. M. Herreros, A. Tsolakis, H. Xu, K. Cockle, and P. Millington, “GDI

Engine Performance and Emissions with Reformed Exhaust Gas Recirculation (REGR)," *SAE Int.*, no. 2013-01–0537, 2013, doi: 10.4271/2013-01-0537.

[89] J. H. Shin, G. J. Kim, and S. C. Hong, "Reaction properties of ruthenium over Ru/TiO2 for selective catalytic oxidation of ammonia to nitrogen," *Appl. Surf. Sci.*, vol. 506, p. 144906, 2020, doi: https://doi.org/10.1016/j.apsusc.2019.144906.

[90] L. Torrente-Murciano, A. K. Hill, and T. E. Bell, "Ammonia decomposition over cobalt/carbon catalysts—Effect of carbon support and electron donating promoter on activity," *Catal. Today*, vol. 286, no. June, pp. 131–140, 2017, doi: 10.1016/j.cattod.2016.05.041.

[91] S.-F. Yin, B.-Q. Xu, C.-F. Ng, and C.-T. Au, "Nano Ru/CNTs: a highly active and stable catalyst for the generation of COx-free hydrogen in ammonia decomposition," *Appl. Catal. B Environ.*, vol. 48, no. 4, pp. 237–241, 2004, doi: https://doi.org/10.1016/j.apcatb.2003.10.013.

[92] Z. Hu, J. Mahin, and L. Torrente-Murciano, "A MOF-templated approach for designing ruthenium–cesium catalysts for hydrogen generation from ammonia," *Int. J. Hydrogen Energy*, vol. 44, no. 57, pp. 30108–30118, 2019, doi: https://doi.org/10.1016/j.ijhydene.2019.09.174.

[93] X.-C. Hu *et al.*, "Ceria-supported ruthenium clusters transforming from isolated single atoms for hydrogen production via decomposition of ammonia," *Appl. Catal. B Environ.*, vol. 268, p. 118424, 2020, doi: https://doi.org/10.1016/j.apcatb.2019.118424.

[94] Z. Lendzion-Bielun, U. Narkiewicz, and W. Arabczyk, "Cobalt-based catalysts for ammonia decomposition," *Materials (Basel).*, vol. 6, no. 6, pp. 2400–2409, 2013, doi: 10.3390/ma6062400.

[95] K. Teramoto *et al.*, "Direct reforming of Methane–Ammonia mixed fuel on Ni–YSZ anode of solid oxide fuel cells," *Int. J. Hydrogen Energy*, vol. 45, no. 15, pp. 8965–8974, 2020, doi: https://doi.org/10.1016/j.ijhydene.2020.01.073.

[96] S. H. Oh and T. Triplett, "Reaction pathways and mechanism for ammonia formation and removal over palladium-based three-way catalysts: Multiple roles of CO," *Catal. Today*, vol. 231, pp. 22–32, 2014, doi: 10.1016/J.CATTOD.2013.11.048.

[97] J. H. Kim and O. C. Kwon, "A micro reforming system integrated with a heat-recirculating micro-combustor to produce hydrogen from ammonia," *Int. J. Hydrogen Energy*, vol. 36, no. 3, pp. 1974–1983, 2011, doi: 10.1016/j.ijhydene.2010.11.043.

[98] S. Chiuta, R. C. Everson, H. W. J. P. Neomagus, L. A. Le Grange, and D. G. Bessarabov, “A modelling evaluation of an ammonia-fuelled microchannel reformer for hydrogen generation,” *Int. J. Hydrogen Energy*, vol. 39, no. 22, pp. 11390–11402, 2014, doi: 10.1016/j.ijhydene.2014.05.146.

[99] R. Can Seyfeli and D. Varisli, “Ammonia decomposition reaction to produce COx-free hydrogen using carbon supported cobalt catalysts in microwave heated reactor system,” *Int. J. Hydrogen Energy*, vol. 45, no. 60, pp. 34867–34878, 2020, doi: https://doi.org/10.1016/j.ijhydene.2020.01.124.

[100] A. Srifa, K. Okura, T. Okanishi, H. Muroyama, T. Matsui, and K. Eguchi, “Hydrogen production by ammonia decomposition over Cs-modified Co3Mo3N catalysts,” *Appl. Catal. B Environ.*, vol. 218, pp. 1–8, 2017, doi: 10.1016/j.apcatb.2017.06.034.

[101] G. Cinti and U. Desideri, “SOFC fuelled with reformed urea,” *Appl. Energy*, vol. 154, pp. 242–253, 2015, doi: 10.1016/j.apenergy.2015.04.126.

[102] National Center for Biotechnology Information, “PubChem Compound Summary for CID 1176, Urea,” *PubChem*. https://pubchem.ncbi.nlm.nih.gov/compound/Urea (accessed Jul. 03, 2019).

[103] S. Satyapal, J. Petrovic, C. Read, G. Thomas, and G. Ordaz, “The U.S. Department of Energy’s National Hydrogen Storage Project: Progress towards meeting hydrogen-powered vehicle requirements,” *Catal. Today*, vol. 120, no. 3-4 SPEC. ISS., pp. 246–256, 2007, doi: 10.1016/j.cattod.2006.09.022.

[104] J. Honorien, R. Fournet, P.-A. Glaude, and B. Sirjean, “Theoretical study of the gas-phase thermal decomposition of urea,” *Proc. Combust. Inst.*, 2020, doi: https://doi.org/10.1016/j.proci.2020.06.012.

[105] K.-W. Lin and H.-W. Wu, “Hydrogen-rich syngas production and carbon dioxide formation using aqueous urea solution in biogas steam reforming by thermodynamic analysis,” *Int. J. Hydrogen Energy*, vol. 45, no. 20, pp. 11593–11604, 2020, doi: https://doi.org/10.1016/j.ijhydene.2020.02.127.

[106] P. Lahijani, Z. A. Zainal, M. Mohammadi, and A. R. Mohamed, “Conversion of the greenhouse gas CO2 to the fuel gas CO via the Boudouard reaction: A review,” *Renew. Sustain. Energy Rev.*, vol. 41, pp. 615–632, 2015, doi: https://doi.org/10.1016/j.rser.2014.08.034.

[107] W.-J. Jang *et al.*, “Combined steam and carbon dioxide reforming of methane and side

reactions: Thermodynamic equilibrium analysis and experimental application," *Appl. Energy*, vol. 173, pp. 80–91, 2016, doi: https://doi.org/10.1016/j.apenergy.2016.04.006.

[108] V. Praveena and M. L. J. Martin, "A review on various after treatment techniques to reduce NOx emissions in a CI engine," *J. Energy Inst.*, vol. 91, no. 5, pp. 704–720, 2018, doi: https://doi.org/10.1016/j.joei.2017.05.010.

[109] T. Kim, B. Choi, and S. Jung, "Numerical analysis of the melting characteristics of a frozen urea-water solution by heat spreaders with a positive temperature coefficient heater," *Appl. Therm. Eng.*, vol. 119, pp. 275–282, 2017, doi: https://doi.org/10.1016/j.applthermaleng.2017.03.069.

[110] B.-C. Choi, Y. K. Kim, W.-N. Jhung, C.-H. Lee, and C.-Y. Hwang, "Experimental investigation on melting characteristics of frozen urea–water-solutions for a diesel SCR de-NOx-system," *Appl. Therm. Eng.*, vol. 50, no. 1, pp. 1235–1245, 2013, doi: https://doi.org/10.1016/j.applthermaleng.2012.08.008.

[111] P. Barbier and S. Sirop, "Method for preventing a risk of freezing in a reducing-agent feeding device of a selective catalytic reduction system." Google Patents, Sep. 28, 2021.

[112] P. Larsson, P. Ravenhill, and P. Tunestal, "NOx-Conversion Comparison of a SCR-Catalyst Using a Novel Biomimetic Effervescent Injector on a Heavy-Duty Engine," *SAE Int.*, vol. 2019-01–00, pp. 1–6, 2019, doi: 10.4271/2019-01-0047.

[113] M. Holtermann, J. Wicmar, and F. Dinkelacker, "Influence of the Backpressure on Urea Sprays Generated by an Air-Blast Atomizer for Large-Scale SCR-Applications," *SAE Int.*, vol. 2019-01–00, pp. 1–9, 2019, doi: 10.4271/2019-01-0046.

[114] G. M. Hasan Shahariar, H. Jo, and O. Lim, "Analysis of the spray wall impingement of urea-water solution for automotive SCR De-NOx systems automotive SCR De-NOx systems," *Energy Procedia*, vol. 158, pp. 1936–1941, 2019, doi: 10.1016/j.egypro.2019.01.448.

[115] L. Hua, Y. Zhao, J. Hu, T. Tao, and S.-J. Shuai, "Comparison Between Air-Assisted and Airless Urea Spray for Diesel SCR System by PDA and CFD," Apr. 2012, doi: https://doi.org/10.4271/2012-01-1081.

[116] D. R. Johnson, C. R. Bedick, N. N. Clark, and D. L. Mckain, "Design and testing of an independently controlled urea SCR retrofit system for the reduction of NOx emissions from marine diesels," *Environ. Sci. Technol.*, vol. 43, no. 10, pp. 3959–3963, 2009, doi:

10.1021/es900269p.

[117] Y. Okada, H. Hirabayashi, S. Sato, and H. Inoue, “Study on Improvement of NOx Reduction Performance at Low Temperature Using Urea Reforming Technology in Urea SCR System,” Apr. 2019, doi: https://doi.org/10.4271/2019-01-0317.

[118] G. M. H. Shahariar and O. T. Lim, “A study on urea-water solution spray-wall impingement process and solid deposit formation in urea-scr de-nox system,” *Energies*, vol. 12, no. 1, 2019, doi: 10.3390/en12010125.

[119] H. S. Um, D. Kim, and K. H. Kim, “Numerical study on the design of urea decomposition chamber in LP SCR system,” *Int. J. Nav. Archit. Ocean Eng.*, vol. 11, no. 1, pp. 307–313, 2019, doi: https://doi.org/10.1016/j.ijnaoe.2018.06.005.

[120] F. Qian, D. Ma, N. Zhu, P. Li, and X. Xu, “Research on Optimization Design of SCR Nozzle for National VI Heavy Duty Diesel Engine,” *Catalysts*, vol. 9, no. 452, 2019, doi: doi:10.3390/catal9050452.

[121] S. Tischer, M. Börnhorst, J. Amsler, G. Schoch, and O. Deutschmann, “Thermodynamics and reaction mechanism of urea decomposition,” *Phys. Chem. Chem. Phys.*, vol. 21, no. 30, pp. 16785–16797, 2019, doi: 10.1039/C9CP01529A.

[122] L. Ravasio, S. Ravelli, and M. Mustafa, “Thermal Efficiency of On-site, Small-scale Hydrogen Production Technologies using Liquid Hydrocarbon Fuels in Comparison to Electrolysis: a Case Study in Norway,” *Energy Procedia*, vol. 148, pp. 1002–1009, 2018, doi: https://doi.org/10.1016/j.egypro.2018.08.061.

[123] Y. Chen, H. Xu, Y. Wang, and G. Xiong, “Hydrogen production from the steam reforming of liquid hydrocarbons in membrane reactor,” *Catal. Today*, vol. 118, no. 1, pp. 136–143, 2006, doi: https://doi.org/10.1016/j.cattod.2005.12.004.

[124] A. S. Damle, “Hydrogen production by reforming of liquid hydrocarbons in a membrane reactor for portable power generation—Experimental studies,” *J. Power Sources*, vol. 186, no. 1, pp. 167–177, 2009, doi: https://doi.org/10.1016/j.jpowsour.2008.09.059.

[125] Y. Chen, H. Xu, Y. Wang, X. Jin, and G. Xiong, “Hydrogen production from liquid hydrocarbon fuels for PEMFC application,” *Fuel Process. Technol.*, vol. 87, no. 11, pp. 971–978, 2006, doi: https://doi.org/10.1016/j.fuproc.2006.07.007.

[126] P. Leung, A. Tsolakis, M. L. Wyszynski, J. Rodriguez-Fernandez, and A. Megaritis, “Performance, emissions and exhaust-gas reforming of an emulsified fuel: A

comparative study with conventional diesel fuel," *SAE Tech. Pap.*, vol. 4970, 2009, doi: 10.4271/2009-01-1809.

[127] K. Theinnoi, A. Tsolakis, S. Sitshebo, R. F. Cracknell, and R. H. Clark, "Fuels combustion effects on a passive mode silver/alumina HC-SCR catalyst activity in reducing NOx," *Chem. Eng. J.*, vol. 158, no. 3, pp. 468–473, 2010, doi: 10.1016/j.cej.2010.01.021.

[128] Y. T. Kwon, J. H. Baik, H. J. Kwon, and I. Nam, "Effect of hydrogen on the CO oxidation and NO reduction reactions over a commercial TWC," *Sci. Technol.*, vol. 52, no. 1991, pp. 2065–2065, 2001.

[129] M. Konsolakis, M. Vrontaki, G. Avgouropoulos, T. Ioannides, and I. V. Yentekakis, "Novel doubly-promoted catalysts for the lean NOxreduction by H2+ CO: Pd(K)/Al2O3-(TiO2)," *Appl. Catal. B Environ.*, vol. 68, no. 1–2, pp. 59–67, 2006, doi: 10.1016/j.apcatb.2006.07.011.

[130] V. Houel, P. Millington, R. Rajaram, and A. Tsolakis, "Promoting functions of H2 in diesel-SCR over silver catalysts," *Appl. Catal. B Environ.*, vol. 77, no. 1–2, pp. 29–34, 2007, doi: 10.1016/j.apcatb.2007.07.003.

[131] A. Abu-Jrai and A. Tsolakis, "The effect of H2 and CO on the selective catalytic reduction of NOx under real diesel engine exhaust conditions over Pt/Al2O3," *Int. J. Hydrogen Energy*, vol. 32, no. 12, pp. 2073–2080, 2007, doi: 10.1016/j.ijhydene.2006.10.003.

[132] A. Abu-Jrai, A. Tsolakis, K. Theinnoi, A. Megaritis, and S. E. Golunski, "Diesel exhaust-gas reforming for H2 addition to an aftertreatment unit," *Chem. Eng. J.*, vol. 141, no. 1–3, pp. 290–297, 2008, doi: 10.1016/j.cej.2007.12.028.

[133] S. Hemmings and A. Megaritis, "Periodically regenerating diesel particulate filter with a hydrogen/carbon monoxide mixture addition," *Int. J. Hydrogen Energy*, vol. 37, no. 4, pp. 3573–3584, 2012, doi: 10.1016/j.ijhydene.2011.11.062.

[134] K. Theinnoi, A. Tsolakis, B. Sawatmongkhon, and S. Chuepeng, "A Study of Hydrogen Addition on Diesel Oxidation Catalyst Activities under the Real Diesel Engine," *J. Res. Appl. meachanical Eng.*, vol. 1, no. 3, pp. 1–4, 2013.

[135] W. Hauptmann, M. Votsmeier, H. Vogel, and D. G. Vlachos, "Modeling the simultaneous oxidation of CO and H2on Pt - Promoting effect of H2on the CO-light-off," *Appl. Catal. A Gen.*, vol. 397, no. 1–2, pp. 174–182, 2011, doi:

10.1016/j.apcata.2011.02.031.

[136] X. Zheng, M. Schultze, J. Mantzaras, and R. Bombach, “Effects of hydrogen addition on the catalytic oxidation of carbon monoxide over platinum at power generation relevant temperatures,” *Proc. Combust. Inst.*, vol. 34, no. 2, pp. 3343–3350, 2013, doi: 10.1016/j.proci.2012.06.118.

[137] E. López, N. J. Divins, A. Anzola, S. Schbib, D. Borio, and J. Llorca, “Ethanol steam reforming for hydrogen generation over structured catalysts,” *Int. J. Hydrogen Energy*, vol. 38, no. 11, pp. 4418–4428, 2013, doi: https://doi.org/10.1016/j.ijhydene.2013.01.174.

[138] A. Simson, R. Farrauto, and M. Castaldi, “Steam reforming of ethanol/gasoline mixtures: Deactivation, regeneration and stable performance,” *Appl. Catal. B Environ.*, vol. 106, no. 3, pp. 295–303, 2011, doi: https://doi.org/10.1016/j.apcatb.2011.05.027.

[139] M. Ni, D. Y. C. Leung, and M. K. H. Leung, “A review on reforming bio-ethanol for hydrogen production,” *Int. J. Hydrogen Energy*, vol. 32, no. 15, pp. 3238–3247, 2007, doi: https://doi.org/10.1016/j.ijhydene.2007.04.038.

[140] P. D. Vaidya and A. E. Rodrigues, “Insight into steam reforming of ethanol to produce hydrogen for fuel cells,” *Chem. Eng. J.*, vol. 117, no. 1, pp. 39–49, 2006, doi: https://doi.org/10.1016/j.cej.2005.12.008.

[141] V. Klouz *et al.*, “Ethanol reforming for hydrogen production in a hybrid electric vehicle: process optimisation,” *J. Power Sources*, vol. 105, no. 1, pp. 26–34, 2002, doi: https://doi.org/10.1016/S0378-7753(01)00922-3.

[142] T. Hou, S. Zhang, Y. Chen, D. Wang, and W. Cai, “Hydrogen production from ethanol reforming: Catalysts and reaction mechanism,” *Renew. Sustain. Energy Rev.*, vol. 44, pp. 132–148, 2015, doi: 10.1016/j.rser.2014.12.023.

[143] W. Wang and Y. Wang, “Dry reforming of ethanol for hydrogen production: thermodynamic investigation,” *Int. J. Hydrogen Energy*, vol. 34, no. 13, pp. 5382–5389, 2009.

[144] P. Nikolaidis and A. Poullikkas, “A comparative overview of hydrogen production processes,” *Renew. Sustain. energy Rev.*, vol. 67, pp. 597–611, 2017.

[145] N. C. for B. Information, “PubChem Compound Summary for CID 702, Ethanol,” *PubChem*. https://pubchem.ncbi.nlm.nih.gov/compound/Ethanol (accessed Apr. 09, 2021).

[146] N. C. for B. Information, “PubChem Compound Summary for CID 887, Methanol,” *PubChem*. https://pubchem.ncbi.nlm.nih.gov/compound/Methanol (accessed Aug. 10, 2021).

[147] H. Jääskeläinen, “Waste heat recovery,” *DieselNet*, 2019. .

[148] D. Pashchenko, “Thermochemical waste-heat recuperation by steam methane reforming with flue gas addition,” *Int. J. Energy Res.*, vol. 43, no. 6, pp. 2216–2226, May 2019, doi: https://doi.org/10.1002/er.4436.

[149] C. Gaber, M. Demuth, C. Schluckner, and C. Hochenauer, “Thermochemical analysis and experimental investigation of a recuperative waste heat recovery system for the tri-reforming of light oil,” *Energy Convers. Manag.*, vol. 195, pp. 302–312, 2019, doi: https://doi.org/10.1016/j.enconman.2019.04.086.

[150] R. C. Brown, *Thermochemical processing of biomass: conversion into fuels, chemicals and power*. John Wiley & Sons, 2019.

[151] R. Saidur, M. Rezaei, W. K. Muzammil, M. H. Hassan, S. Paria, and M. Hasanuzzaman, “Technologies to recover exhaust heat from internal combustion engines,” *Renew. Sustain. Energy Rev.*, vol. 16, no. 8, pp. 5649–5659, 2012, doi: 10.1016/j.rser.2012.05.018.

[152] R. Zhao, D. Wen, W. Li, W. Zhuge, Y. Zhang, and Y. Yin, “Characteristic and regulation method of parallel turbocompound engine with steam injection for waste heat recovery,” *Energy*, vol. 208, p. 118422, 2020, doi: https://doi.org/10.1016/j.energy.2020.118422.

[153] R. Amirante, P. De Palma, E. Distaso, and P. Tamburrano, “Thermodynamic analysis of small-scale externally fired gas turbines and combined cycles using turbo-compound components for energy generation from solid biomass,” *Energy Convers. Manag.*, vol. 166, pp. 648–662, 2018, doi: https://doi.org/10.1016/j.enconman.2018.04.055.

[154] M. Yang *et al.*, “Matching method of electric turbo compound for two-stroke low-speed marine diesel engine,” *Appl. Therm. Eng.*, vol. 158, p. 113752, 2019, doi: https://doi.org/10.1016/j.applthermaleng.2019.113752.

[155] J. Dahl *et al.*, “Model Predictive Control of a Diesel Engine with Turbo Compound and Exhaust After-Treatment Constraints,” *IFAC-PapersOnLine*, vol. 51, no. 31, pp. 349–354, 2018, doi: https://doi.org/10.1016/j.ifacol.2018.10.072.

[156] L. Feng, W. Gao, H. Qin, and B. Xie, “Heat Recovery from Internal Combustion

Engine with Rankine Cycle," in *2010 Asia-Pacific Power and Energy Engineering Conference*, 2010, pp. 1–4, doi: 10.1109/APPEEC.2010.5448861.

[157] K. Mohammadi and J. G. McGowan, "Thermoeconomic analysis of multi-stage recuperative Brayton cycles: Part II – Waste energy recovery using CO2 and organic Rankine power cycles," *Energy Convers. Manag.*, vol. 185, pp. 920–934, 2019, doi: https://doi.org/10.1016/j.enconman.2019.01.091.

[158] P. Fuc, P. Lijewski, A. Ziolkowski, and M. Dobrzyński, "Dynamic test bed analysis of gas energy balance for a diesel exhaust system fit with a thermoelectric generator," *J. Electron. Mater.*, vol. 46, no. 5, pp. 3145–3155, 2017.

[159] S. Vale, L. Heber, P. J. Coelho, and C. M. Silva, "Parametric study of a thermoelectric generator system for exhaust gas energy recovery in diesel road freight transportation," *Energy Convers. Manag.*, vol. 133, pp. 167–177, 2017, doi: https://doi.org/10.1016/j.enconman.2016.11.064.

[160] N. Muralidhar, M. Himabindu, and R. V Ravikrishna, "Modeling of a hybrid electric heavy duty vehicle to assess energy recovery using a thermoelectric generator," *Energy*, vol. 148, pp. 1046–1059, 2018, doi: https://doi.org/10.1016/j.energy.2018.02.023.

[161] T. Y. Kim and J. Kim, "Assessment of the energy recovery potential of a thermoelectric generator system for passenger vehicles under various drive cycles," *Energy*, vol. 143, pp. 363–371, 2018, doi: https://doi.org/10.1016/j.energy.2017.10.137.

[162] R. Ramírez, A. S. Gutiérrez, J. J. Cabello Eras, K. Valencia, B. Hernández, and J. Duarte Forero, "Evaluation of the energy recovery potential of thermoelectric generators in diesel engines," *J. Clean. Prod.*, vol. 241, p. 118412, 2019, doi: https://doi.org/10.1016/j.jclepro.2019.118412.

[163] E. Massaguer, A. Massaguer, T. Pujol, M. Comamala, L. Montoro, and J. R. Gonzalez, "Fuel economy analysis under a WLTP cycle on a mid-size vehicle equipped with a thermoelectric energy recovery system," *Energy*, vol. 179, pp. 306–314, 2019, doi: https://doi.org/10.1016/j.energy.2019.05.004.

[164] H. Nozari and A. Karabeyoğlu, "Numerical study of combustion characteristics of ammonia as a renewable fuel and establishment of reduced reaction mechanisms," *Fuel*, vol. 159, pp. 223–233, 2015, doi: 10.1016/j.fuel.2015.06.075.

[165] H. Nozari and A. M. Karabeyoglu, “Combustion characteristics of ammonia as a renewable energy source and development of reduced chemical mechanisms,” Jul. 2015, doi: doi:10.2514/6.2015-3917.

[166] A. A. Konnov, “Implementation of the NCN pathway of prompt-NO formation in the detailed reaction mechanism,” *Combust. Flame*, vol. 156, no. 11, pp. 2093–2105, 2009, doi: 10.1016/j.combustflame.2009.03.016.

[167] A. A. Konnov, “Yet another kinetic mechanism for hydrogen combustion,” *Combust. Flame*, vol. 203, pp. 14–22, 2019, doi: https://doi.org/10.1016/j.combustflame.2019.01.032.

[168] R. Gholami, M. Alyani, and K. Smith, “Deactivation of Pd Catalysts by Water during Low Temperature Methane Oxidation Relevant to Natural Gas Vehicle Converters,” *Catalysts*, vol. 5, no. 2, pp. 561–594, 2015, doi: 10.3390/catal5020561.

[169] W. S. Kijlstra, J. C. M. L. Daamen, J. M. van de Graaf, B. van der Linden, E. K. Poels, and A. Bliek, “Inhibiting and deactivating effects of water on the selective catalytic reduction of nitric oxide with ammonia over MnOx/Al2O3,” *Appl. Catal. B Environ.*, vol. 7, no. 3, pp. 337–357, 1996, doi: https://doi.org/10.1016/0926-3373(95)00052-6.

[170] C. Philibert, “Producing ammonia and fertilizers : new opportunities from renewables,” *IEA-Renewable Energy Div.*, pp. 1–6, 2017.

[171] D. Flórez-Orrego and S. de Oliveira Junior, “On the efficiency, exergy costs and CO2 emission cost allocation for an integrated syngas and ammonia production plant,” *Energy*, vol. 117, no. 2016, pp. 341–360, 2016, doi: 10.1016/j.energy.2016.05.096.

[172] M. G. Heidlage, E. A. Kezar, K. C. Snow, and P. H. Pfromm, “Thermochemical Synthesis of Ammonia and Syngas from Natural Gas at Atmospheric Pressure,” *Ind. Eng. Chem. Res.*, vol. 56, no. 47, pp. 14014–14024, 2017, doi: 10.1021/acs.iecr.7b03173.

[173] D. Miura and T. Tezuka, “A comparative study of ammonia energy systems as a future energy carrier, with particular reference to vehicle use in Japan,” *Energy*, vol. 68, pp. 428–436, 2014, doi: https://doi.org/10.1016/j.energy.2014.02.108.

[174] U.S. Department of Energy, “Gate-to-Grave Life Cycle Analysis Model of Saline Aquifer Sequestration of Carbon Dioxide,” 2013. [Online]. Available: www.netl.doe.gov.

[175] I. Rafiqul, C. Weber, B. Lehmann, and A. Voss, “Energy efficiency improvements in

ammonia production—perspectives and uncertainties," *Energy*, vol. 30, no. 13, pp. 2487–2504, 2005, doi: https://doi.org/10.1016/j.energy.2004.12.004.

[176] Y. Bicer, I. Dincer, C. Zamfirescu, G. Vezina, and F. Raso, "Comparative life cycle assessment of various ammonia production methods," *J. Clean. Prod.*, vol. 135, pp. 1379–1395, 2016, doi: https://doi.org/10.1016/j.jclepro.2016.07.023.

[177] Natural Resources Canada (NRC), "Canadian Ammonia Producers: Benchmarking Energy Efficiency and Carbon Dioxide Emissions," 2007. [Online]. Available: https://www.nrcan.gc.ca/sites/www.nrcan.gc.ca/files/oee/pdf/industrial/technical-info/benchmarking/ammonia/pdf/ammonia-study.pdf.

[178] M. L. N. M. Carneiro *et al.*, "Potential of biofuels from algae: Comparison with fossil fuels, ethanol and biodiesel in Europe and Brazil through life cycle assessment (LCA)," *Renew. Sustain. Energy Rev.*, vol. 73, pp. 632–653, 2017, doi: https://doi.org/10.1016/j.rser.2017.01.152.

[179] J. A. M. Silva, D. Flórez-Orrego, and S. Oliveira, "An exergy based approach to determine production cost and CO2 allocation for petroleum derived fuels," *Energy*, vol. 67, pp. 490–495, 2014, doi: 10.1016/j.energy.2014.02.022.

[180] M. Morales, S. Gonzalez-García, G. Aroca, and M. T. Moreira, "Life cycle assessment of gasoline production and use in Chile," *Sci. Total Environ.*, vol. 505, pp. 833–843, 2015, doi: https://doi.org/10.1016/j.scitotenv.2014.10.067.

[181] O. Cavalett, M. F. Chagas, J. E. A. Seabra, and A. Bonomi, "Comparative LCA of ethanol versus gasoline in Brazil using different LCIA methods," *Int. J. Life Cycle Assess.*, vol. 18, no. 3, pp. 647–658, 2013.

[182] S. González-García, M. T. Moreira, and G. Feijoo, "Environmental aspects of eucalyptus based ethanol production and use," *Sci. Total Environ.*, vol. 438, pp. 1–8, 2012, doi: https://doi.org/10.1016/j.scitotenv.2012.07.044.

[183] L. T. Le, E. C. van Ierland, X. Zhu, and J. Wesseler, "Energy and greenhouse gas balances of cassava-based ethanol," *Biomass and Bioenergy*, vol. 51, pp. 125–135, 2013, doi: https://doi.org/10.1016/j.biombioe.2013.01.011.

[184] A. L. Borrion, M. C. McManus, and G. P. Hammond, "Environmental life cycle assessment of bioethanol production from wheat straw," *Biomass and Bioenergy*, vol. 47, pp. 9–19, 2012, doi: https://doi.org/10.1016/j.biombioe.2012.10.017.

[185] C. O. Blanco *et al.*, "The Impact of Water on Ru-Catalyzed Olefin Metathesis: Potent

Deactivating Effects Even at Low Water Concentrations," *ACS Catal.*, vol. 11, no. 2, pp. 893–899, Jan. 2021, doi: 10.1021/acscatal.0c04279.

[186] M. J. Bos, S. R. A. Kersten, and D. W. F. Brilman, "Wind power to methanol: Renewable methanol production using electricity, electrolysis of water and CO2 air capture," *Appl. Energy*, vol. 264, p. 114672, 2020, doi: https://doi.org/10.1016/j.apenergy.2020.114672.

[187] S. S. Ali, S. S. Ali, and N. Tabassum, "A review on CO2 hydrogenation to ethanol: Reaction mechanism and experimental studies," *J. Environ. Chem. Eng.*, vol. 10, no. 1, p. 106962, 2022, doi: https://doi.org/10.1016/j.jece.2021.106962.

[188] Q. Wu, C. Shen, N. Rui, K. Sun, and C. Liu, "Experimental and theoretical studies of CO2 hydrogenation to methanol on Ru/In2O3," *J. CO2 Util.*, vol. 53, p. 101720, 2021, doi: https://doi.org/10.1016/j.jcou.2021.101720.

[189] B. G. Schieweck, P. Jürling-Will, and J. Klankermayer, "Structurally Versatile Ligand System for the Ruthenium Catalyzed One-Pot Hydrogenation of CO2 to Methanol," *ACS Catal.*, vol. 10, no. 6, pp. 3890–3894, Mar. 2020, doi: 10.1021/acscatal.9b04977.

[190] K. Hashimoto and N. Toukai, "Decomposition of ammonia over a catalyst consisting of ruthenium metal and cerium oxides supported on Y-form zeolite," *J. Mol. Catal. A Chem.*, vol. 161, no. 1, pp. 171–178, 2000, doi: https://doi.org/10.1016/S1381-1169(00)00332-0.

[191] E. Baraj, K. Ciahotný, and T. Hlinčík, "The water gas shift reaction: Catalysts and reaction mechanism," *Fuel*, vol. 288, p. 119817, 2021, doi: https://doi.org/10.1016/j.fuel.2020.119817.

[192] S. McDonagh, D. M. Wall, P. Deane, and J. D. Murphy, "The effect of electricity markets, and renewable electricity penetration, on the levelised cost of energy of an advanced electro-fuel system incorporating carbon capture and utilisation," *Renew. Energy*, vol. 131, pp. 364–371, 2019, doi: https://doi.org/10.1016/j.renene.2018.07.058.

[193] L. Weimann, A. Grimm, J. Nienhuis, P. Gabrielli, G. J. Kramer, and M. Gazzania, "Energy System Design for the Production of Synthetic Carbon-neutral Fuels from Air-captured CO2," in *30 European Symposium on Computer Aided Process Engineering*, vol. 48, S. Pierucci, F. Manenti, G. L. Bozzano, and D. B. T.-C. A. C. E. Manca, Eds. Elsevier, 2020, pp. 1471–1476.

[194] J. Ashok, M. H. Wai, and S. Kawi, "Nickel-based Catalysts for High-temperature

Water Gas Shift Reaction-Methane Suppression," *ChemCatChem*, vol. 10, no. 18, pp. 3927–3942, Sep. 2018, doi: https://doi.org/10.1002/cctc.201800031.

[195] P. Hongmanorom *et al.*, "Zr–Ce-incorporated Ni/SBA-15 catalyst for high-temperature water gas shift reaction: Methane suppression by incorporated Zr and Ce," *J. Catal.*, vol. 387, pp. 47–61, 2020, doi: https://doi.org/10.1016/j.jcat.2019.11.042.

[196] J. Cored *et al.*, "Hydrothermal Synthesis of Ruthenium Nanoparticles with a Metallic Core and a Ruthenium Carbide Shell for Low-Temperature Activation of CO2 to Methane," *J. Am. Chem. Soc.*, vol. 141, no. 49, pp. 19304–19311, Dec. 2019, doi: 10.1021/jacs.9b07088.

[197] F. Geng, Y. Bonita, V. Jain, M. Magiera, N. Rai, and J. C. Hicks, "Bimetallic Ru–Mo Phosphide Catalysts for the Hydrogenation of CO2 to Methanol," *Ind. Eng. Chem. Res.*, vol. 59, no. 15, pp. 6931–6943, Apr. 2020, doi: 10.1021/acs.iecr.9b06937.

[198] P. Tahay, Y. Khani, M. Jabari, F. Bahadoran, and N. Safari, "Highly porous monolith/TiO2 supported Cu, Cu-Ni, Ru, and Pt catalysts in methanol steam reforming process for H2 generation," *Appl. Catal. A Gen.*, vol. 554, pp. 44–53, 2018, doi: https://doi.org/10.1016/j.apcata.2018.01.022.

[199] R. Guil-López *et al.*, "Methanol Synthesis from CO2: A Review of the Latest Developments in Heterogeneous Catalysis," *Materials* , vol. 12, no. 23. 2019, doi: 10.3390/ma12233902.

[200] M. Bowker, "Methanol Synthesis from CO(2) Hydrogenation," *ChemCatChem*, vol. 11, no. 17, pp. 4238–4246, Sep. 2019, doi: 10.1002/cctc.201900401.

[201] A. Ochoa, J. Bilbao, A. G. Gayubo, and P. Castaño, "Coke formation and deactivation during catalytic reforming of biomass and waste pyrolysis products: A review," *Renew. Sustain. Energy Rev.*, vol. 119, p. 109600, 2020, doi: https://doi.org/10.1016/j.rser.2019.109600.

[202] F. Carvalho *et al.*, "Prospects for carbon-neutral maritime fuels production in Brazil," *J. Clean. Prod.*, vol. 326, p. 129385, 2021, doi: https://doi.org/10.1016/j.jclepro.2021.129385.

[203] M. Wang, M. Wu, and H. Huo, "Life-cycle energy and greenhouse gas emission impacts of different corn ethanol plant types," *Environ. Res. Lett.*, vol. 2, no. 2, p. 24001, 2007, doi: 10.1088/1748-9326/2/2/024001.

[204] G. Zang, P. Sun, A. Elgowainy, A. Bafana, and M. Wang, "Life Cycle Analysis of

Electrofuels: Fischer–Tropsch Fuel Production from Hydrogen and Corn Ethanol Byproduct CO2," *Environ. Sci. Technol.*, vol. 55, no. 6, pp. 3888–3897, Mar. 2021, doi: 10.1021/acs.est.0c05893.

[205] S. El Takriti, S. Searle, and N. Pavlenko, "Indirect greenhouse gas emissions of molasses ethanol in the European Union," *Retrieved from Int. Counc. Clean Transp. https//theicct. org/sites/default/files/publications/EU-molasses-ethanol-emissions_ICCT-working-paper_27092017_% 20vF. pdf*, 2017.

[206] J. Mochizuki, J. F. Yanagida, D. Kumar, D. Takara, and G. S. Murthy, "Life cycle assessment of ethanol production from tropical banagrass (Pennisetum purpureum) using green and dry processing technologies in Hawaii," *J. Renew. Sustain. Energy*, vol. 6, no. 4, p. 43128, 2014.

[207] M. Wang, J. Han, J. B. Dunn, H. Cai, and A. Elgowainy, "Well-to-wheels energy use and greenhouse gas emissions of ethanol from corn, sugarcane and cellulosic biomass for US use," *Environ. Res. Lett.*, vol. 7, no. 4, p. 45905, 2012, doi: 10.1088/1748-9326/7/4/045905.

[208] M. Gustafsson, N. Svensson, M. Eklund, J. Dahl Öberg, and A. Vehabovic, "Well-to-wheel greenhouse gas emissions of heavy-duty transports: Influence of electricity carbon intensity," *Transp. Res. Part D Transp. Environ.*, vol. 93, p. 102757, 2021, doi: https://doi.org/10.1016/j.trd.2021.102757.

[209] M. Yang, N. R. Baral, A. Anastasopoulou, H. M. Breunig, and C. D. Scown, "Cost and Life-Cycle Greenhouse Gas Implications of Integrating Biogas Upgrading and Carbon Capture Technologies in Cellulosic Biorefineries," *Environ. Sci. Technol.*, vol. 54, no. 20, pp. 12810–12819, Oct. 2020, doi: 10.1021/acs.est.0c02816.

[210] S. A. Isaacs, M. D. Staples, F. Allroggen, D. S. Mallapragada, C. P. Falter, and S. R. H. Barrett, "Environmental and Economic Performance of Hybrid Power-to-Liquid and Biomass-to-Liquid Fuel Production in the United States," *Environ. Sci. Technol.*, vol. 55, no. 12, pp. 8247–8257, Jun. 2021, doi: 10.1021/acs.est.0c07674.

[211] L. Rigamonti and E. Brivio, "Life cycle assessment of methanol production by a carbon capture and utilization technology applied to steel mill gases," *Int. J. Greenh. Gas Control*, vol. 115, p. 103616, 2022, doi: https://doi.org/10.1016/j.ijggc.2022.103616.

[212] J. J. Corbett and J. J. Winebrake, "Life Cycle Analysis of the use of Methanol for

Marin Transportation," *Prep. US Dep. Transp. Marit. Adm.*, 2018.

[213] G. Zang, P. Sun, A. Elgowainy, and M. Wang, "Technoeconomic and Life Cycle Analysis of Synthetic Methanol Production from Hydrogen and Industrial Byproduct CO2," *Environ. Sci. Technol.*, vol. 55, no. 8, pp. 5248–5257, Apr. 2021, doi: 10.1021/acs.est.0c08237.

[214] T. Cordero-Lanzac *et al.*, "A techno-economic and life cycle assessment for the production of green methanol from CO2: catalyst and process bottlenecks," *J. Energy Chem.*, vol. 68, pp. 255–266, 2022, doi: https://doi.org/10.1016/j.jechem.2021.09.045.

[215] A. Sánchez, L. M. Gil, and M. Martín, "Sustainable DMC production from CO2 and renewable ammonia and methanol," *J. CO2 Util.*, vol. 33, pp. 521–531, 2019, doi: https://doi.org/10.1016/j.jcou.2019.08.010.

[216] P. Kumar, S. Verma, A. Gupta, A. Ranjan Paul, A. Jain, and N. Haque, "Life Cycle Analysis for The Production of Urea Through Syngas," *IOP Conf. Ser. Earth Environ. Sci.*, vol. 795, no. 1, p. 12031, 2021, doi: 10.1088/1755-1315/795/1/012031.

[217] L. Shi, L. Liu, B. Yang, G. Sheng, and T. Xu, "Evaluation of Industrial Urea Energy Consumption (EC) Based on Life Cycle Assessment (LCA)," *Sustainability* , vol. 12, no. 9. 2020, doi: 10.3390/su12093793.

[218] M. Alfian and W. W. Purwanto, "Multi-objective optimization of green urea production," *Energy Sci. Eng.*, vol. 7, no. 2, pp. 292–304, 2019.

[219] H. Ishaq, O. Siddiqui, G. Chehade, and I. Dincer, "A solar and wind driven energy system for hydrogen and urea production with CO2 capturing," *Int. J. Hydrogen Energy*, vol. 46, no. 6, pp. 4749–4760, 2021, doi: 10.1016/j.ijhydene.2020.01.208.

[220] M. Chehrazi and B. K. Moghadas, "A review on CO2 capture with chilled ammonia and CO2 utilization in urea plant," *J. CO2 Util.*, vol. 61, p. 102030, 2022, doi: https://doi.org/10.1016/j.jcou.2022.102030.

Appendices

Appendix A: Arduino coding for the programmable fuel injection controller unit

```
//Injector controller unit: Controlled by serial monitor to start or stop injection
int modeSW = 2;         //Pin 2 for SW1 (middle) as manual on/off
int injtSW =  3;          //Pin 3 for SW2 (right) as mode select
int injector = 5;
int modeState = 0;
int injState = 0;
int serialControl = 0;      //'1' = injector will turn on PWRT, '0' = injector off at PWRT
byte PC  = 0;
void setup() {
  pinMode(modeSW, INPUT_PULLUP);
  pinMode(injtSW, INPUT_PULLUP);
  pinMode(injector, OUTPUT);
  Serial.begin(9600);
  Serial.println("Hello SAK!, This is fuel injector controller version 1.0-a");
  Serial.println("Press 'y' + 'Enter' to turn on injector");
  Serial.println("Press 'n' + 'Enter' to turn off injector");
  Serial.println("Injector is ready now");
}
void loop() {
  modeState = digitalRead(modeSW);    //read mode switch
    if((modeState == 1) && (serialControl == 1))                //if modeSW is UP
```

```
 {
  digitalWrite(injector, HIGH);
  delayMicroseconds(2000);          //turn on time delay in microsecond
  digitalWrite(injector, LOW);
  delay(38);                                //turn off time delay in millisecond
 }
 if(modeState == 0)                 //in modeSW is DOWN
 {
            injState = digitalRead(injtSW);   //read switch state
            if(injState == 0)   //toggle sw down
            {      digitalWrite(injector, HIGH);    }
            if(injState == 1)   //toggle sw up
            {      digitalWrite(injector, LOW);    }
 }
 if(Serial.available())             //Control LAMP outputs via y & n button
 {
             PC = Serial.read();
            if(PC == 'y')
            {  serialControl = 1; Serial.println("Injector on"); }
            if(PC == 'n')
            {  serialControl = 0; Serial.println("Injector off"); }
 }
}
```

Appendix B: Updated CHEMKIN mechanism

MECHANISM

```
ELEM  O N AR H HE
END
SPECIES ! structure, source of thermo-data, source of transport
H  ! burcat, chemkin
H2 ! burcat, chemkin
O   O2    H2O    OH    H2O2    HO2   OX   OHX   O2X   O3
AR ! burcat, chemkin
HE ! burcat, chemkin
N2 ! burcat, chemkin
END
REACTIONS
!*****************************************************************************
! A.KONNOV's detailed reaction mechanism   h/o3 excited 2018
!*****************************************************************************
H+H+M=H2+M                    7.000E+17     -1.0         0.0
 H2/0.0/ N2/0.0/ H/0.0/ H2O/14.3/ ! CO/3.0/ CO2/3.0/
H+H+H2=H2+H2                  1.000E+17     -0.6         0.0
H+H+N2=H2+N2                  5.400E+18     -1.3         0.0
H+H+H=H2+H                   3.200E+15      0.0         0.0
O+O+M=O2+M                    1.000E+17     -1.0         0.0
 O/28.8/ O2/8.0/ N2/2.0/ H2O/5.0/ O3/8.0/ ! NO/2.0/ N/2.0/
O+H+M=OH+M                    6.750E+18     -1.0         0.0
 H2O/5.0/
H2O+M=H+OH+M                  6.060E+27     -3.312  120770.0
 H2O /0/ H2/3.0/ N2 /2.0/ O2 /1.5/ HE /1.1/ !CH4/7/ CO2 /4/
H2O+H2O=H+OH+H2O              1.000E+26     -2.44   120160.0
H+O2(+M)=HO2(+M)              4.660E+12      0.44        0.0
   LOW /1.225E+19 -1.2 0.0/
   TROE /0.5 1 1E+10/
 AR/0.72/ H2O/16.6/ O2/1.0/ H2/1.5/ HE/0.57/ ! CO2/3.61/ CH4/3.5/
```

```
H2O2(+M)=OH+OH(+M)            2.000E+12      0.9     48750.0
   LOW /2.49E+24 -2.3 48750.0 /
   TROE /0.42 1 1E+10/
 H2O/7.5/ H2O2/7.7/ O2/1.2/ N2/1.5/ HE/0.65/ H2/3.7/ !CO2/1.6/ CO/2.8/
O+H2=OH+H                     5.080E+04      2.67     6292.0
H+O2=OH+O                     1.040E+14      0.0     15286.0
H2+OH=H2O+H                    2.140E+08      1.52     3450.0
OH+OH=H2O+O                    2.668E+06      1.82    -1647.0
HO2+O=OH+O2                    2.850E+10      1.0      -723.9
H+HO2=OH+OH                    7.080E+13      0.0       300.0
H2O+O=H+HO2                    2.200E+08      2.0     61600.0
H2+O2=H+HO2                    7.400E+05      2.43    53500.0
HO2+OH=H2O+O2                  7.000E+12      0.0     -1093.0
   DUPLICATE
HO2+OH=H2O+O2                  4.500E+14      0.0     10930.0
   DUPLICATE
HO2+HO2=H2O2+O2                1.030E+14      0.0     11040.0
   DUPLICATE
HO2+HO2=H2O2+O2                1.940E+11      0.0     -1409.0
   DUPLICATE
H2O2+H=HO2+H2                  5.020E+06      2.07     4300.0
H2O2+H=H2O+OH                  2.030E+07      2.02     2620.0
H2O2+O=HO2+OH                  9.550E+06      2.0      3970.0
H2O2+OH=HO2+H2O                1.740E+12      0.0       318.0
   DUPLICATE
H2O2+OH=HO2+H2O                7.590E+13      0.0      7269.0
   DUPLICATE
O2+O+AR=O3+AR                  4.290E+17     -1.5        0.0
   DUPLICATE
O2+O+AR=O3+AR                  5.100E+21     -3.2        0.0
   DUPLICATE
O2+O+M=O3+M                    6.530E+17     -1.5        0.0
```

```
 AR/0.0/ O2/0.95/ O3/2.5/ O/4.0/
   DUPLICATE
O2+O+M=O3+M                1.330E+22    -3.3        0.0
 AR/0.0/ O2/1.07/ O3/2.5/ O/4.0/
   DUPLICATE
O3+O=O2+O2                 4.820E+12     0.0     4094.0
O3+O=O2X+O2                1.440E+11     0.0     4094.0
O+O+M=O2X+M                7.000E+15    -1.0        0.0
 O/28.8/ O2/8.0/ N2/2.0/ H2O/5.0/ O3/8.0/ ! NO/2.0/ N/2.0/
O2X+M=O2+M                 1.800E+06     0.0      400.0
 O/0/ H/0/ AR/0.005/ HE/0.005/ N2/0.002/ H2O/3.3/ H2/2.5/ !CO2/0.01/ CO/5.6/
O2X+O=O2+O                 7.800E+07     0.0        0.0
O2X+H=O2+H                 4.000E+13     0.0     5030.0
O2X+O+M=O+O2+M             3.600E+15     0.0        0.0
 AR/0.63/
O2X+O3=O2+O2+O             3.130E+13     0.0     5644.0
OX+O2X=O+O2                6.030E+12     0.0        0.0
OX+O2=O+O2X                1.590E+13     0.0     -139.0
OX+O2=O+O2                 2.810E+12     0.0     -139.0
OX+M=O+M                   4.800E+11     0.0        0.0
 O2/0/ N2/0/ O/10.0/ H2O/3.0/
OX+N2=O+N2                 1.260E+13     0.0     -230.0
OX+O3=O2+O+O               7.230E+13     0.0        0.0
OX+O3=O2+O2                7.230E+13     0.0        0.0
H2+O2X=H+HO2               6.160E+05     2.335   31080.0
H+O2X=OH+O                 3.500E+08     1.45     4508.0
H+O2X+M=HO2+M              9.890E+09     2.03     3360.0
HO2+OH=H2O+O2X             2.140E+06     1.65     2180.0
OH+O2X=O+HO2               1.300E+13     0.0     34000.0
O3+H=OH+O2                 8.430E+13     0.0      934.0
O3+OH=HO2+O2               1.000E+12     0.0     1870.0
O3+HO2=OH+O2+O2            5.850E-04     4.57    -1377.0
```

```
H+HO2=H2O+OX                2.500E+12      0.0       300.0
OX+H2=OH+H                  8.100E+13      0.0         0.0
OX+H2O=OH+OH                1.000E+14      0.0       -71.0
O+H+M=OHX+M                 1.500E+13      0.0      5970.0
  AR/0.35/ H2O/6.5/ O2/0.4/ N2/0.4/
OHX+O2=OH+O2                8.400E+11      0.5      -482.0
OHX+N2=OH+N2                1.080E+11      0.5     -1238.0
OHX+H2O=OH+H2O              2.960E+12      0.5      -861.0
OHX+H2=OH+H2                3.540E+11      0.5      -444.0
OHX+OH=OH+OH                1.500E+12      0.5         0.0
OHX+H=OH+H                  1.500E+12      0.5         0.0
OHX+O=OH+O                  1.500E+12      0.5         0.0
OHX+AR=OH+AR                2.170E+10      0.5      2060.0
OHX+H2=H2O+H                2.600E+12      0.5      -444.0
OHX+O2=O3+H                 2.520E+11      0.5      -482.0
OHX+O2=HO2+O                1.008E+12      0.5      -482.0
OHX+H2O=H2O2+H              2.960E+12      0.5      -861.0
OHX=OH+hv                   1.400E+06      0.0         0.0
H+O2+H=H2+O2                8.800E+22     -1.835     800.0
H+O2+H=OH+OH                4.000E+22     -1.835     800.0
H+O2+O=OH+O2                7.350E+22     -1.835     800.0
H+O2+OH=H2O+O2              2.560E+22     -1.835     800.0
END
```

THERMODYNAMICS FILE

```
THERMO ALL
 300.000  1000.000  5000.000
O2X singlet       ATcT  O  2.   0.   0.   0.G   200.000  6000.000  1000.0      1
 3.45852381E+00 1.04045351E-03-2.79664041E-07 3.11439672E-11-8.55656058E-16    2
 1.02229063E+04 4.15264119E+00 3.78535371E+00-3.21928540E-03 1.12323443E-05    3
-1.17254068E-08 4.17659585E-12 1.02922572E+04 3.27320239E+00 1.13558105E+04    4
O2                ATcT  O  2.   0.   0.   0.G   200.000  6000.000  1000.0      1
 3.66096065E+00 6.56365811E-04-1.41149627E-07 2.05797935E-11-1.29913436E-15    2
-1.21597718E+03 3.41536279E+00 3.78245636E+00-2.99673416E-03 9.84730201E-06    3
-9.68129509E-09 3.24372837E-12-1.06394356E+03 3.65767573E+00 0.00000000E+00    4
OX singlet        ATcT  O  1.   0.   0.   0.G   200.000  6000.000  1000.0      1
 2.49368475E+00 1.37617903E-05-1.00401058E-08 2.76012182E-12-2.01597513E-16    2
 5.19986304E+04 4.65050950E+00 2.49993786E+00 1.71935346E-07-3.45215267E-10    3
 3.71342028E-13-1.70964494E-16 5.19965317E+04 4.61684555E+00 5.27418934E+04    4
O                 ATcT  O  1.   0.   0.   0.G   200.000  6000.000  1000.0      1
 2.54363697E+00-2.73162486E-05-4.19029520E-09 4.95481845E-12-4.79553694E-16    2
 2.92260120E+04 4.92229457E+00 3.16826710E+00-3.27931884E-03 6.64306396E-06    3
-6.12806624E-09 2.11265971E-12 2.91222592E+04 2.05193346E+00 2.99687009E+04    4
OHX A 2Sigma+     ATcT  O  1.H  1.   0.   0.G   200.000  6000.000  1000.0      1
 2.75582920E+00 1.39848756E-03-4.19428493E-07 6.33453282E-11-3.56042218E-15    2
 5.09751756E+04 5.62581429E+00 3.46084428E+00 5.01872172E-04-2.00254474E-06    3
 3.18901984E-09-1.35451838E-12 5.07349466E+04 1.73976415E+00 5.17770741E+04    4
OH                ATcT  O  1.H  1.   0.   0.G   200.000  6000.000  1000.0      1
 2.83853033E+00 1.10741289E-03-2.94000209E-07 4.20698729E-11-2.42289890E-15    2
 3.69780808E+03 5.84494652E+00 3.99198424E+00-2.40106655E-03 4.61664033E-06    3
-3.87916306E-09 1.36319502E-12 3.36889836E+03-1.03998477E-01 4.48615380E+03    4
H                 L 6/94H   10   00   00   0G   200.000  6000.00  1000.0      1
 0.25000000E+01 0.00000000E+00 0.00000000E+00 0.00000000E+00 0.00000000E+00    2
 0.25473660E+05-0.44668285E+00 0.25000000E+01 0.00000000E+00 0.00000000E+00    3
 0.00000000E+00 0.00000000E+00 0.25473660E+05-0.44668285E+00 0.26219035E+05    4
H2  REF ELEMENT   RUS 78H   20   00   00   0G   200.000  6000.00  1000.0      1
```

2.93286575E+00 8.26608026E-04-1.46402364E-07 1.54100414E-11-6.88804800E-16 2
-8.13065581E+02-1.02432865E+00 2.34433112E+00 7.98052075E-03-1.94781510E-05 3
2.01572094E-08-7.37611761E-12-9.17935173E+02 6.83010238E-01 0.00000000E+00 4
HO2 L 5/89H 1O 20 00 0G 200.000 5000.00 1000.0 1
4.17228741E+00 1.88117627E-03-3.46277286E-07 1.94657549E-11 1.76256905E-16 2
3.10206839E+01 2.95767672E+00 4.30179807E+00-4.74912097E-03 2.11582905E-05 3
-2.42763914E-08 9.29225225E-12 2.64018485E+02 3.71666220E+00 1.47886045E+03 4
H2O L 5/89H 2O 10 00 0G 200.000 6000.00 1000.0 1
0.26770389E+01 0.29731816E-02-0.77376889E-06 0.94433514E-10-0.42689991E-14 2
-0.29885894E+05 0.68825500E+01 0.41986352E+01-0.20364017E-02 0.65203416E-05 3
-0.54879269E-08 0.17719680E-11-0.30293726E+05-0.84900901E+00-0.29084817E+05 4
H2O2 L 2/93H 2O 20 00 0G 200.000 6000.00 1000.0 1
4.57977305E+00 4.05326003E-03-1.29844730E-06 1.98211400E-10-1.13968792E-14 2
-1.80071775E+04 6.64970694E-01 4.31515149E+00-8.47390622E-04 1.76404323E-05 3
-2.26762944E-08 9.08950158E-12-1.77067437E+04 3.27373319E+00-1.63425145E+04 4
AR REF ELEMENT L 6/88AR 1 0 0 0G 200.000 6000.00 1000.0 1
2.50000000E+00 0.00000000E+00 0.00000000E+00 0.00000000E+00 0.00000000E+00 2
-7.45375000E+02 4.37967491E+00 2.50000000E+00 0.00000000E+00 0.00000000E+00 3
0.00000000E+00 0.00000000E+00-7.45375000E+02 4.37967491E+00 0.00000000E+00 4
N2 REF ELEMENT 8/02 N 2 0 0 0G 200.000 6000.00 1000.0 1
2.95257637E+00 1.39690040E-03-4.92631603E-07 7.86010195E-11-4.60755204E-15 2
-9.23948688E+02 5.87188762E+00 3.53100528E+00-1.23660988E-04-5.02999433E-07 3
2.43530612E-09-1.40881235E-12-1.04697628E+03 2.96747038E+00 0.00000000E+00 4
O3 L 5/90 O 3 0 0 0G 200.000 6000.000 1000.0 1
1.23302914E+01-1.19324783E-02 7.98741278E-06-1.77194552E-09 1.26075824E-13 2
1.26755831E+04-4.08823374E+01 3.40738221E+00 2.05379063E-03 1.38486052E-05 3
-2.23311542E-08 9.76073226E-12 1.58644979E+04 8.28247580E+00 1.70545228E+04 4
HE REF ELEMENT g 5/97 HE 1 0 0 0G 200.000 6000.000 1000.0 1
2.50000000E+00 0.00000000E+00 0.00000000E+00 0.00000000E+00 0.00000000E+00 2
-7.45375000E+02 9.28723974E-01 2.50000000E+00 0.00000000E+00 0.00000000E+00 3
0.00000000E+00 0.00000000E+00-7.45375000E+02 9.28723974E-01 0.00000000E+00 4
END

Appendix C: Technical specification of the instruments

MKS Multigas 2030 FTIR gas analyser

Item	Details
Measurement principle	Infrared Spectroscopy
Phase of input sample	Gas
Range of measurement	Part per million (ppm) to part per billion (ppb)
Spectra resolution	0.5 cm^{-1} to 128 cm^{-1}
Scan duration	1 second
Scan frequency	1 Hertz
Laser reference	Silicon carbide at 1100°C
Infrared source	Helium - Neon
Detector	Liquid nitrogen cooled MCT digitally linearised
Pressure transducer	MKS Baratron ±1% uncertainty

MKS 2030 measurement range and accuracy

Specie	Measurement Range	Accuracy
Acetylene	20 ppm to 991 ppm	~ ±5%
Ammonia	13 ppm to 10425 ppm	±5%
Carbon dioxide	0%-vol to 23%-vol	±5%
Carbon monoxide	0%-vol to 19%-vol	±5%
Dodecane	20 ppm to 1000 ppm	~ ±10%
Ethane	100 ppm to 1004 ppm	±5%
Ethanol	100 ppm to 10000 ppm	~ ±5%
Ethylene	10 ppm to 3000 ppm	±3%
Formaldehyde	4 ppm to 69 ppm	~ ±5%
Formic acid	19 ppm to 466 ppm	±5%
Methane	210 ppm to 20000 ppm	~ ±5%
Methanol	19 ppm to 932 ppm	±5%
Nitric acid	19 ppm to 2795 ppm	~ ±5%
Nitrogen dioxide	33 ppm to 1939 ppm	~ ±3%

MKS 2030 measurement range and accuracy (continue)

Specie	Measurement Range	Accuracy
Nitrous oxide	13 ppm to 200 ppm	~ ±5%
Propane	102 ppm to 25427 ppm	~ ±5%
Propylene	26 ppm to 194 ppm	~ ±10%
Toluene	186 ppm to 932 ppm	±5%
Water	2%-vol to 40%-vol	±5%

Hsense Hydrogen mass spectrometer

Item	Details	Item	Details
Measurement mass range	2 to 4 amu	Measurement range	0-50000 ppm and 0-100%-vol
Accuracy	<±2%	Reproducibility	<±3%
Analysis duration	>= 1 ms/amu	Resolution	< 1 amu
Response time	T90 < 1s	Lower detection limit	< 1 ppm for H_2 and He
Concentration drift	<±3% over 24h		

Engine rest rig instrumentations

Item	Measurement Range	Accuracy
Dynamometer load cell	0 to 1000 N	~±0.05% FS
Rheonik RM015 fuel flow meter	0 to 20 kg/h	~±0.12%
AVL GM12D pressure transducer	0-200 bar	±0.3% FS
Thermocouple	-40 to 1100°C	±0.5%

Testo 340 flue gas analyser

Item	Measuring range	Resolution	Accuracy
O_2	0 to 25%-vol	0.01%-vol	±0.2%-vol
CO	0 to 10000 ppm	1 ppm	±10 ppm or ±10% of m.v. (0 to 200 ppm) ±20 ppm or ±5% of m.v. (201 to 2.000 ppm) ±10% of m.v. (2.001 to 10.000 ppm)
CO_2 (calculated from O_2)	0 to CO_2 max	0.1%-vol	±0.2%-vol

Appendix D: Author Publications

Published research papers

S. Sittichompoo, H. Nozari, J.M. Herreros, N. Serhan, J.A.M. da Silva, A.P.E. York, P. Millington, A. Tsolakis, "Exhaust energy recovery via catalytic ammonia decomposition to hydrogen for low carbon clean vehicles", Fuel, Volume 285, 2021, 119111, https://doi.org/10.1016/j.fuel.2020.119111. (This publication is part of the chapter 4)

S. Sittichompoo, S. Kanagalingam, L.E.J. Thomas-Seale, A. Tsolakis, J.M. Herreros, "Characterization of particle emission from thermoplastic additive manufacturing", Atmospheric Environment, Volume 239, 2020, 117765, https://doi.org/10.1016/j.atmosenv.2020.117765.

On-going/ Future publication

S. Sittichompoo, H. Nozari, M. Mardani, J. Singh, S. Zeraati-Rezaei, O. Doustdar, J.M. Herreros, and A. Tsolakis "Aqeuous Urea Decomposition to Hydrogen for Transport Decarbonisation" (Part of the thesis chapter 5) This paper is planned to publish with Fuel or International Journal of Hydrogen Energy in 2023.

S. Sittichompoo, H. Nozari, J.M. Herreros, and A. Tsolakis "Carbon Neutral Energy Carrier for On-board Hydrogen Production" (Part of the thesis chapter 6) This paper is planned to publish with Fuel or International Journal of Hydrogen Energy in 2023.